

AD 605671

UNIVERSITY OF MINNESOTA
INSTITUTE OF TECHNOLOGY

DEPARTMENT OF AERONAUTICAL ENGINEERING



MINNEAPOLIS 14, MINNESOTA

**CLEARINGHOUSE FOR FEDERAL SCIENTIFIC AND TECHNICAL INFORMATION CFSTI
DOCUMENT MANAGEMENT BRANCH 410.11**

LIMITATIONS IN REPRODUCTION QUALITY

ACCESSION #

- ☒ 1. WE REGRET THAT LEGIBILITY OF THIS DOCUMENT IS IN PART UNSATISFACTORY. REPRODUCTION HAS BEEN MADE FROM BEST AVAILABLE COPY.
- ☒ 2. A PORTION OF THE ORIGINAL DOCUMENT CONTAINS FINE DETAIL WHICH MAY MAKE READING OF PHOTOCOPY DIFFICULT.
- ☐ 3. THE ORIGINAL DOCUMENT CONTAINS COLOR, BUT DISTRIBUTION COPIES ARE AVAILABLE IN BLACK-AND-WHITE REPRODUCTION ONLY.
- ☐ 4. THE INITIAL DISTRIBUTION COPIES CONTAIN COLOR WHICH WILL BE SHOWN IN BLACK-AND-WHITE WHEN IT IS NECESSARY TO REPRINT.
- ☐ 5. LIMITED SUPPLY ON HAND: WHEN EXHAUSTED, DOCUMENT WILL BE AVAILABLE IN MICROFICHE ONLY.
- ☐ 6. LIMITED SUPPLY ON HAND: WHEN EXHAUSTED DOCUMENT WILL NOT BE AVAILABLE.
- ☐ 7. DOCUMENT IS AVAILABLE IN MICROFICHE ONLY.
- ☐ 8. DOCUMENT AVAILABLE ON LOAN FROM CFSTI (TT DOCUMENTS ONLY).
- ☐ 9.

PROCESSOR:

TSL-107-10/64

AD 605671

118-7

COPY	OF	1
HARD COPY	\$.	4.00
MICROFICHE	\$.	0.75

✓ Progress Report No 23

B. THEORETICAL PARACHUTE INVESTIGATIONS

Aeronautical Systems Division Contract No.

AF 33(616)-8310; Project No 6065; Task No 60252

1 September 1962 to 30 November 1962

Department of Aeronautics and Engineering

Mechanics, No 5007 ✓

University of Minnesota

605671

Dr. H. G. Heinrich, Professor, Department of Aeronautics and Engineering Mechanics
Dr. T. Riabokin, Research Associate, Department of Aeronautics and Engineering Mechanics
Prof. S. K. Ibrahim, Research Fellow, Department of Aeronautics and Engineering Mechanics
Mr. E. L. Haak, Senior Engineer, Department of Aeronautics and Engineering Mechanics
Mr. R. J. Niccum, Senior Engineer, Department of Aeronautics and Engineering Mechanics
Mr. E. M. Linhart, Engineer, Department of Aeronautics and Engineering Mechanics
and graduate and undergraduate students of the Department of Aeronautics and Engineering Mechanics (see Appendix)

63-01-5555

TABLE OF CONTENTS

<u>Project No</u>		<u>Page</u>
1	Investigation of Wake Effects on the Behavior of Parachutes and Other Retardation Devices Behind Large Bodies . . .	2
	a) Velocity Distribution in the Wake of Bodies of Revolution in Turbulent Subsonic Flow	
	b) Theoretical Analysis of Turbulent Wake in Supersonic Flow	
4	Investigation of Basic Stability Parameters of Conventional Parachutes	3
	a) Experimental Determination of the Apparent Moment of Inertia of Parachutes	
	b) Wind Tunnel and Theoretical Investigation of Dynamic Stability of Conventional Parachutes with Store	
7	Theoretical Study of Supersonic Parachute Phenomena	43
	a) Water Analogy Studies	
	b) Supersonic Wind Tunnel Studies of Flexible Spiked Parachute Models	
8	Theoretical Analysis of the Dynamics of the Opening Parachute	58
	a) Experimental Analysis of the Dynamics of the Opening Parachute	
	b) Mass Flow Study of the Opening Parachute	
9	Statistical Analysis of Extraction Time, Deployment Time, Opening Time, and Drag Coefficient for Aerial Delivery Parachutes and Systems	65

<u>Project No</u>		<u>Page</u>
12	Gliding Aerodynamic Decelerator	66
13	Effective Porosity Studies	72
	a) Parachute Cloths	
	b) Ribbon Grid Configurations	
14	Study of Flow Patterns of Aerodynamic Decelerators by Means of the Surface Wave Analogy	73
16	Stress Analysis of the T-10 Troop Parachute	76
17	Aerodynamic Characteristics of the Parachute Stabilized A-21 Cargo Container	77
18	Aerodynamic Characteristics of the Cross and Wagon-Wheel Type Parachutes	88
	a) Evaluation of "Cross" and "Wagon-Wheel" Type Parachute Configurations in Free Stream	
19	Determination of Mass Flow Through Parachutes with Inherent Geometric Porosity,	93

THEORETICAL PARACHUTE INVESTIGATIONS

Progress Report No 23

INTRODUCTION

1.0 This is the twenty-third quarterly report covering the time from 1 September 1962 to 30 November 1962 on the study program on basic information of Aerodynamic Deceleration.

1.1 As in preceding reporting periods, work during this reporting period has been pursued in accordance with the technical program, and is described in the following sections of this report.

Project No 1

2.0 Investigation of Wake Effects on the Behavior of Parachutes and Other Retardation Devices Behind Large Bodies at Subsonic and Supersonic Speeds

2.1 Velocity Distribution in the Wake of Bodies of Revolution in Turbulent Subsonic Flow

A preliminary technical report concerning this work has been written and will be submitted for review shortly. Further reports are under preparation.

2.2 Theoretical Analysis of Turbulent Wake in Supersonic Flow

No new work concerning this phase of the program will be reported.

Project No 4

3.0 Investigation of Basic Stability Parameters of Conventional Parachutes

This project will be reported as two separate investigations. They are:

- 1) Experimental determination of the apparent moment of inertia of parachutes.
- 2) Wind tunnel and theoretical investigation of dynamic stability of conventional parachutes.

3.1 Experimental Determination of the Apparent Moment of Inertia of Parachutes

3.1.1 Introduction

Progress Report No 22 introduced the notation system adopted for this work, outlined some modifications of the test apparatus and experimental procedure, and presented initial test results for hollow hemispherical canopy models oscillating about an axis through the canopy center of gravity. Non-dimensional apparent moment of inertia coefficients based on the enclosed fluid mass and the surface area of the canopy were calculated and reported.

3.1.2 Present Work

During the present reporting period, tests were conducted on hemispherical, circular flat, and ribless guide surface canopy models oscillating about an axis through the center of gravity of the enclosed fluid mass.

In addition, preliminary tests were conducted on a model canopy oscillating about an axis passing through the confluence point and perpendicular to the longitudinal axis of symmetry of the canopy.

3.1.2.1 Modifications and Improvements in Experimental Procedure and Data Reduction

In considering the dynamic behavior of parachute canopies, the mass of the canopy itself is often negligible as compared to that of the enclosed air mass. It is therefore logical to refer the apparent mass and apparent moment of inertia to some reference mass and moment of inertia dictated by the canopy geometry and the fluid density.

In Progress Report No 22, the reference mass used was that of the fluid enclosed by the canopy. The reference moment of inertia was obtained by multiplying the enclosed fluid mass by the canopy surface area.

This hypothetical moment of inertia is very much larger than the moment of inertia of the enclosed mass when oscillating about an axis through its center of gravity since the canopy surface area is much larger than the square of the radius of gyration of the enclosed mass and this explains the very small values of the non-dimensional apparent moment of inertia coefficients reported in Progress Report No 22.

The use of the enclosed fluid mass which is different for each canopy tends to complicate the comparisons between different canopy shapes from the viewpoint of apparent moment of inertia. Furthermore, it cannot be applied to the limiting case of thin flat discs. It is conventional, in the case of discs, to use for reference the mass of a sphere of the same radius as that of the disc, i.e., $M = \frac{4}{3}\rho\pi r^3$. For the moment of inertia, it would be logical to use for reference, the moment of inertia of the above spherical mass, i.e.,

$$I_y = M k^2 = \frac{4}{3}\rho\pi r^3 \times \frac{2}{5}r^2 = \frac{8}{15}\rho\pi r^5, \quad (4.0)$$

where k is the radius of gyration of the spherical mass.

The same reference moment of inertia, based on the canopy projected diameter has been adopted for the different shapes tested, thereby providing a simple basis of comparison between different parachutes of equal projected diameter.

3.1.2.2 Experimental Results

The model arrangement for the tests on the hemispherical, the circular flat, and the ribless guide surface canopies was similar to that illustrated in Figs 4-3 and 4-4 of Progress Report No 22, but with the axis of oscillation passing through the center of gravity of the enclosed mass.

The data and calculations of the canopy apparent moment of inertia I_c' , the reference moment of inertia I_y , and the non-dimensional apparent moment of inertia coefficient $A_{y,c'}$ for the two hemispherical canopy models are given in Tables 4-1 and 4-2. For purposes of comparison, the values of the apparent moment of inertia coefficients for the same canopies when oscillating about an axis through the canopy center of gravity reported in Progress Report No 22, but converted to the new reference moment of inertia I_y have been calculated and are also given in Tables 4-1 and 4-2. As expected, the apparent moment of inertia of the hemispherical canopy is smaller when oscillating about an axis through the center of gravity of the enclosed mass since the distance from that axis to the center of the hemisphere is $3/8 r$ as compared to $r/2$ for the previous case.

The test data and calculated results indicate good repeatability for tests with the same model and satisfactory agreement between the tests on two models having the same geometry but different sizes.

Table 4-3 presents the test data and calculated results for the circular flat canopy model. The results show satisfactory repeatability and indicate an apparent moment of inertia coefficient of the same order as that of the hemispherical canopy.

Table 4-4 presents the test data and calculated results for the ribless guide surface canopy. The results indicate an apparent moment of inertia coefficient of the same order as that of the circular flat and hemispherical canopies.

Preliminary tests to determine the apparent moment of inertia of circular flat canopies oscillating about an axis through the confluence point, perpendicular to the canopy axis of symmetry, were conducted. For these tests, two canopy models were mounted symmetrically about the torsion rod in the same manner as in the earlier tests on discs reported in Progress Report No 21. To reduce excessive relative damping, the inertia of the system was increased by adding two solid spheres symmetrically mounted about the torsion rod. The spheres were attached in such a way that the canopies could be removed and attached without affecting the other parts of the system.

The apparent moment of inertia of the system with and without the canopy models was determined experimentally and the apparent moment of inertia of the canopies obtained by subtraction. This method reduces certain errors produced by the canopy supporting arms since they are left on the system when the canopies are removed.

The model tests with oscillation about the confluence point were of an exploratory nature to determine suitable experimental parameters such as model size and to perfect the experimental technique. Not enough numerical data is yet available for analysis and reporting.

3.1.3 Proposed Work

Tests on the ribbon parachute canopy for oscillation about an axis through the center of gravity of the enclosed mass await completion of this model.

The experimental techniques for determining the apparent moment of inertia for the circular flat, the ribbon, and the ribless guide surface canopies when oscillating about an axis through the confluence point have been developed.

Work in this direction is the subject of specific proposals for continued research in this area. Also contained in these proposals are tests to determine the apparent moment of inertia of cubes, ogives, cylinders, and skirted hemispheres.

3.2 Wind Tunnel and Theoretical Investigation of Dynamic Stability of Conventional Parachutes with Store

3.2.1 Introduction

This study will analyze the oscillatory behavior of a parachute with store combination both theoretically and experimentally.

The work done during this reporting period will be reported in the following phases.

- 1) Design and fabrication of a store model.
- 2) Equation of motion of parachute and store system.
- 3) Development of a damping "factor."
- 4) Development of an empirical equation.

3.2.2 Design and Fabrication of a Store Model

An ogive cylinder (Fig 4-1) with the dimensions shown in Fig 4-2 was constructed. A potentiometer was incorporated into the body of the ogive as shown in the detail drawing of Fig 4-2. Bearings are mounted into the potentiometer block so that the system will be suspended at 50% chord of the ogive which corresponds with the center of gravity of the system. With an oscillation of the ogive, the resistance element of the potentiometer remains stationary on the supporting rod while the center tap pick-off rotates with the

model. The resistance element is used as a shunt on one leg of a Wheatstone bridge so that the resistance change is approximately that of a conventional strain gage. The output of the Wheatstone bridge is then fed into an amplifier and the amplified signal is recorded on the Century model 408 oscillograph so that the final result is a filmed recording of the oscillations of the ogive. Work has been done by the U. S. Naval Aircraft Torpedo Unit at Quonset Point, Rhode Island, on drop tests from aircraft. As a basis for work to be done here the same diameter ratio of parachute to forebody was used. The riser length was also scaled down accordingly. The purpose of this was to enable a comparison of our results with established work.

A geodetic suspension system (Fig 4-5) is used so that the ogive and parachute may be considered to constitute a rigid system. Two lead weights are included inside the ogive for balancing the system and changing the moment of inertia, one fore and one aft of the center of gravity. These weights can be moved by turning threaded shafts with an Allen-head wrench at the base of the ogive.

The supporting rod is $3/8$ inch drill rod 34 inches long. It is supported on two struts at midstream of the tunnel. This rod is used as one lead of the potentiometer. The sliding contact consists of a ball bearing being pushed against the resistance element by a small spring, which can be compressed by a set screw set in a sleeve which is mounted into the plastic block. This contact is brought to the side of the ogive by a screw in the sleeve. This screw has a slider on the end which contacts a copper ring insulated from the shaft. A wire from the copper ring and a wire connected to the shaft itself serve as the two leads of the potentiometer.

The parachutes used were eight-gore ribless guide surface types of different nominal porosities. The profile dimensions and static stability characteristics can be found in Ref 2.

3.2.3 Equation of Motion of a Parachute and Store System

In this investigation, the coordinates and free body shown in Fig 4-6 are employed with assumptions and symbols defined as follows.

3.2.3.1 The assumptions made to derive the equation of motion of the system are:

- a) The motion is restricted to one plane (x-y plane)
- b) The parachute and store combination constitutes a rigid body where the axes of the parachute and store always coincide
- c) The apparent mass of the parachute acts at the center of gravity (c.g.) of the canopy
- d) The apparent mass of the store is neglected.

3.2.3.2 List of Symbols

α	= angle of attack of the parachute
\hat{k}	= unit vector in z direction
m_s	= mass of the store
m_1	= mass of air enclosed in the canopy
m_{app}	= apparent mass of the parachute
m_c	= mass of the canopy
m_t	= $m_1 + m_c$ = total mass of the parachute
I_{az}^*	= total moment of inertia of the canopy rotating about an axis through the center of mass and parallel to the z-axis
I_s^*	= total moment of inertia of the store rotating about an axis through the center of gravity and parallel to the z-axis
V	= wind tunnel velocity
ρ	= air density
q	= $\frac{1}{2}\rho V^2$ = dynamic pressure
S	= area of parachute canopy upon which all coefficients are based

ω_z	= angular velocity of the system about the z-axis
0	= origin of x-y-z coordinate system at the point of suspension of the system
s	= distance between center of mass of canopy and base of the store
1	= distance between center of mass and center of pressure of the canopy
l_1	= distance between center of gravity and center of pressure of the store, negative for unstable store
l_2	= $l_3 + l_1$ = distance between origin and center of pressure of store
l_3	= distance from base to center of gravity of store
l_4	= distance between center of gravity of store and center of gravity of the system
C_N	= normal force coefficient of the parachute
C_{N_s}	= normal force coefficient of the store

3.2.3.3 Derivation of Equation of Motion

According to Newton's law of motion, the summation of all moments of external forces must equal the time rate of change of moment of momentum. Applying this to the moment of momentum, we have

$$\dot{\vec{H}} = \sum \vec{M} , \quad (4.1)$$

where H is the angular moment, M the applied moment, $(\dot{})$ denotes differentiation with respect to time, and the arrow indicates a vector quantity. Since the principal axes of rotation are in a single plane,

$$\dot{\vec{H}} = I_z^* \dot{\omega} \hat{k} , \quad (4.2)$$

where the superscript * refers to the moment of inertia, I_z^* as being about an axis through the center of gravity.

Combining Eqns (4.1) and (4.2), we have

$$I_z^* \ddot{\alpha} = \sum M_z \quad (4.3)$$

The standard definition of a positive aerodynamic moment in parachute technology is that it is a restoring moment. This moment is considered positive when for positive angle of attack, it tends to rotate the canopy in the direction toward zero angle of attack (Ref 2).

From Fig 4-6 we see that:

$$I_z^* = I_{az}^* + m_v (l + s + l_3 - l_4)^2 + I_s^* + m_s l_4^2 \quad (4.4)$$

$$M = N(l + s + l_3 - l_4) + N_s(l_1 - l_4) \quad (4.5)$$

$$m_v(l + s + l_3 - l_4) = m_s l_4 \quad (4.6)$$

Using Eqns (4.3), (4.4), and (4.5) we have:

$$I_z^* \ddot{\alpha} + M = 0$$

or

$$\begin{aligned} & \left[I_{az}^* + m_s l_4 (l + s + l_3) + I_s^* \right] \ddot{\alpha} + \\ & + N(l + s + l_3 - l_4) + N_s(l_1 - l_4) = 0 \end{aligned} \quad (4.7)$$

We will now introduce the relations:

$$N = C_N q S \quad \text{and} \quad N_s = C_{N_s} q S$$

When the normal force coefficient of a ribless guide surface parachute is found through static wind tunnel tests the C_N is very nearly proportional to angle of attack. It is therefore sufficient to use $C_N = \frac{2C}{\beta \alpha}$. When the canopy is undergoing

a dynamic oscillation there will be a lateral movement perpendicular to the main flow resulting in an additional component of normal force.

We may think of this in another respect. If we suppose that the main (axial) flow is zero and that somehow the canopy is rigid there will be a normal force or side drag exerted on the canopy if it is rotated about some point on the axis, in this case the suspension point of the ogive. The lateral velocity in this case would be $(S + l_3 - l_4) \dot{\alpha}$. In order that the equations remain linear we assume:

$$C_N = f(\alpha, \dot{\alpha}) = \frac{\partial C_N}{\partial \alpha} \alpha + \frac{\partial C_N}{\partial \dot{\alpha}} \dot{\alpha} \quad (4.8)$$

We may now write Eqn (4.7) as:

$$\begin{aligned} & \left[I_{aa}^* + m_s l_4 (l + S + l_3) + I_s^* \right] \ddot{\alpha} + \\ & + q S (l + S + l_3 - l_4) \left(\frac{\partial C_N}{\partial \alpha} \alpha + \frac{\partial C_N}{\partial \dot{\alpha}} \dot{\alpha} \right) + \\ & + q S (l_1 - l_4) \left(\frac{\partial C_{N2}}{\partial \alpha} \alpha + \frac{\partial C_{N2}}{\partial \dot{\alpha}} \dot{\alpha} \right) = 0 \end{aligned} \quad (4.9)$$

Assuming $\frac{\partial C_{N2}}{\partial \dot{\alpha}} \ll \frac{\partial C_N}{\partial \dot{\alpha}}$ we have:

$$\begin{aligned} & \left[I_{aa}^* + m_s l_4 (l + S + l_3) + I_s^* \right] \ddot{\alpha} + \\ & + \left[(l + S + l_3 - l_4) \frac{\partial C_N}{\partial \dot{\alpha}} \right] q S \dot{\alpha} + \\ & \left[(l + S + l_3 - l_4) \frac{\partial C_N}{\partial \alpha} + (l_1 - l_4) \frac{\partial C_{N2}}{\partial \alpha} \right] q S \alpha = 0. \end{aligned} \quad (4.9a)$$

3.2.3.4 Solution of the Equation of Motion
Equation (4.9a) has the form

$$\ddot{\alpha} + 2n\dot{\alpha} + \omega_n^2 \alpha = 0. \quad (4.10)$$

This is the general equation of motion of a free damped vibration. The solution of this equation must be a function

which has the property that repeated differentiations do not change its form, since the function and its first and second derivatives must be added together to give zero (Ref 1). The general solution may be written as:

$$x = C_1 e^{m_1 t} + C_2 e^{m_2 t},$$

where

$$m_1 = -\eta + \sqrt{\eta^2 - \omega_n^2}$$

$$m_2 = -\eta - \sqrt{\eta^2 - \omega_n^2}.$$

The physical significance of this solution depends on the relative magnitudes of η^2 and ω_n^2 , which determine whether the exponents are real or complex. For the exponent to be real,

$$\eta^2 > \omega_n^2.$$

Physically this means a relatively large damping since η is a measure of damping in the system.

Then the solution is:

$$x = C_1 e^{-\eta_1 t} + C_2 e^{-\eta_2 t}, \quad (4.11)$$

where η_1 and η_2 are real quantities. In this event the motion is not oscillatory, but is an exponential subsidence. Because of the relatively large damping, the mass released from rest never passes the static equilibrium position. Such a system is said to be "overdamped."

On the other hand, if the damping is small such that $\eta^2 < \omega_n^2$, then we can write:

$$\begin{aligned} x &= C_1 e^{(-\eta + i\sqrt{\omega_n^2 - \eta^2})t} + C_2 e^{(-\eta - i\sqrt{\omega_n^2 - \eta^2})t} \\ &= e^{-\eta t} \left[C_1 e^{(i\sqrt{\omega_n^2 - \eta^2})t} + C_2 e^{(-i\sqrt{\omega_n^2 - \eta^2})t} \right]. \end{aligned}$$

Using the relationship

$$e^{i\theta} = \cos \theta + i \sin \theta,$$

the displacement may be represented as:

$$\alpha = e^{-nt} \left[(C_1 + C_2) \cos \sqrt{\omega_n^2 - n^2} t + i (C_1 - C_2) \sin \sqrt{\omega_n^2 - n^2} t \right].$$

Since the constants c_1 and c_2 are arbitrary and are to be determined by the initial conditions, we may simplify the expression by introducing the constant $c_1' = \frac{1}{2}(c_1 - c_2)$ and $c_2' = c_1 + c_2$; dropping the primes and substituting into the previous equation, we have

$$\alpha = e^{-nt} \left[C_1 \sin \sqrt{\omega_n^2 - n^2} t + C_2 \cos \sqrt{\omega_n^2 - n^2} t \right]. \quad (4.12)$$

Comparing the two solutions [Eqns (4.11) and (4.12)], we see that the effect of the damping is to increase the period of the vibration and to decrease the magnitudes of successive peaks of the vibration, since the amplitude of the vibration decreases exponentially with time.

As a convenient measure of the damping we may compare the ratio of the amplitudes of successive cycles of the vibration such that

$$\frac{\alpha_1}{\alpha_2} = \frac{e^{-nt_1}}{e^{-n(t_1 + \frac{2\pi}{\sqrt{\omega_n^2 - n^2}})}} = e^{\frac{2\pi n}{\sqrt{\omega_n^2 - n^2}}}.$$

The amount of damping is often specified by giving the logarithmic damping decrement δ , where

$$\delta = \log \frac{\alpha_1}{\alpha_2} = \log e^{\frac{2\pi n}{\sqrt{\omega_n^2 - n^2}}} = \frac{2\pi n}{\sqrt{\omega_n^2 - n^2}}. \quad (4.13)$$

For systems having small damping, a simple way of determining the logarithmic damping decrement from the free vibration curve is to use the relationship,

$$\begin{aligned}\delta &= \log \left(\frac{\alpha + \Delta\alpha}{\alpha} \right) = \log \left(1 + \frac{\Delta\alpha}{\alpha} \right) \\ &= \frac{\Delta\alpha}{\alpha} - \frac{1}{2} \left(\frac{\Delta\alpha}{\alpha} \right)^2 + \frac{1}{3} \left(\frac{\Delta\alpha}{\alpha} \right)^3 + \dots\end{aligned}$$

For small value of $\frac{\Delta\alpha}{\alpha}$, the higher order terms may be neglected, yielding:

$$\delta \approx \frac{\Delta\alpha}{\alpha} .$$

Thus the logarithmic damping decrement is approximately equal to the fractional decrease in amplitude during one cycle of the vibration for small amounts of damping. If the fraction of critical damping is small and α_1 and α_2 are nearly equal, it would be more accurate to measure the second ordinate α_n after n cycles. Under such circumstances,

$$\delta = \frac{1}{n} \log \frac{\alpha_1}{\alpha_n} . \quad (4.14)$$

The logarithmic decrement can be obtained from a relatively simple measurement. The absolute values of ordinate and abscissae of the decay curve need not be known; therefore, the measuring apparatus need not even be calibrated except for determination of initial conditions.

3.2.4 Development of the Damping Factor

In order to determine the degree of validity of the simplified mechanical model chosen, tests were performed at various dynamic pressures. These tests were conducted in the 38 x 54 inch test section of the subsonic horizontal return wind tunnel of the Aeronautics and Engineering Mechanics Department at the University of Minnesota. The oscillation-time histories were recorded for several runs at each velocity

for the three different parachutes. Since there was some variations in the traces obtained the amplitudes and periods were measured and tabulated. Average values were then found for the magnitudes and periods. Two of the runs for each dynamic pressure closest to the average were then traced and are shown in Figs (4-7) through (4-23) along with the theoretical curve which will be derived in the next chapter.

When the average magnitudes were found they were used to compute the experimental damping factor. This was found in the following way;

Since

$$\frac{\alpha_1}{\alpha_2} = e^{\frac{2\pi n}{\sqrt{\omega_n^2 - n^2}}}$$

$$\frac{2\pi n}{\sqrt{\omega_n^2 - n^2}} = \ln_e \frac{\alpha_1}{\alpha_2} \quad (4.13)$$

or
$$n = \frac{\sqrt{\omega_n^2 - n^2}}{2\pi} \ln_e \frac{\alpha_1}{\alpha_2}$$

and: $T = \frac{2\pi}{\sqrt{\omega_n^2 - n^2}}$ where T is the period,

so:

$$n = \frac{1}{T} \ln_e \frac{\alpha_1}{\alpha_2} = \frac{1}{T} \delta \quad (4.15)$$

For each velocity and each parachute we have found an average value for T and $\frac{\alpha_1}{\alpha_2}$ so that from this we can determine the damping factor n. A graph of damping factor versus dynamic pressure is shown in Fig 4-24. This data is also tabulated in Table 4-5.

It can be seen from this figure that n is not zero when q = 0. This can best be expressed as viscous damping inherent in the mounting system and potentiometer assumed to be proportional to the angular velocity. The equations of the straight lines in the figure are:

$$1) \text{ For the } 30 \text{ ft}^3/\text{ft}^2\text{-min nominal porosity chute.}$$

$$2n = 1.4 + 0.472q \quad (4.16)$$

$$2) \text{ For the } 60\text{-}90 \text{ ft}^3/\text{ft}^2\text{-min nominal porosity chute.}$$

$$2n = 1.4 + 0.562q \quad (4.17)$$

$$3) \text{ For the } 120 \text{ ft}^3/\text{ft}^2\text{-min nominal porosity chute.}$$

$$2n = 1.4 + 0.843q \quad (4.18)$$

It is seen that these equations are of the form $2n = A + Bq$ where the constant A is attributed to damping in the mounting system.

3.2.5 An Empirical Equation

If we compare equations,

$$I \ddot{\alpha} + qSL \frac{\partial C_N}{\partial \dot{\alpha}} \dot{\alpha} + \left[L \frac{\partial C_N}{\partial \alpha} + (l_1 - l_2) \frac{\partial C_{Ns}}{\partial \alpha} \right] qS \alpha = 0 \quad (4.9a)$$

and

$$\ddot{\alpha} + 2n\dot{\alpha} + \omega_n^2 \alpha = 0, \quad (4.10)$$

we see that:

$$2n = \frac{qSL}{I} \frac{\partial C_N}{\partial \dot{\alpha}}$$

so that:

$$\frac{\partial C_N}{\partial \dot{\alpha}} = \frac{2nI}{qSL} \quad (4.19)$$

If we drop the constant A in Eqns (4.16), (4.17), and (4.18), we see that

$$\frac{\partial C_N}{\partial \dot{\alpha}} = \frac{I}{SL} B \quad (4.20)$$

for the system, where B is the slope of the appropriate curve in Fig 4-24.

To confirm the above relation it was decided to run the same system with only the moment of inertia of the ogive changed. Figure 4-25 shows a plot of $2n$ versus q for the two moments of inertia. By measuring the slope of the curves we find the factor B and calculate $\frac{\partial C_N}{\partial \alpha}$ by use of Eqn (4.20). We see that within the range of experimental error $\frac{\partial C_N}{\partial \alpha} = \text{constant}$. For:

$$\begin{aligned} I_s^* &= 0.01278 \text{ slug-ft}^2 \\ m_s &= 0.1583 \text{ slug} \\ I_z^* &= 0.0203 \text{ slug-ft}^2 \\ 30 \text{ ft}^3/\text{ft}^2\text{-min nominal porosity ribless guide} \\ &\text{surface parachute} \end{aligned}$$

$$B = 0.472 \text{ ft-sec/slug}$$

$$\frac{\partial C_N}{\partial \alpha} = 0.0052 \text{ sec.}$$

For:

$$\begin{aligned} I_s^* &= 0.004548 \text{ slug-ft}^2 \\ m_s &= 0.0708 \text{ slug} \\ I_z^* &= 0.01498 \text{ slug-ft}^2 \\ 30 \text{ ft}^3/\text{ft}^2\text{-min nominal porosity ribless guide} \\ &\text{surface parachute} \end{aligned}$$

$$B = 0.343 \text{ ft-sec/slug}$$

$$\frac{\partial C_N}{\partial \alpha} = 0.00538 \text{ sec.}$$

The data for the store and parachutes was the following:

$$\begin{aligned}
l &= 0.19 \text{ ft} & l_1 &= -0.18 \text{ ft} & l_2 &= 0.63 \text{ ft} \\
l_3 &= 0.45 \text{ ft} & S &= 1.73 \text{ ft} \\
I_{az}^* &= 0.0000335 \text{ slug-ft}^2 & m_t &= 0.00185 \text{ slug} \\
L &= l + S + l_3 - l_4 = 2.343 \text{ ft} \\
S &= 0.786 \text{ ft}^2
\end{aligned}$$

$$\frac{\partial C_{Ns}}{\partial \alpha} = 0.092 \text{ (Based on } S = 0.786 \text{ ft}^2)$$

I_s^* and m_s were variable.

Substituting these numbers into Eqn (4.9a) we get:
for $I_s^* = 0.01278 \text{ slug-ft}^2$, $m_s = 0.1583 \text{ slug}$

$$\ddot{\alpha} + 2n\dot{\alpha} + \left[79.8 \frac{\partial C_N}{\partial \alpha} - 0.639 \right] \alpha = 0. \quad (4.21)$$

This is the general differential equation for the assumed mechanical system. We have now only to choose the parachute and the dynamic pressure we desire and we will arrive at the solution, using the relations developed in the preceding chapter. Equations for the three parachutes used at several dynamic pressures are tabulated in Table 4-6.

It is the equations tabulated in Table 4-6 that are plotted in Figs 4-7 through 4-23 with two experimental traces taken of the corresponding parachute and dynamic pressure.

It may be noted that the period of the experimental trace decreases slightly after the initial deflection. After examining the data for the static stability normal force curve, it was noted that $\frac{\partial C_N}{\partial \alpha}$ for $\alpha \neq 0$ is somewhat higher than for $\frac{\partial C_N}{\partial \alpha}$ in the general range of $\pm 15^\circ$. Since $\frac{\partial C_N}{\partial \alpha}$ was assumed to be linear in the theory we would imagine that as the oscillations grow smaller $\frac{\partial C_N}{\partial \alpha}$ is higher, thereby increasing the angular frequency. Thus the decrease in period can be attributed to non-linearity of the normal force curve near $\alpha = 0$.

3.2.5.1 Comparison of Theory and Experiment

We have seen in Figs 4-7 through 4-23 that the experimental traces are very closely approximated by the theoretical traces. Since the period T , can be found both theoretically and experimentally it is desirable to make a graphic comparison. Since the theoretical relationship says that the natural period is inversely proportional to the velocity, the periods were plotted versus the free stream velocity in Figs 4-26 through 4-28.

3.2.5.2 Conclusions and Results

Using Eqns (4.20) and Fig 4-24, we have determined the parameter $\frac{\partial C_N}{\partial \alpha}$.

- 1) For the 30 ft³/ft²-min nominal porosity ribless guide surface parachute:

$$\frac{\partial C_N}{\partial \alpha} = 0.0052 \quad (4.22)$$

- 2) For the 60-90 ft³/ft²-min nominal porosity ribless guide surface parachute:

$$\frac{\partial C_N}{\partial \alpha} = 0.0062 \quad (4.23)$$

- 3) For the 120 ft³/ft²-min nominal porosity ribless guide surface parachute:

$$\frac{\partial C_N}{\partial \alpha} = 0.0093 \quad (4.24)$$

3.2.6 Proposed Work

3.2.6.1 Progress Report No 18 included a strictly analytical method of describing the dynamic stability of a parachute store system. The amplitude-time and frequency velocity relationships of the analytical method and the empirical method presented in this report should be compared.

3.2.6.2 If the previous method seems to be a practical engineering approach, a characteristic "damping factor" related to the ratio of load and parachute size, weight of the load, and type of parachute will be established. This will enable rapid and relatively simple calculation of the amplitude time and frequency velocity relationships for a parachute and store combination.

REFERENCES

1. Housner, George, W. and Hudson, Donald E.:
Applied Mechanics - Dynamics, D. Van Nostrand
Company, Inc., New York, 1958.
2. Heinrich, Helmut G. and Haak, Eugene L.:
Stability and Drag of Parachutes with Varying
Effective Porosity, ASD Technical Report 62-100,
December, 1961.
3. Von Karman, Theodore: Notes on Analysis of the
Opening Shock of Parachutes at Various Altitudes,
Army Air Corps Scientific Advisory Group,
24 August 1945.

$$A_{y,c}' = \frac{I_c'}{I_y} = \frac{K \cancel{4} \pi^2 (I_w^2 - I_d^2) - M_d w L^2}{\frac{8}{15} \pi (\frac{Dp}{2})^5}$$

6" HEMISPHERE MODEL	① RUN NO.	② $\frac{K}{4\pi^2} \times 10^{-4}$ dyne-cm	③ T_w^2 sec ²	④ T_d^2 sec ²	⑤ $(I_w^2 - I_d^2) \times 10^{-3}$ sec ²	⑥ $(I_c' + I_{2s}') \times 10^{-3}$ gm-cm ²	⑦ $M_d w$ gm	⑧ L cm	⑨ L^2 cm ²	⑩ $I_{2s} \times 10^{-3}$ gm-cm ²	⑪ $I_c' \times 10^{-3}$ gm-cm ²	⑫ $\frac{8}{15} \pi (\frac{Dp}{2})^5 \times 10^{-3}$	⑬ $A_{y,c}'$ (11)/(12)
1 1/4" ATTACHED SPHERES	1	8.900	1.1274	.9596	.1678	14.93	16.80	16.07	258.3	4.340	10.59	46.50	.228
	2	8.900	1.1278	.9616	.1662	14.79	16.80	16.07	258.3	4.340	10.45	46.50	.225
	3	8.900	1.1287	.9551	.1736	15.45	16.80	16.07	258.3	4.340	11.11	46.50	.239
	4	8.900	1.1204	.9596	.1608	14.31	16.80	16.07	258.3	4.340	9.97	46.50	.214
Average $A_{y,c}'$ For Oscillations About C.G. of Enclosed Volume = .221 Average $A_{y,c}'$ For Oscillations About C.G. of Canopy Surface* = .363													
1 1/2" ATTACHED SPHERES	1	8.900	1.8028	1.5952	.2076	18.48	28.95	16.39	268.7	7.778	10.70	46.50	.230
	2	8.900	1.8152	1.6030	.2122	18.89	28.95	16.39	268.7	7.778	11.11	46.50	.239
	3	8.900	1.8285	1.6073	.2222	18.78	28.95	16.39	268.7	7.778	12.00	46.50	.258
	4	8.900	1.8279	1.6152	.2127	18.93	28.95	16.39	268.7	7.778	11.15	46.50	.240
Average $A_{y,c}'$ For Oscillations About C. G. of Enclosed Volume = .242 Average $A_{y,c}'$ For Oscillations About C. G. of Canopy Surface* = .364													

TABLE 4-1. CALCULATION OF THE DIMENSIONLESS REPRESENTATION OF THE APPARENT MOMENT OF INERTIA FOR THE 6" HEMISPHERICAL CANOPY

*Data was presented in Progress Report No. 22 in a different dimensionless form, that is here presented in the form $A_{y,c}'$.

$$A_{y,c} = \frac{I'_c}{I_y} = \frac{K \cancel{4\pi^2} (T_w^2 - T_q^2) - M_{dw} L^2}{\frac{8}{15} \pi (D_p)^5}$$

5' HEMISPHERE MODEL	① RUN NO.	② $K \times 10^{-4}$ $\frac{4\pi^2}{L^2}$ dyne-cm	③ T_w^2 sec ²	④ T_q^2 sec ²	⑤ $(T_w^2 - T_q^2)(I'_c + I'_{qs})$ $\frac{8}{15} \pi (D_p)^5$ sec ² × 10 ⁻³ gm-cm ²	⑥ $I'_c + I'_{qs}$ gm-cm ²	⑦ M_{dw} gm	⑧ L cm	⑨ L^2 cm ²	⑩ $I'_{qs} \times 10^{-3}$ gm-cm ²	⑪ $I'_c \times 10^{-3}$ gm-cm ²	⑫ $\frac{8}{15} \pi (D_p)^5$ gm-cm ²	⑬ $A_{y,c}$ (11)/(12)
1 1/4" ATTACHED SPHERES	1	8.900	.7987	.7155	.0832	7.405	16.80	14.76	217.9	3.661	3.744	15.24	.246
	2	8.900	.8005	.7144	.0811	7.218	16.80	14.76	217.9	3.661	3.557	15.24	.233
	3	8.900	.8010	.7176	.0834	7.423	16.80	14.76	217.9	3.661	3.762	15.24	.247
	4	8.900	.8008	.7201	.0807	7.182	16.80	14.76	217.9	3.661	3.521	15.24	.231
Average $A_{y,c}$ For Oscillations About C.G. of Enclosed Volume = .239 Average $A_{y,c}$ For Oscillations About C.G. of Canopy Surface* = .371													
1 1/2" ATTACHED SPHERES	1	8.900	.8100	.7295	.0855	7.165	28.95	11.35	128.8	3.730	3.435	15.24	.225
	2	8.900	.8131	.7281	.0850	7.565	28.95	11.35	128.8	3.730	3.835	15.24	.252
	3	8.900	.8127	.7278	.0849	7.556	28.95	11.35	128.8	3.730	3.826	15.24	.251
	4	8.900	.8127	.7293	.0834	7.423	28.95	11.35	128.8	3.730	3.693	15.24	.242
	5	8.900	.8089	.7281	.0808	7.191	28.95	11.35	128.8	3.730	3.461	15.24	.227
Average $A_{y,c}$ For Oscillations About C.G. of Enclosed Volume = .239 Average $A_{y,c}$ For Oscillations About C.G. of Canopy Surface* = .373													

TABLE 4-2. CALCULATION OF THE DIMENSIONLESS REPRESENTATION OF THE APPARENT MOMENT OF INERTIA FOR THE 5" HEMISPHERICAL CANOPY

*Data was presented in Progress Report No. 22 in a different dimensionless form, that is here presented in the form $A_{y,c}$.

$$A_{y,c'} = \frac{I'_c}{I_y} = \frac{K}{4\pi^2} \frac{(T_w^2 - T_d^2) - M_{dw} L^2}{\frac{8}{15} \pi (\frac{Dp}{2})^5}$$

6' CIRCULAR FLAT MODEL	① RUN NO.	② $\frac{K}{4\pi^2} \times 10^{-4}$ dyne-cm	③ T_w^2 sec ²	④ T_d^2 sec ²	⑤ $(T_w^2 - T_d^2) \times 10^{-3}$ sec ²	⑥ $(I'_c + I'_{2s}) \times 10^{-3}$ gm-cm ²	⑦ M_{dw} gm	⑧ L cm	⑨ L^2 cm ²	⑩ $I'_{2s} \times 10^{-3}$ gm-cm ²	⑪ $I'_c \times 10^{-3}$ gm-cm ²	⑫ $\frac{8}{15} \pi (\frac{Dp}{2})^5$ in ³	⑬ $A_{y,c'}$
1 1/4" ATTACHED SPHERES	1	8.900	.6719	.5229	.1490	13.26	16.80	12.58	158.3	2.66	10.60	46.50	.228
	2	8.900	.6693	.5249	.1444	12.85	16.80	12.58	158.3	2.66	10.19	46.50	.219
	3	8.900	.6670	.5246	.1424	12.67	16.80	12.58	158.3	2.66	10.02	46.50	.215
	4	8.900	.6648	.5262	.1436	12.78	16.80	12.58	158.3	2.66	10.12	46.50	.218
	5	8.900	.6724	.5262	.1462	13.01	16.80	12.58	158.3	2.66	10.35	46.50	.223
Average $A_{y,c'} = .221$													
1 1/2" ATTACHED SPHERES	1	8.900	1.0980	.9243	.1737	15.46	28.95	12.90	166.4	4.82	10.64	46.50	.229
	2	8.900	1.0900	.9176	.1724	15.34	28.95	12.90	166.4	4.82	10.52	46.50	.226
	3	8.900	1.1022	.9264	.1756	15.63	28.95	12.90	166.4	4.82	10.81	46.50	.233
	4	8.900	1.0860	.9216	.1644	14.63	28.95	12.90	166.4	4.82	9.81	46.50	.211
Average $A_{y,c'} = .225$													

TABLE 4-3. CALCULATION OF THE DIMENSIONLESS REPRESENTATION OF THE APPARENT MOMENT OF INERTIA FOR THE 6' CIRCULAR FLAT CANOPY

$$A_{yc'} = \frac{I'_{cy}}{I_y} = \frac{K \cancel{4\pi^2} (I_w^2 - I_d^2) - M_{dw} L^2}{\frac{8}{15} \pi (\frac{Dp}{2})^5}$$

6" RIBLESS GUIDE SURFACE MODEL	① RUN NO.	② $\frac{K}{4\pi^2} \times 10^{-4}$ dyne-cm	③ T_w^2 sec ²	④ T_d^2 sec ²	⑤ $(T_w^2 - T_d^2) \times 10^{-3}$ sec ²	⑥ $(I_w^2 - I_d^2) \times 10^{-3}$ gm-cm ²	⑦ M_{dw} gm	⑧ L cm	⑨ L^2 cm ²	⑩ $I'_2 \times 10^{-3}$ gm-cm ²	⑪ $I'_c \times 10^{-3}$ gm-cm ²	⑫ $\frac{8}{15} \pi (\frac{Dp}{2})^5 I_y \times 10^{-3}$	⑬ $A_{yc'}$
1" 1/4 ATTACHED SPHERES	1	8.77	.9366	.7783	.1583	13.88	16.80	15.16	229.8	3.86	10.02	43.88	.228
	2	8.77	.9442	.7866	.1576	13.82	16.80	15.16	229.8	3.86	9.96	43.88	.227
	3	8.77	.9409	.7845	.1564	13.72	16.80	15.16	229.8	3.86	9.86	43.88	.225
	4	8.77	.9465	.7862	.1603	14.06	16.80	15.16	229.8	3.86	10.20	43.88	.232
Average $A_{y,c'} = .228$													
1" 1/2 ATTACHED SPHERES	1	8.77	1.5346	1.3442	.1904	16.70	28.95	15.64	244.6	7.08	9.62	43.88	.219
	2	8.77	1.5349	1.3430	.1919	16.83	28.95	15.64	244.6	7.08	9.75	43.88	.222
	3	8.77	1.5302	1.3396	.1906	16.71	28.95	15.64	244.6	7.08	9.63	43.88	.220
	4	8.77	1.5366	1.3396	.1970	17.28	28.95	15.64	244.6	7.08	10.20	43.88	.232
Average $A_{y,c'} = .223$													

TABLE 4-4. CALCULATION OF THE DIMENSIONLESS REPRESENTATION OF THE APPARENT MOMENT OF INERTIA FOR THE '6" RIBLESS GUIDE SURFACE CANOPY

30 ft³/ft²-min nominal porosity

q	ω_n^2	n	ω^2	$T=2\pi/\omega$	T_{exp}
1/2	89.2	1.26	87.6	0.672	0.688
1	179	1.87	175.5	0.474	0.494
1-1/2	268	2.56	261.5	0.388	0.397
2	358	3.24	347.5	0.336	0.340
2-1/2	446	3.63	432.8	0.300	0.307
3	535	4.38	515.8	0.277	0.270

60-90 ft³/ft²-min nominal porosity

q	ω_n^2	n	ω^2	$T=2\pi/\omega$	T_{exp}
1/2	101.4	1.45	99.3	0.630	0.620
1	202.8	2.11	198.4	0.445	0.470
1-1/2	304.2	2.99	295.3	0.365	0.372
2	405.6	3.62	392.5	0.317	0.336
2-1/2	507.0	4.211	489.3	0.284	0.308

120 ft³/ft²-min nominal porosity

q	ω_n^2	n	ω^2	$T=2\pi/\omega$	T_{exp}
1/2	132	1.89	128.4	0.554	0.607
1	263	2.75	255.4	0.393	0.456
1-1/2	395	3.81	380.5	0.322	0.364
2	528	5.08	502.2	0.280	0.299
2-1/2	658	5.92	622.9	0.252	0.278
3	788	7.57	730.7	0.235	0.234

TABLE 4-5. PERIOD, DAMPING FACTOR, AND ANGULAR FREQUENCY AS A FUNCTION OF DYNAMIC PRESSURE

TABLE 4-6. DIFFERENTIAL EQUATIONS AND SOLUTIONS

30 ft³/ft²-min nominal porosity

$$\underline{q = 1/2" H_2O}$$

$$\ddot{\alpha} + 2.52 \dot{\alpha} + 89.2 \alpha = 0$$

$$\alpha = e^{-1.26t} (\alpha_0 \cos 9.35t + 0.135 \alpha_0 \sin 9.35t)$$

$$\underline{q = 1" H_2O}$$

$$\ddot{\alpha} + 3.74 \dot{\alpha} + 179 \alpha = 0$$

$$\alpha = e^{-1.87t} (\alpha_0 \cos 13.3t + 0.147 \alpha_0 \sin 13.3t)$$

$$\underline{q = 1-1/2" H_2O}$$

$$\ddot{\alpha} + 5.12 \dot{\alpha} + 268 \alpha = 0$$

$$\alpha = e^{-2.56t} (\alpha_0 \cos 16.2t + 0.158 \alpha_0 \sin 16.2t)$$

$$\underline{q = 2" H_2O}$$

$$\ddot{\alpha} + 6.48 \dot{\alpha} + 358 \alpha = 0$$

$$\alpha = e^{-3.24t} (\alpha_0 \cos 18.6t + 0.174 \alpha_0 \sin 18.6t)$$

$$\underline{q = 2-1/2" H_2O}$$

$$\ddot{\alpha} + 7.26 \dot{\alpha} + 446 \alpha = 0$$

$$\alpha = e^{-3.63t} (\alpha_0 \cos 20.8t + 0.175 \alpha_0 \sin 20.8t)$$

$$\underline{q = 3" H_2O}$$

$$\ddot{\alpha} + 8.76 \dot{\alpha} + 535 \alpha = 0$$

$$\alpha = e^{-4.38t} (\alpha_0 \cos 22.7t + 0.193 \alpha_0 \sin 22.7t)$$

TABLE 4-6 CONT.

60-90 ft³/ft²-min nominal porosity

$q = 1/2" H_2O$

$$\ddot{\alpha} + 2.90\dot{\alpha} + 101.4\alpha = 0$$

$$\alpha = e^{-1.45t} (\alpha_0 \cos 9.96t + 0.146 \alpha_0 \sin 9.96t)$$

$q = 1" H_2O$

$$\ddot{\alpha} + 4.22\dot{\alpha} + 202.8\alpha = 0$$

$$\alpha = e^{-2.11t} (\alpha_0 \cos 14.1t + 0.15 \alpha_0 \sin 14.1t)$$

$q = 1-1/2" H_2O$

$$\ddot{\alpha} + 5.98\dot{\alpha} + 304.2\alpha = 0$$

$$\alpha = e^{-2.99t} (\alpha_0 \cos 17.2t + 0.174 \alpha_0 \sin 17.2t)$$

$q = 2" H_2O$

$$\ddot{\alpha} + 7.24\dot{\alpha} + 405.6\alpha = 0$$

$$\alpha = e^{-3.62t} (\alpha_0 \cos 19.8t + 0.183 \alpha_0 \sin 19.8t)$$

$q = 2-1/2" H_2O$

$$\ddot{\alpha} + 8.42\dot{\alpha} + 507\alpha = 0$$

$$\alpha = e^{-4.21t} (\alpha_0 \cos 22.5t + 0.187 \alpha_0 \sin 22.5t)$$

TABLE 4-6 CONT

120 ft³/ft²-min nominal porosity

$$\underline{q = 1/2" H_2O}$$

$$\ddot{\alpha} + 3.78 \dot{\alpha} + 132 \alpha = 0$$

$$\alpha = e^{-1.89t} (\alpha_0 \cos 11.3t + 0.167 \alpha_0 \sin 11.3t)$$

$$\underline{q = 1" H_2O}$$

$$\ddot{\alpha} + 5.5 \dot{\alpha} + 263 \alpha = 0$$

$$\alpha = e^{-2.75t} (\alpha_0 \cos 16.0t + 0.172 \alpha_0 \sin 16.0t)$$

$$\underline{q = 1-1/2" H_2O}$$

$$\ddot{\alpha} + 7.62 \dot{\alpha} + 395 \alpha = 0$$

$$\alpha = e^{-3.81t} (\alpha_0 \cos 19.5t + 0.195 \alpha_0 \sin 19.5t)$$

$$\underline{q = 2" H_2O}$$

$$\ddot{\alpha} + 10.16 \dot{\alpha} + 528 \alpha = 0$$

$$\alpha = e^{-5.08t} (\alpha_0 \cos 22.4t + 0.227 \alpha_0 \sin 22.4t)$$

$$\underline{q = 2-1/2" H_2O}$$

$$\ddot{\alpha} + 11.84 \dot{\alpha} + 658 \alpha = 0$$

$$\alpha = e^{-5.92t} (\alpha_0 \cos 25.0t + 0.237 \alpha_0 \sin 25.0t)$$

$$\underline{q = 3" H_2O}$$

$$\ddot{\alpha} + 15.14 \dot{\alpha} + 788 \alpha = 0$$

$$\alpha = e^{-7.57t} (\alpha_0 \cos 27.0t + 0.280 \alpha_0 \sin 27.0t)$$

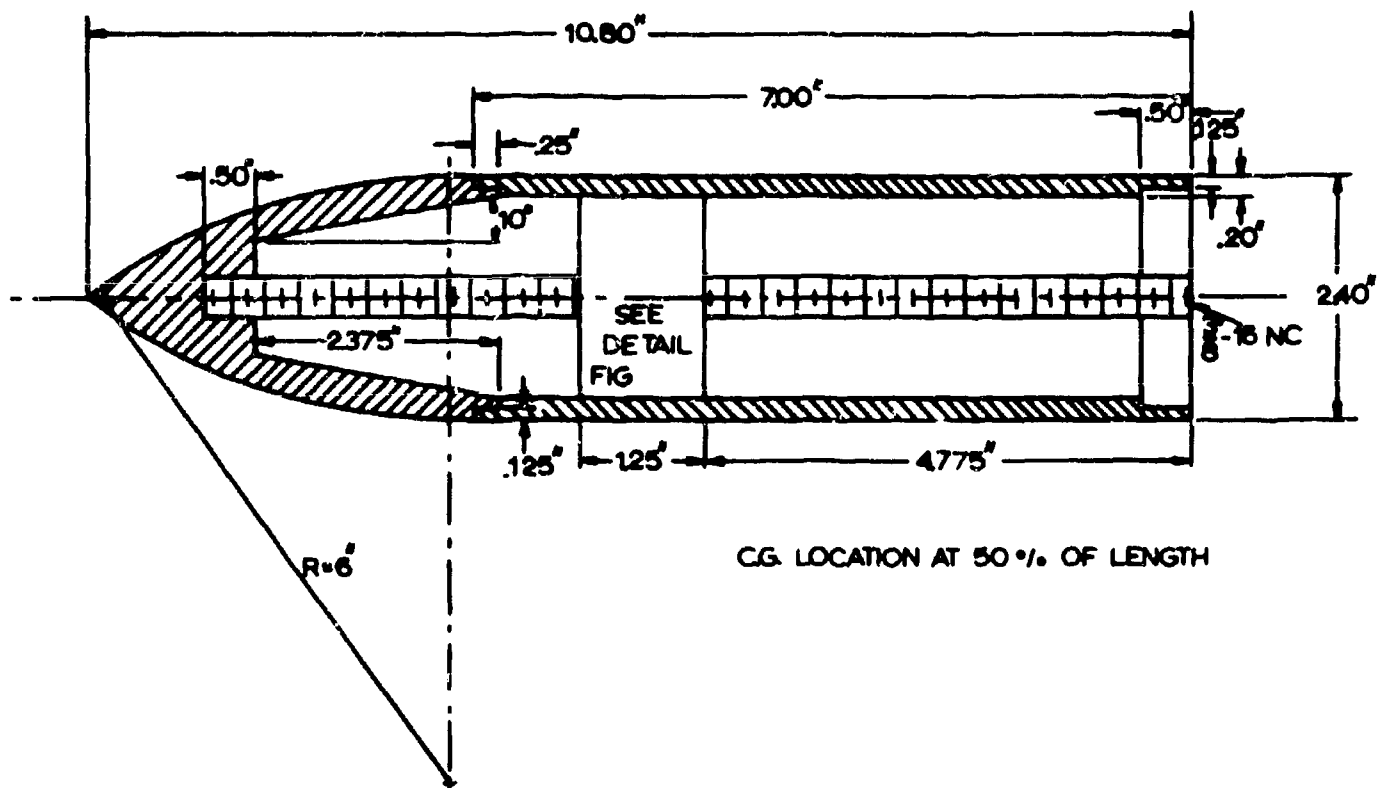


FIG 4-1. DIMENSIONS OF OGIVE CYLINDER MODEL

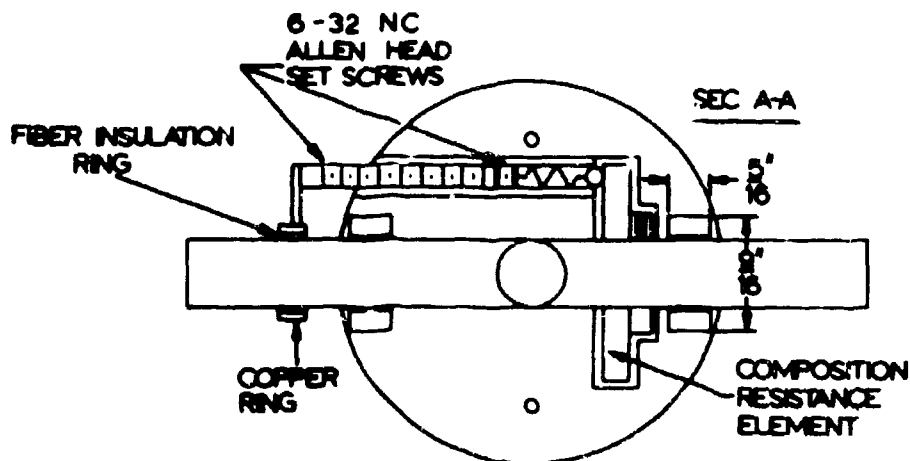
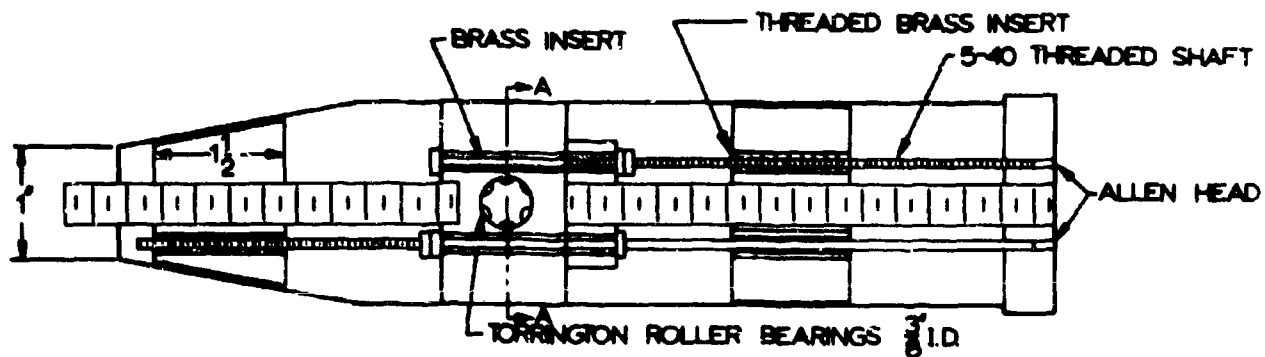


FIG 4-2. CONSTRUCTION DETAILS OF OGIVE CYLINDER MODEL

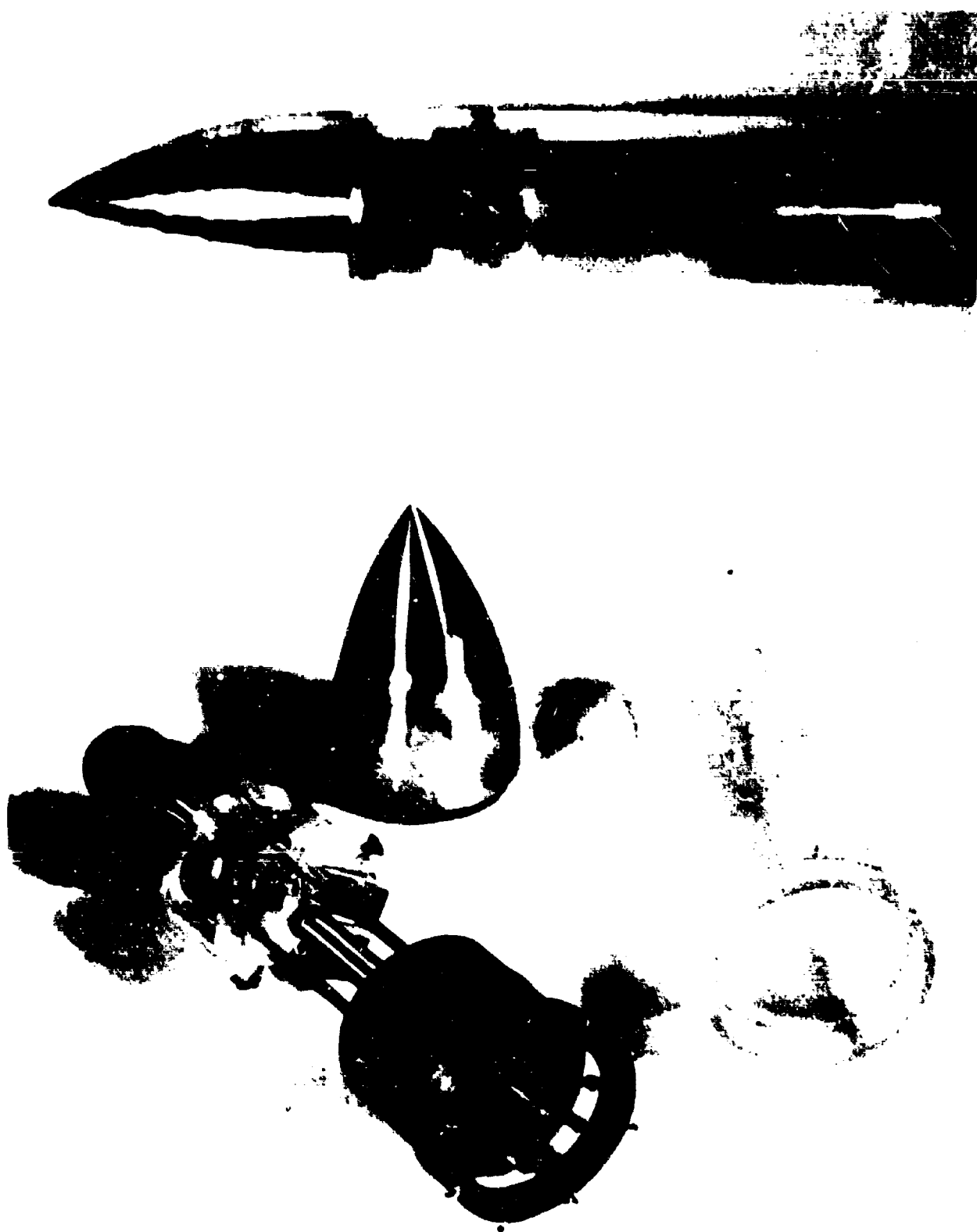


FIG 4-3. OGIVE CYLINDER MODEL

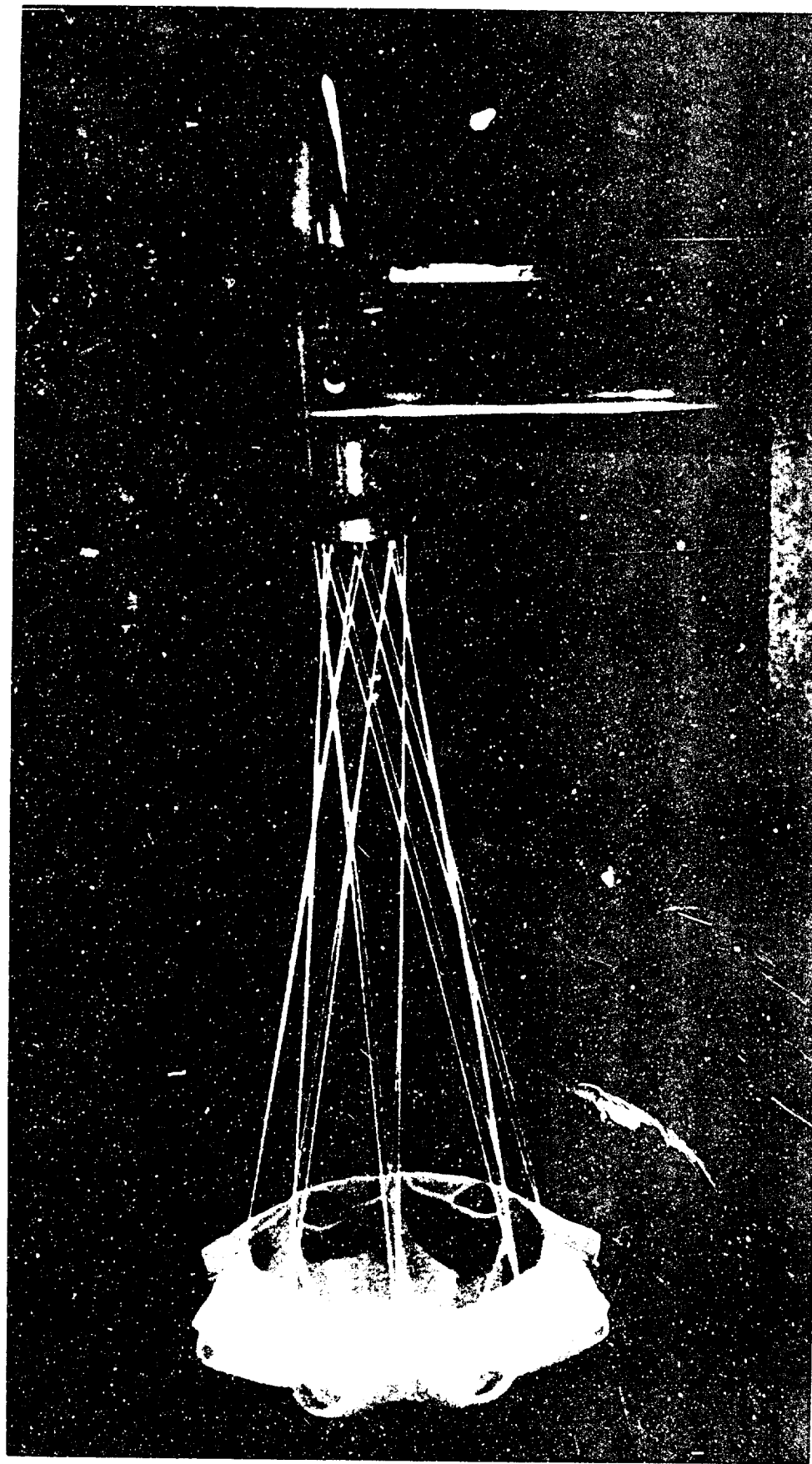
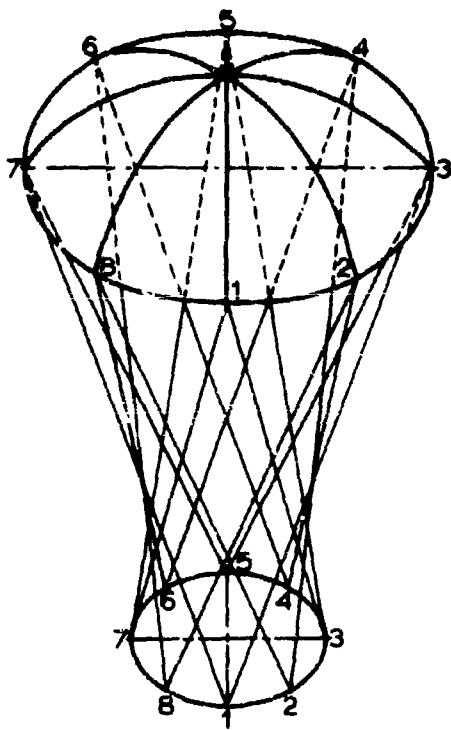


FIG 4-4. WIND TUNNEL TEST ARRANGEMENT



CONNECT POINT	TO POINTS
1	7,3
2	8,4
3	1,5
4	2,6
5	3,7
6	4,8
7	5,1
8	6,2
ON SKIRT	ON BOTTOM

FIG 4-5. GEODETIC SUSPENSION SYSTEM

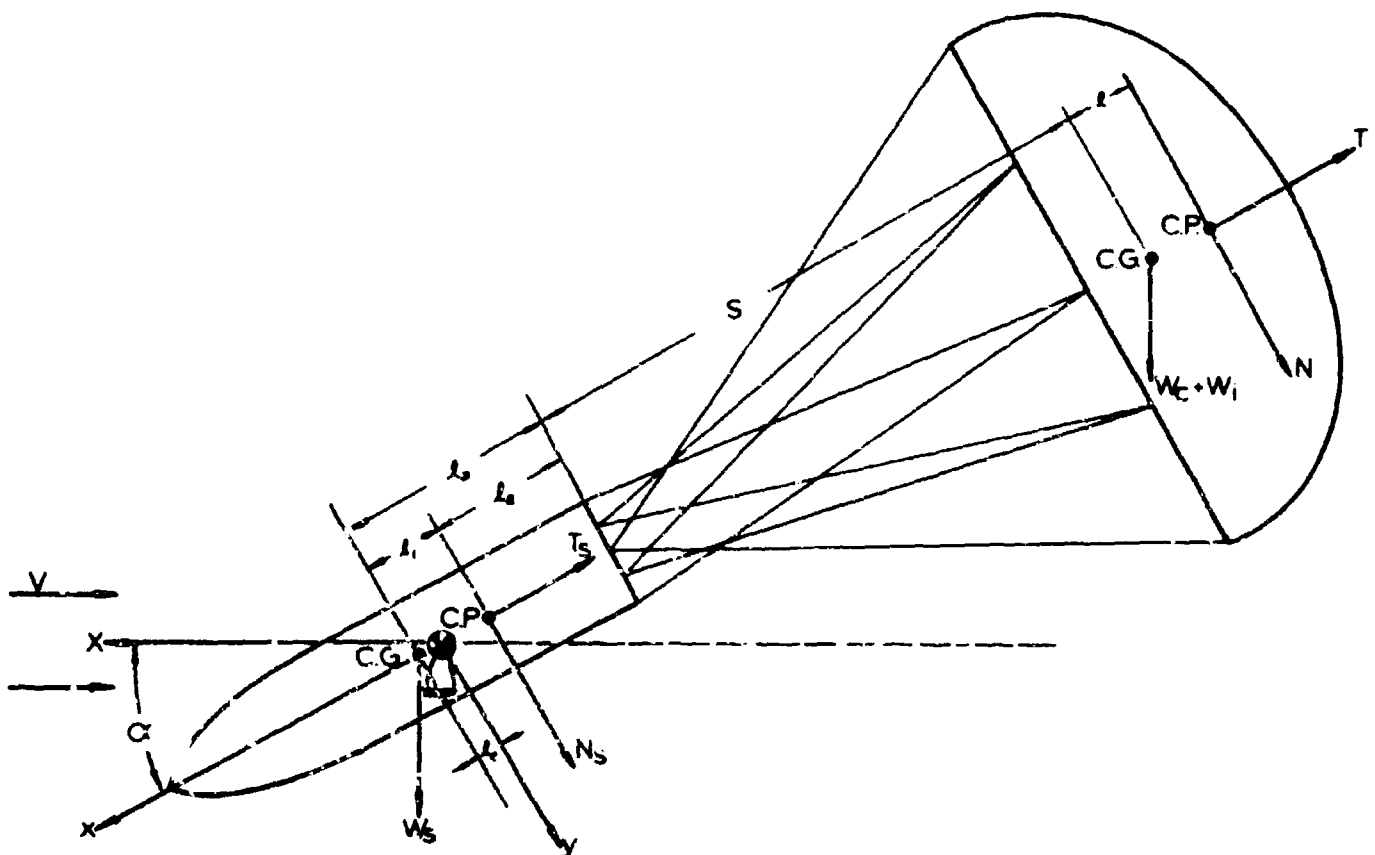


FIG 4-6. FREE BODY DIAGRAM OF PARACHUTE AND STORE

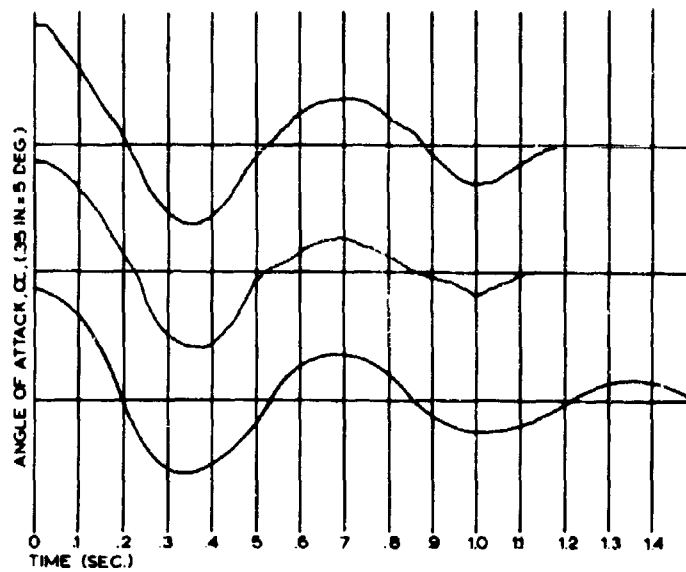


FIG 4-7. OSCILLATION HISTORY OF OGIVE CYLINDER
 $q = 1/2$ IN H_2O NOM. POR. 30 FT^3/FT^2-MIN

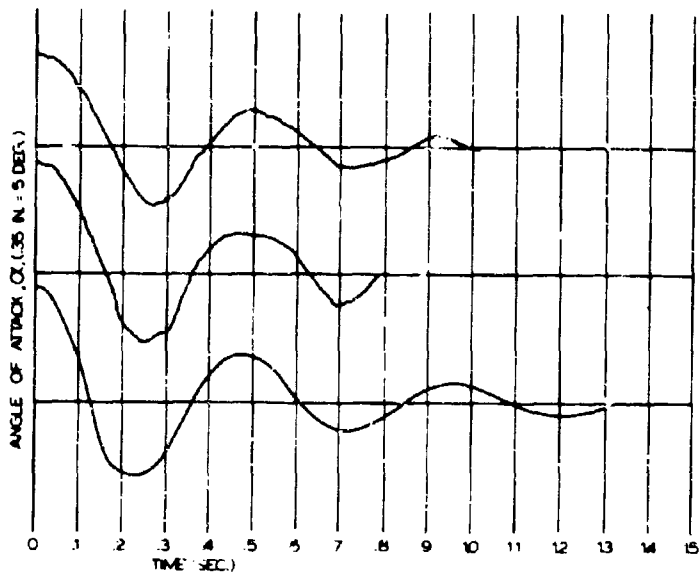


FIG 4-8. OSCILLATION HISTORY OF OGIVE CYLINDER
 $q = 1$ IN H_2O NOM. POR. 30 FT^3/FT^2-MIN

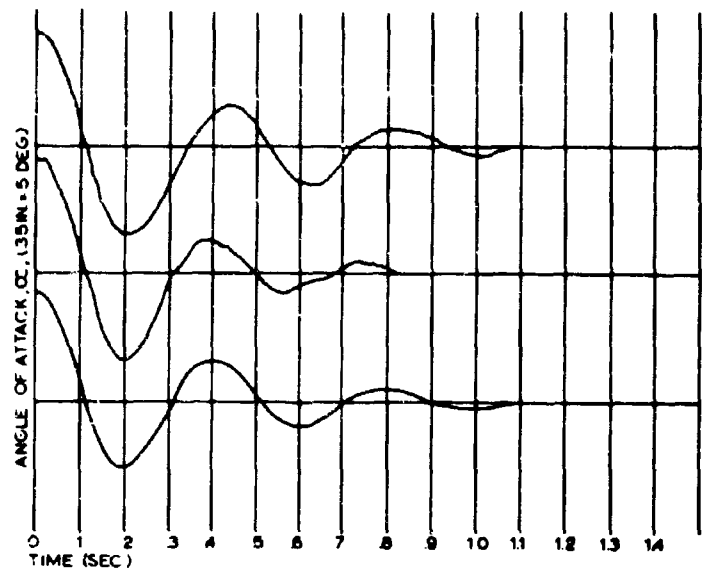


FIG 4-9. OSCILLATION HISTORY OF OGIVE CYLINDER
 $q = 1/2$ IN H_2O NOM. POR. 30 FT^3/FT^2-MIN

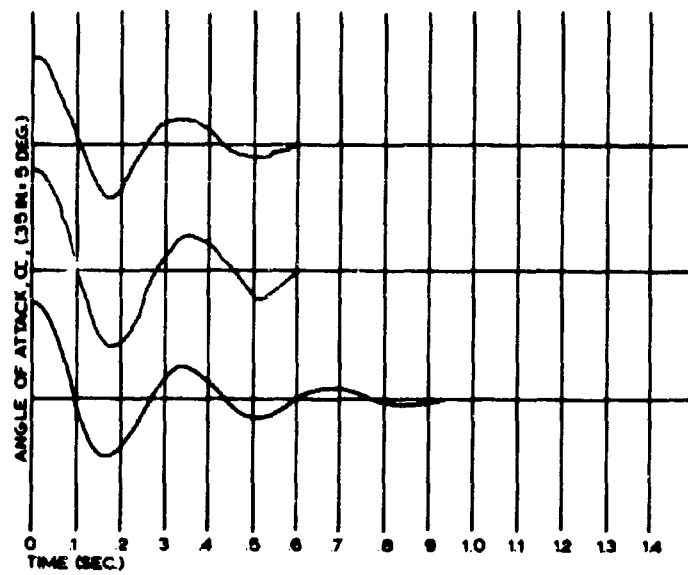


FIG 410 OSCILLATION HISTORY OF OGIVE CYLINDER
 $q = 2 \text{ IN } H_2O$ NOM. POR. $30 \text{ FT}^3/\text{FT}^2\text{-MIN}$

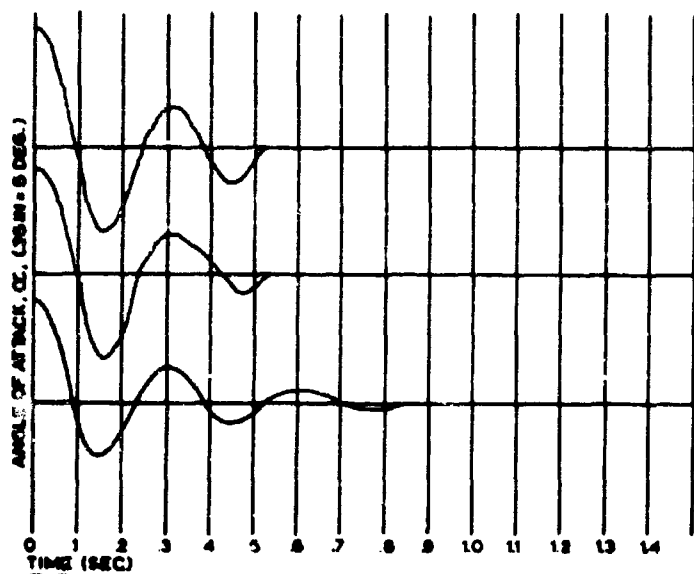


FIG 411 OSCILLATION HISTORY OF OGIVE CYLINDER
 $q = 2 \text{ 1/2 IN } H_2O$ NOM. POR. $30 \text{ FT}^3/\text{FT}^2\text{-MIN}$

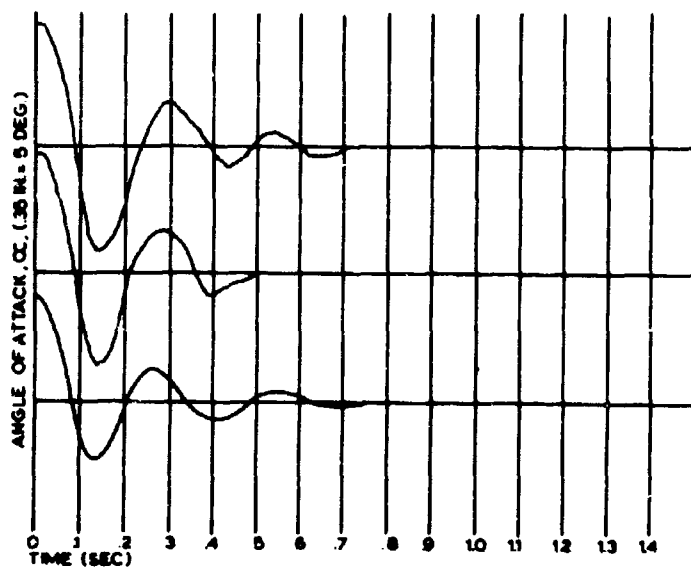


FIG 412 OSCILLATION HISTORY OF OGIVE CYLINDER
 $q = 3 \text{ IN } H_2O$ NOM. POR. $30 \text{ FT}^3/\text{FT}^2\text{-MIN}$

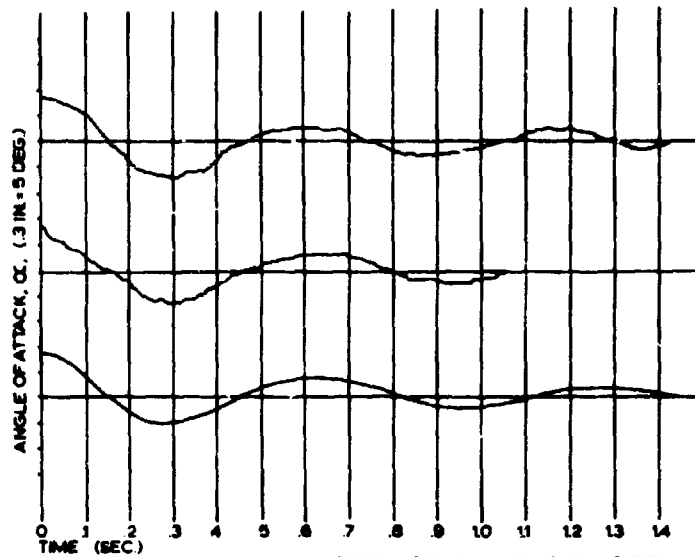


FIG 4-13. OSCILLATION HISTORY OF OGIVE CYLINDER

$q = 1/2$ IN. H_2O NOM. POR. 60-90 FT^3/FT^2 MIN.

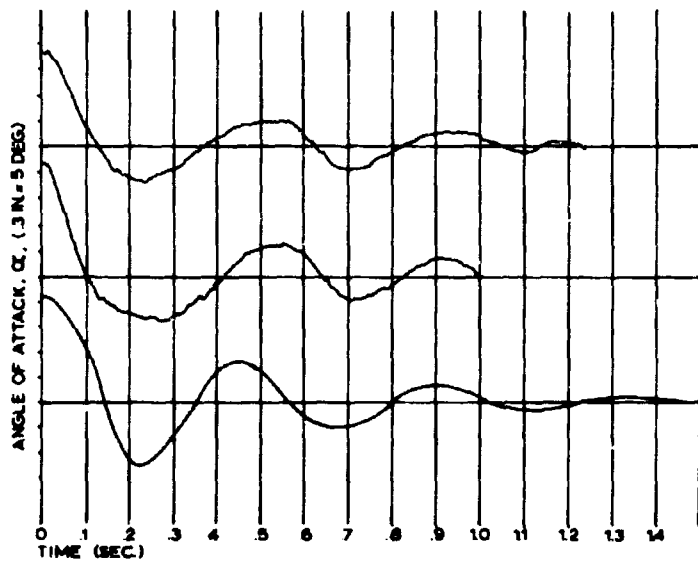


FIG 4-14. OSCILLATION HISTORY OF OGIVE CYLINDER

$q = 1$ IN. H_2O NOM. POR. 60-90 FT^3/FT^2 MIN.

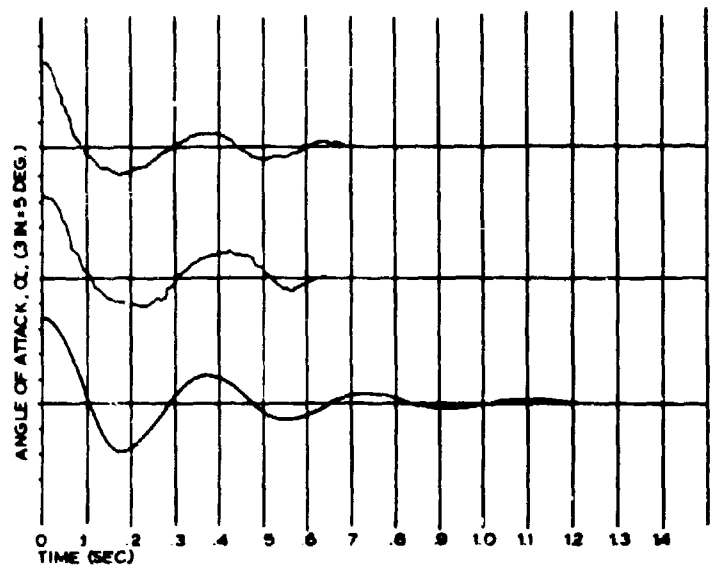


FIG 4-15. OSCILLATION HISTORY OF OGIVE CYLINDER

$q = 1 1/2$ IN. H_2O NOM. POR. 60-90 FT^3/FT^2 MIN.

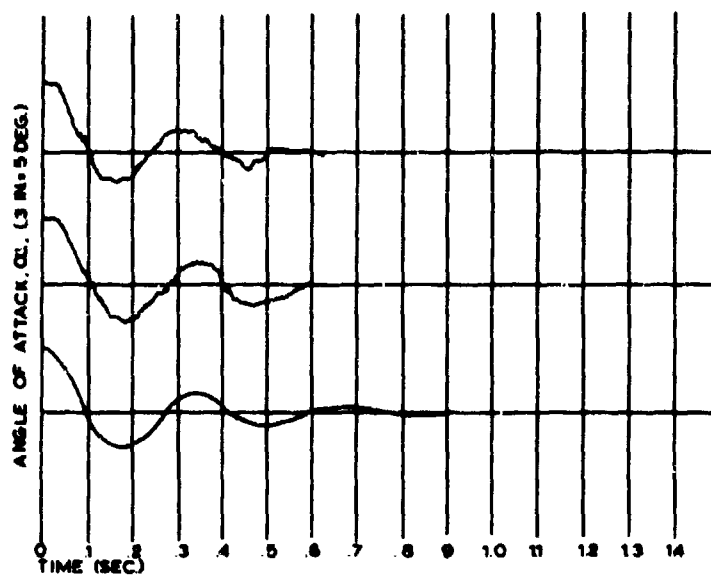


FIG 4-16. OSCILLATION HISTORY OF OGIVE CYLINDER
 $q = 2 \text{ IN. H}_2\text{O}$ NOM FOR $60-90 \text{ FT}^3/\text{FT}^2 \cdot \text{MIN}$

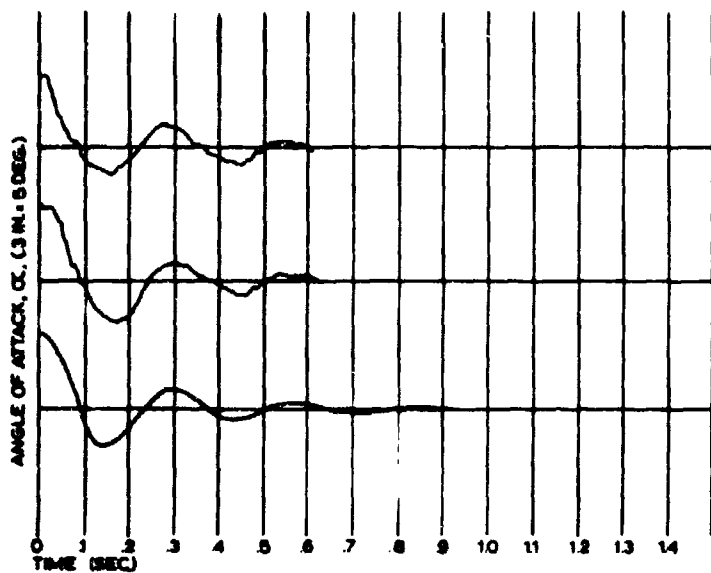


FIG 4-17. OSCILLATION HISTORY OF OGIVE CYLINDER
 $q = 2.12 \text{ IN. H}_2\text{O}$ NOM FOR $60-90 \text{ FT}^3/\text{FT}^2 \cdot \text{MIN}$

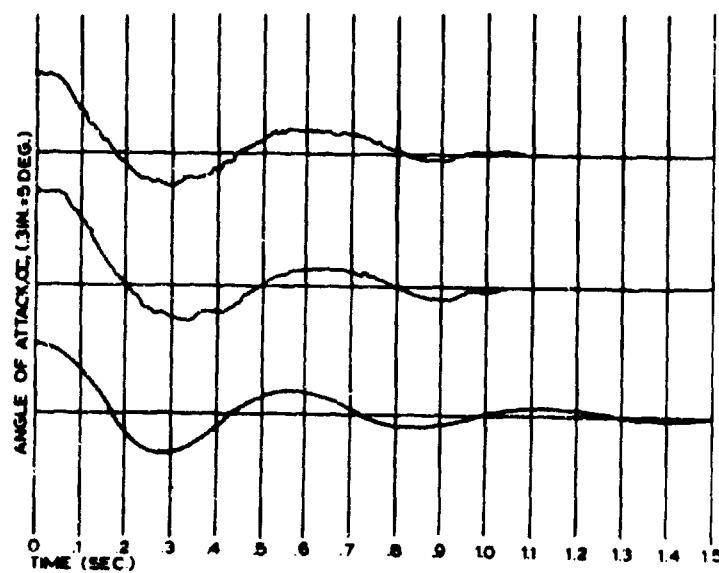


FIG 4-18. OSCILLATION HISTORY OF OGIVE CYLINDER
 $q = 1/2 \text{ IN. H}_2\text{O}$ NOM. FOR $120 \text{ FT}^3/\text{FT}^2 \cdot \text{MIN}$

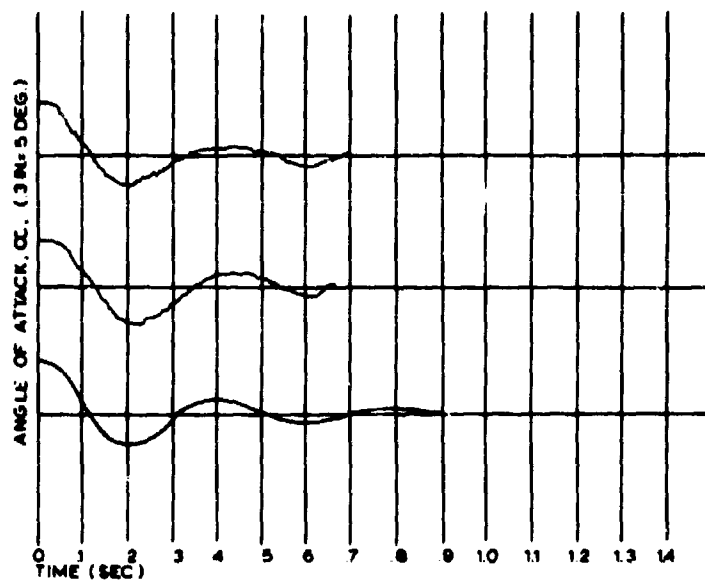


FIG 4-19. OSCILLATION HISTORY OF OGIVE CYLINDER
 $q=1$ IN H_2O NOM FOR $120 \text{ FT}^3/\text{FT}^2/\text{MIN}$

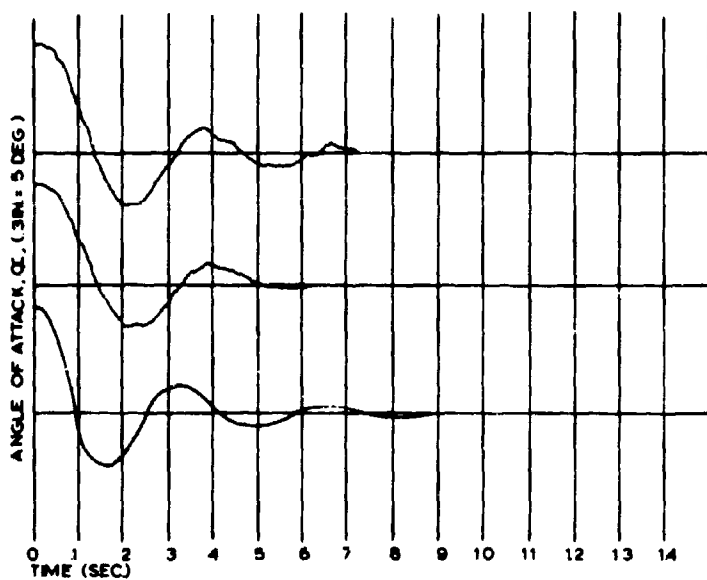


FIG 4-20. OSCILLATION HISTORY OF OGIVE CYLINDER
 $q=1/2$ IN H_2O NOM FOR $120 \text{ FT}^3/\text{FT}^2/\text{MIN}$

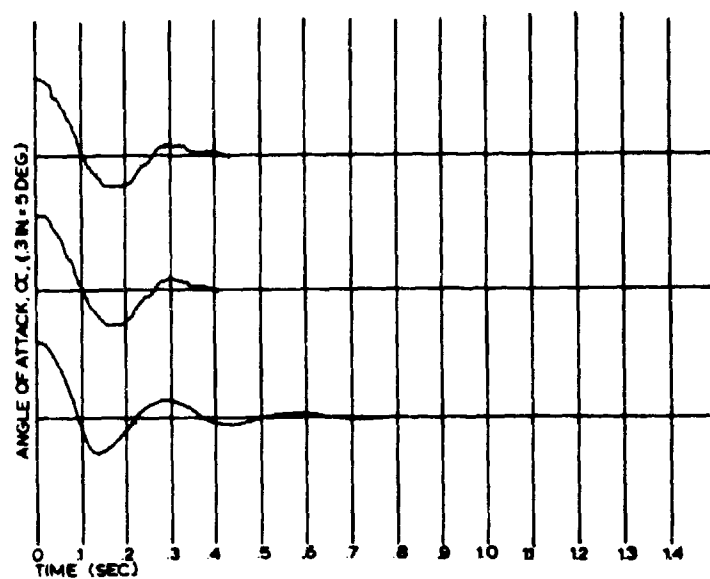


FIG 4-21. OSCILLATION HISTORY OF OGIVE CYLINDER
 $q=2$ IN H_2O NOM FOR $120 \text{ FT}^3/\text{FT}^2/\text{MIN}$

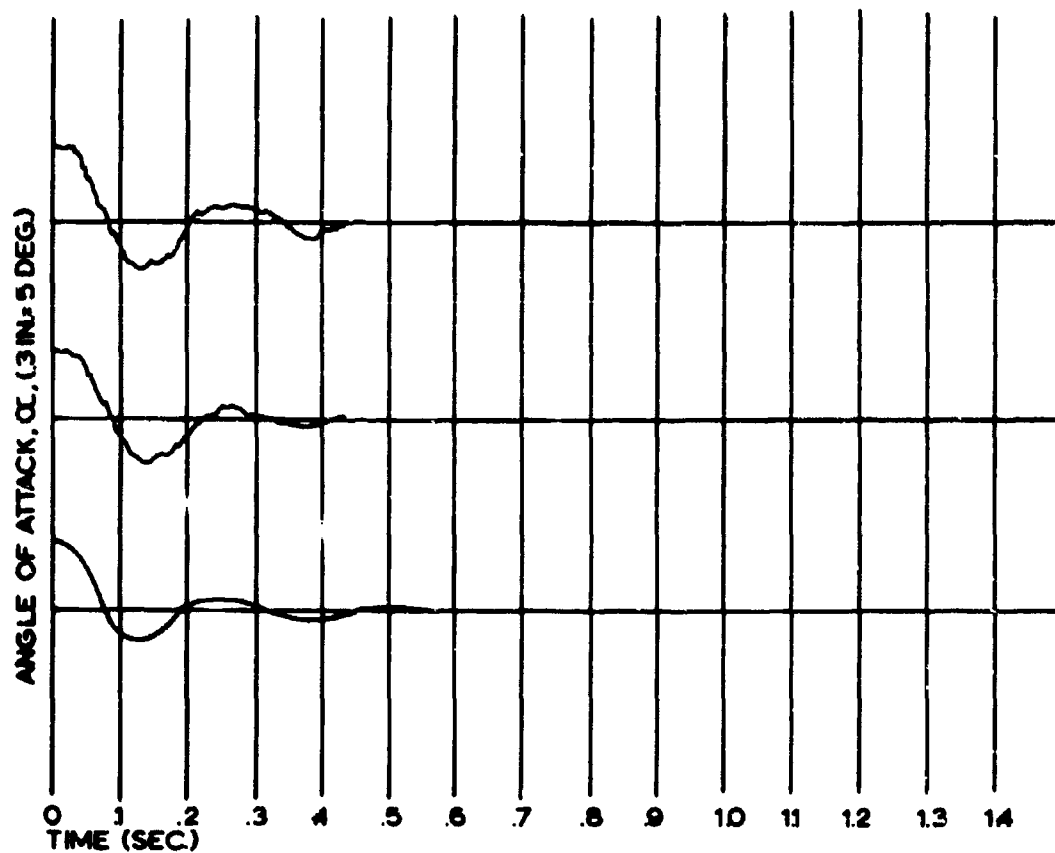


FIG 422. OSCILLATION HISTORY OF OGIVE CYLINDER
 $q = 2 \text{ V}_2 \text{ IN}$ NOM. POR. $120 \text{ FT}^3/\text{FT}^2 \text{ MIN.}$

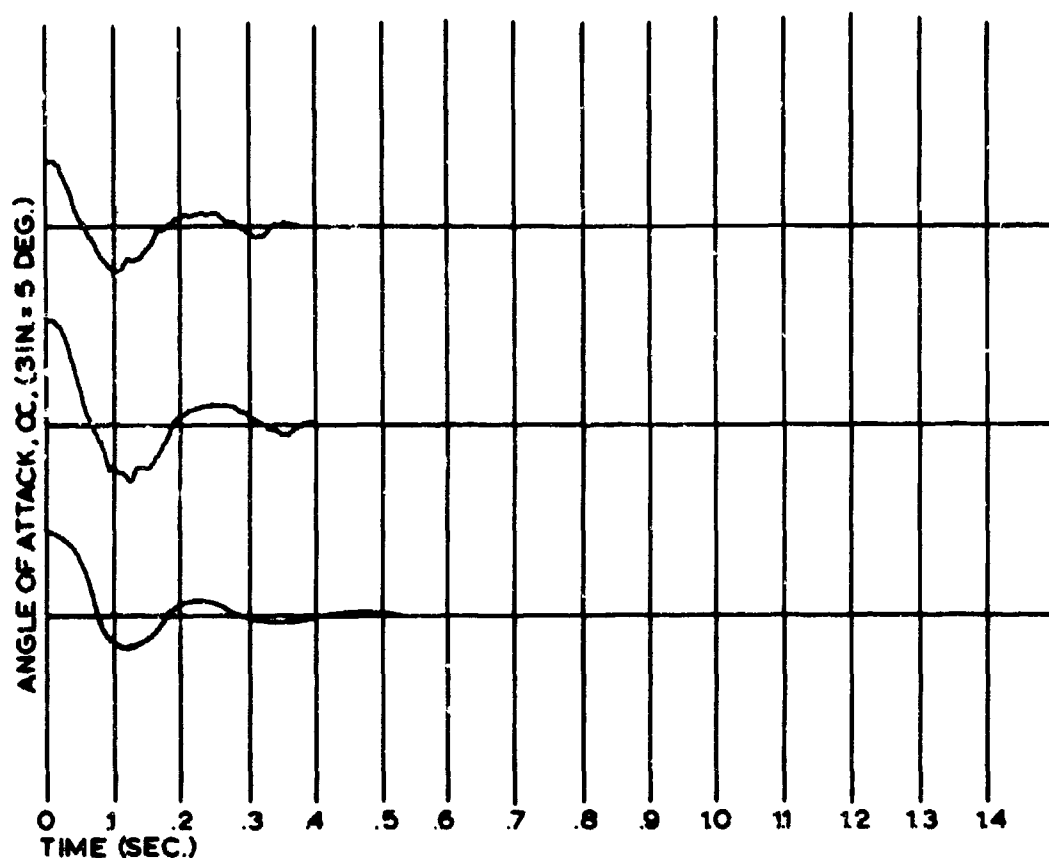


FIG 423. OSCILLATION HISTORY OF OGIVE CYLINDER
 $q = 3 \text{ IN H}_2\text{O}$ NOM. POR. $120 \text{ FT}^3/\text{FT}^2 \text{ MIN.}$

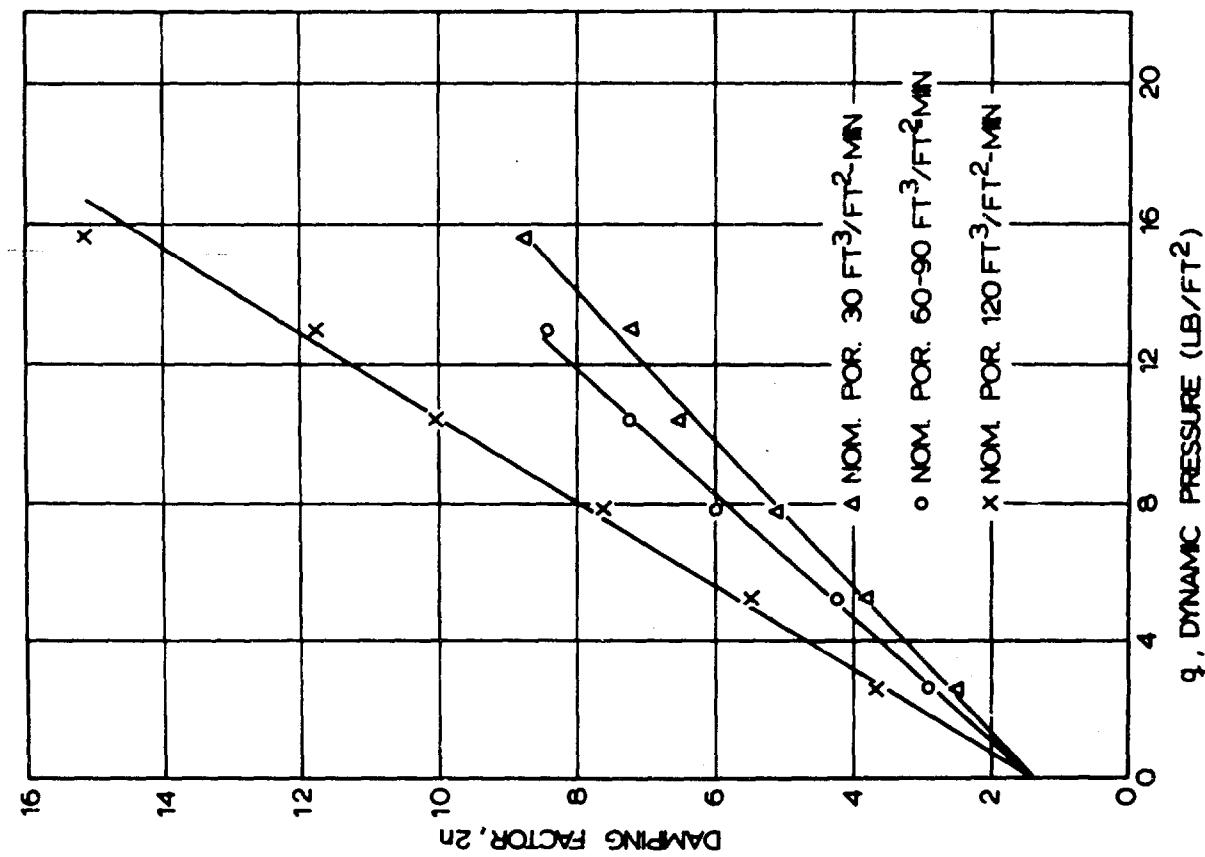


FIG 4-24. EXPERIMENTAL DAMPING FACTOR
VS DYNAMIC PRESSURE

$$I_S^* = 0.01278 \text{ SLUG-FT}^2$$

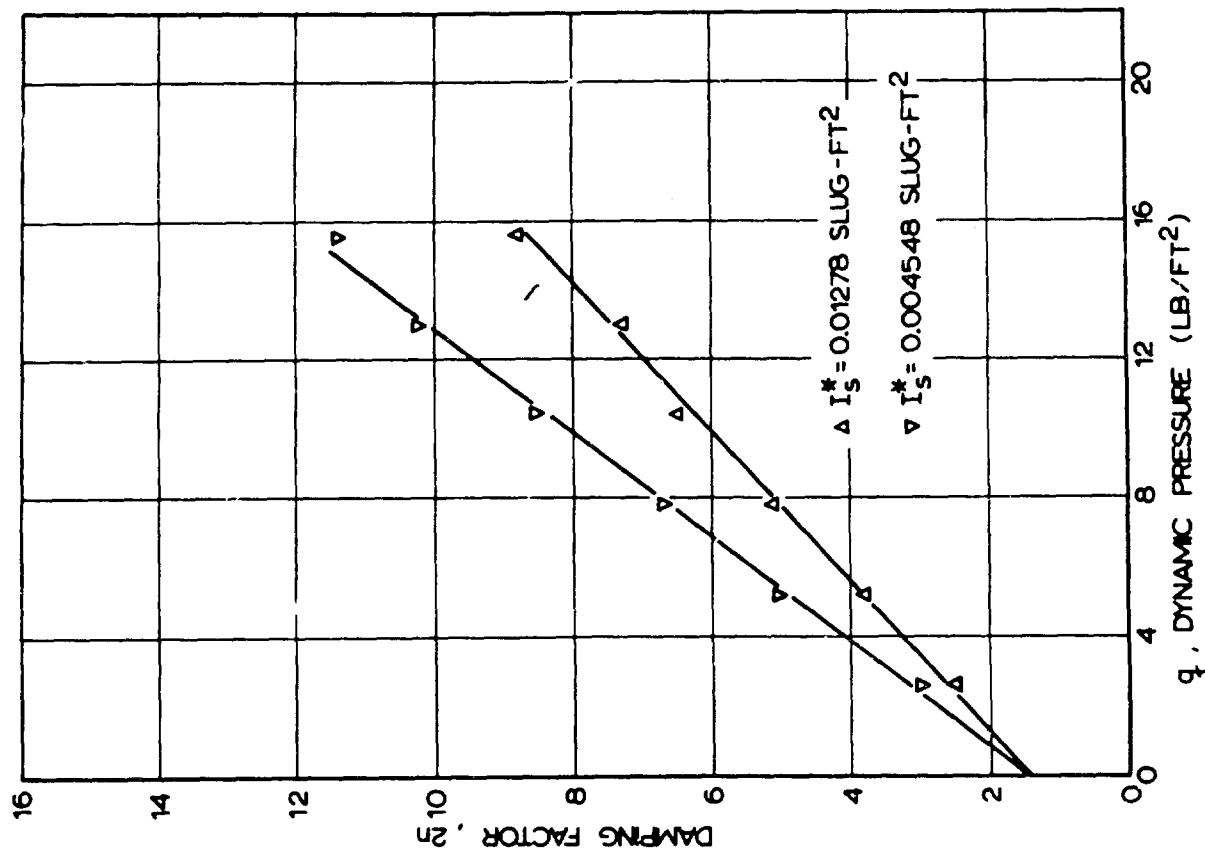


FIG 4-25. EXPERIMENTAL DAMPING FACTOR
VS DYNAMIC PRESSURE

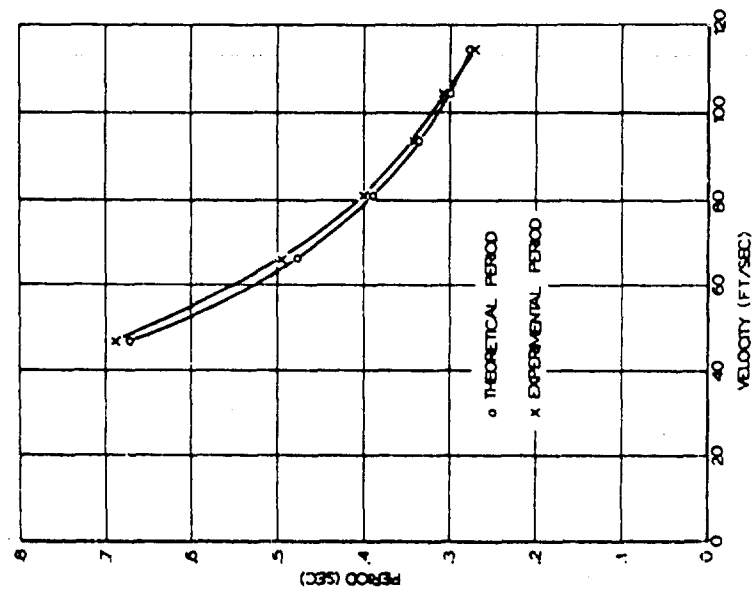


FIG 4-26. PERIOD OF OSCILLATION VS FREE
STREAM VELOCITY
NOMINAL POROSITY 30 FT³/FT²·MIN

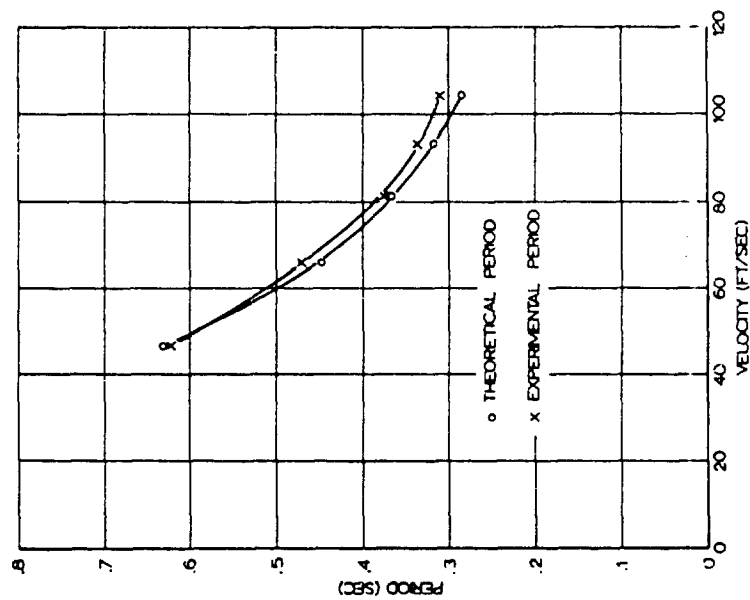


FIG 4-27. PERIOD OF OSCILLATION VS FREE
STREAM VELOCITY
NOMINAL POROSITY 60-90 FT³/FT²·MIN

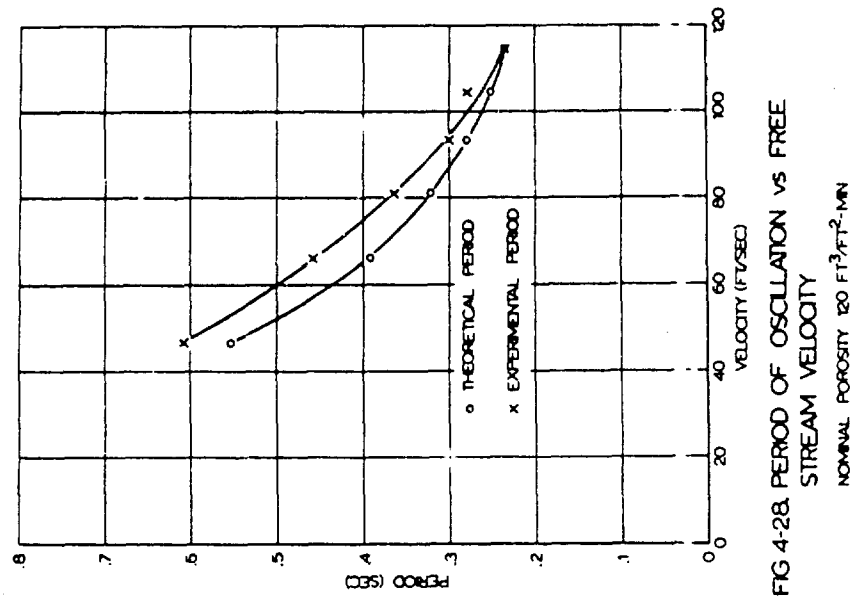


FIG 4-28. PERIOD OF OSCILLATION VS FREE
STREAM VELOCITY
NOMINAL POROSITY 120 FT³/FT²·MIN

Project No 7

4.0 Theoretical Study of Supersonic Parachute Phenomena

4.1 Introduction

This study has been centered around further development of the "spiked" supersonic aerodynamic decelerator conceived and developed through succeeding experimentation and analysis. Work done during the present reporting period will be considered in the following phases:

- 1) Water analogy studies
- 2) Supersonic wind tunnel studies of flexible parachute models.

4.2 Water Analogy Studies

4.2.1 Introduction

The use of the water tow facility in making preliminary studies of the spiked parachute concept has proven to be very fruitful. With the addition of a moving water tow facility a variety of flow field studies can be made. Several of these studies have already been performed, such as the depth field survey and photographic field surveys, as noted in Progress Report No 22, Section 4.2.

4.2.2 Continuation

During the present reporting period efforts have been directed at the determination of the velocity distribution in the flow field of a supersonic parachute.

Since velocity is a vector quantity, one needs to know its magnitude as well as its direction at all points in the flow field. A theoretical analysis of velocity as a function of position for supersonic flow in complex flow fields can only be performed by the method of characteristics, which

is a very involved and tedious task. Furthermore, relatively simple experimental methods for determining the velocity distribution in three dimensional gas flows are non-existent.

However, to determine a velocity flow field by means of water analogy is quite simple and such results could prove to be a valuable tool in mass flow evaluation, design phenomena, and in predicting stability changes at varying Mach numbers.

Preliminary studies of several flow visualization methods in the flow field of a supersonic parachute are being made to determine their practicality, in predicting stability changes at varying Mach numbers. In one method, thin streams of another fluid, such as ink, are injected into the water and their paths observed. If motion pictures are taken, these paths can easily be determined and studied. If "particles" of ink are injected and a reference is made to the time elapsed for the particle to move an increment length, then the velocities of these particles may be established at all points in the flow field. Figure 7-1 is an enlargement of one frame of 16 mm movie film capturing the effect of ink injected into the water.

In a second method, time exposure photographs are taken of confetti particles suspended on the surface of the water in the flow field of the supersonic parachute configuration. As seen from Fig 7-2, these particles appear as thick lines whose lengths are proportional to their velocities.

4.2.3 Proposed Work

Streamlines will be determined experimentally by the above methods and illustrated in graphical form.

Since in reality, certain turbulence and mass exchange between vertical fluid layers exists, the velocity distribution cannot be expected to remain constant for each fluid layer. Therefore, investigations will be made at various

depths to determine the change in the velocity field and the errors it may introduce. Several methods will be applied, such as use of tufts, or streamers, ejection of air bubbles, or suspension of particles within the fluid, to fulfill the above objectives.

To allow for better accuracy in all such tests, the test model size will be increased from a canopy diameter of 8 inches to one of 16 inches.

4.3 Supersonic Wind Tunnel Studies of Flexible Parachute Models

4.3.1 Past Work

During the previous reporting period a variety of outlet shapes for the supersonic parachute were designed as shown in Fig 7-9 of Progress Report No 22, and models with such designs were tested. As seen from Fig 7-12 through 7-16 of the mentioned report, two of these models with perlon screen outlets were quite stable. It was hoped, however, that a solid cloth nozzle outlet design as shown in Fig 7-16 of Progress Report No 22 would be superior to one of screen, in that it would present less of an aerodynamic heating problem.

4.3.2 Continuation

During the present reporting period, wind tunnel tests of flexible spiked supersonic parachutes using the cloth nozzle outlet configuration were conducted at Mach numbers of 1.1, 2.0, and 3.0. The models tested with and without a forebody (Fig 7-4, Progress Report No 21) all had exits shaped like subsonic nozzles as pictured in Fig 7-16 of Progress Report No 22. High speed Schlieren movies, 35 mm flash photos, and drag recordings were made during all wind tunnel tests. In addition, several shadowgraph photographs were taken of stable models at each Mach number.

4.3.3 Test Apparatus

Tests have been conducted in the 12 x 12 inch test section facility described in Progress Report No 22, Section 4.3.3. This particular wind tunnel is of the blowdown type with a high pressure reservoir upstream and a vacuum tank downstream of the test section. Figure 7-3 is a photograph of the test section and the drag recording equipment. The test setup otherwise is similar to that illustrated in Fig 7-6, of Progress Report No 18.

The transonic tests were conducted at the FluidDyne Engineering Corporation's 22 x 22 inch transonic facility. This is a continuous flow wind tunnel with a heated atmospheric intake and a steam ejector low pressure supply downstream of the test section. The test setup which is pictured schematically in Fig 7-4, differs from our conventional test setup in that the model is pulled upstream to deployment, rather than by moving the deployment basket downstream.

4.3.4 Results

Results of the test fall logically under two main headings; the first being ranges of stability, and the second being drag calculations.

With regard to stability, each model was placed into one of three groups by visual inspection of the high speed Schlieren movies. The groups were classified stable, semi-stable, and unstable. Models in the semi-stable group are so defined because they deflate and reinflate by themselves during the run, thus being stable only part of the time.

4.3.4.1 Model Stability

Several models with nozzle exits were tested at Mach 3.0, with and without forebodies, with outlet to inlet diameter ratios (D_o/D_1) ranging from 0.67 to 0.77. Stable configurations were found for all models of that range.

Prints made from Schlieren movies of a run with $D_o/D_1 = 0.72$ are shown in Fig 7-5. A 35 mm flash photo of the same configuration is shown in Fig 7-6 and a shadowgraph photo in Fig 7-7. All models exhibited excellent inflation and a small degree of oscillation. Figure 7-8 shows the stability of various models classified according to their D_o/D_1 values. No distinction was made between tests with and without forebody.

Tests next were conducted at Mach 2.0. From Schlieren photos, however, it was observed that the shock wave emanating from the mounting strut upstream was being reflected from the walls and crossed in front of the cone-cup configuration, thus placing the model in the second test rhombus (see Fig 7-9). Preliminary calculations revealed that the effective Mach number just ahead of the canopy was on the order of 1.5 instead of 2.0. Additional studies are presently being conducted to determine the exact Mach number for these tests. For clarity however, these tests will be referred to a Mach number of 2.0 in the remainder of this report.

Models with the same range of D_o/D_1 as found stable at Mach 3.0 were tested at Mach 2.0, but only a portion of the models in the range (0.71 to 0.73) was found to be stable (see Fig 7-8). Figure 7-9 is a print of a portion of a Schlieren movie taken of a stable model with $D_o/D_1 = 0.72$. Figure 7-10 shows the same model photographed with a 35 mm camera and Fig 7-11 is a shadowgraph photo of the model. From these figures it is again noted that the model possesses excellent inflation and a small degree of oscillation.

Transonic tests were conducted with models whose D_o/D_1 ratio varied from 0.69 to 0.72. Since the test section in the transonic wind tunnel measured 22" x 22", larger models could be tested. To take advantage of the larger test section, several 6 inch (maximum canopy diameter) models were constructed and tested in the transonic Mach number range.

All 6 inch models in the range $0.69 \leq D_o/D_i \leq 0.72$ were found to be stable (see Fig 7-8). Figure 7-12 is a shadowgraph of a model with $D_o/D_i = 0.72$ at Mach 1.10.

4.3.4.2 Conclusions

It can be concluded that the supersonic parachute with an outlet to inlet diameter ratio on the order of 0.72 is stable in the Mach number range 1.1 to 3.0, and that the presence of the forebody has no noticeable effect on the stability of this parachute.

4.3.5 Model Drag Characteristics

Drag measurements were made on all models tested during this reporting period. The drag force was detected with the strain gage assembly shown in Fig 7-16 of Progress Report No 22, and recorded by means of a Honeywell Visicorder (Model 501). Values of drag coefficients based on the projected area are presented in Fig 7-13.

It can be seen from the figure that the drag coefficients exhibit a characteristic dependence on the Mach number; that is, the drag coefficient is maximum in the region around Mach 1.0, falls to a low at about Mach 1.5, and gradually rises again with increasing Mach number.

It can also be seen from Fig 7-13 that the presence of the forebody has a decreasing effect on the magnitude of the drag coefficient. For lower Mach numbers, however, the effect of the forebody seems to be less pronounced.

4.4 Proposed Work

As previously mentioned, during the Mach 2.0 tests the reflected shock wave from the model mounting strut reduced the Mach number in the test rhombus to about 1.5. Presently an investigation is under way to determine the exact Mach number

in this region and the results of this investigation will be presented in the next reporting period.

A technical report describing the work conducted thus far in the development of the spiked supersonic decelerator will be prepared during the next reporting period.



FIG 7-1. ILLUSTRATION OF FLOW VISUALIZATION IN THE WATER FLOW CHANNEL BY INJECTION OF INK INTO THE FLOW FIELD OF A SUPERSONIC PARACHUTE

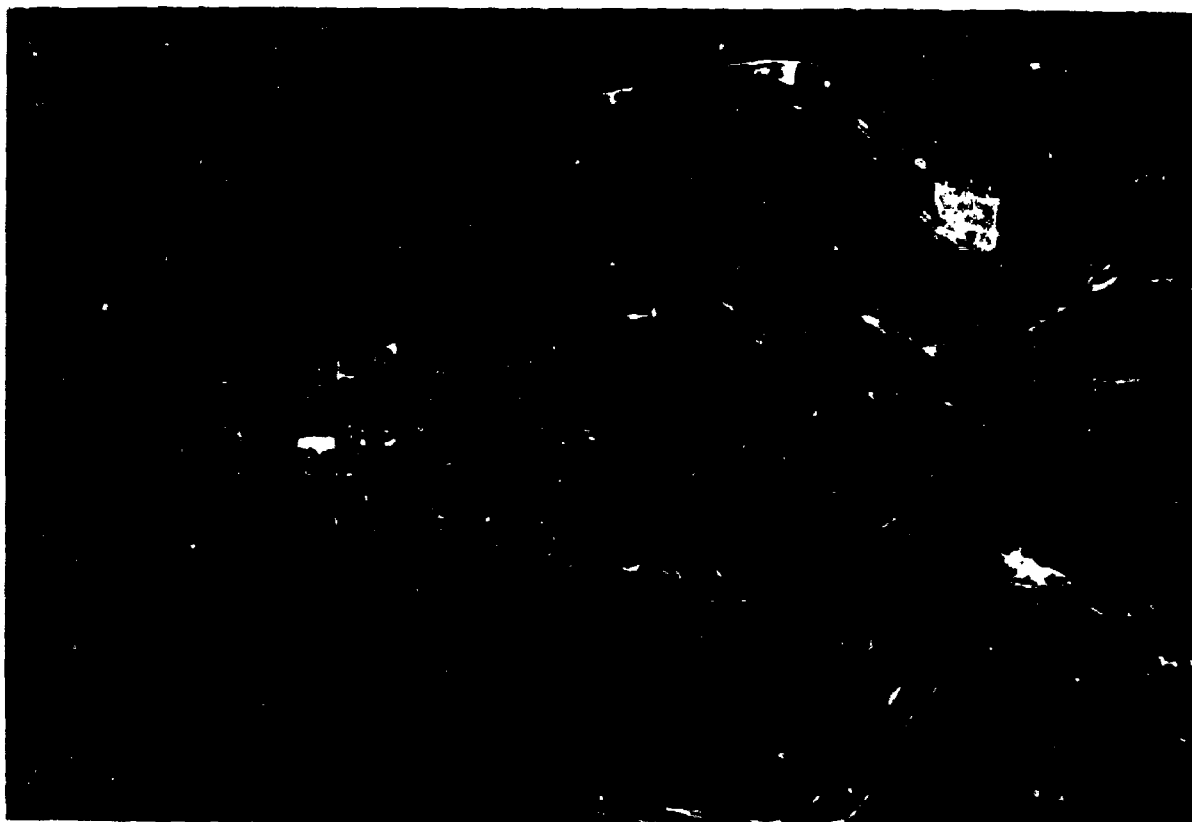


FIG 7-2. TIME EXPOSURE PHOTOGRAPH OF CONFETTI PARTICLES SUSPENDED IN THE FLOW FIELD OF A SUPERSONIC PARACHUTE CONFIGURATION AT SIMULATED MACH NUMBER 2.

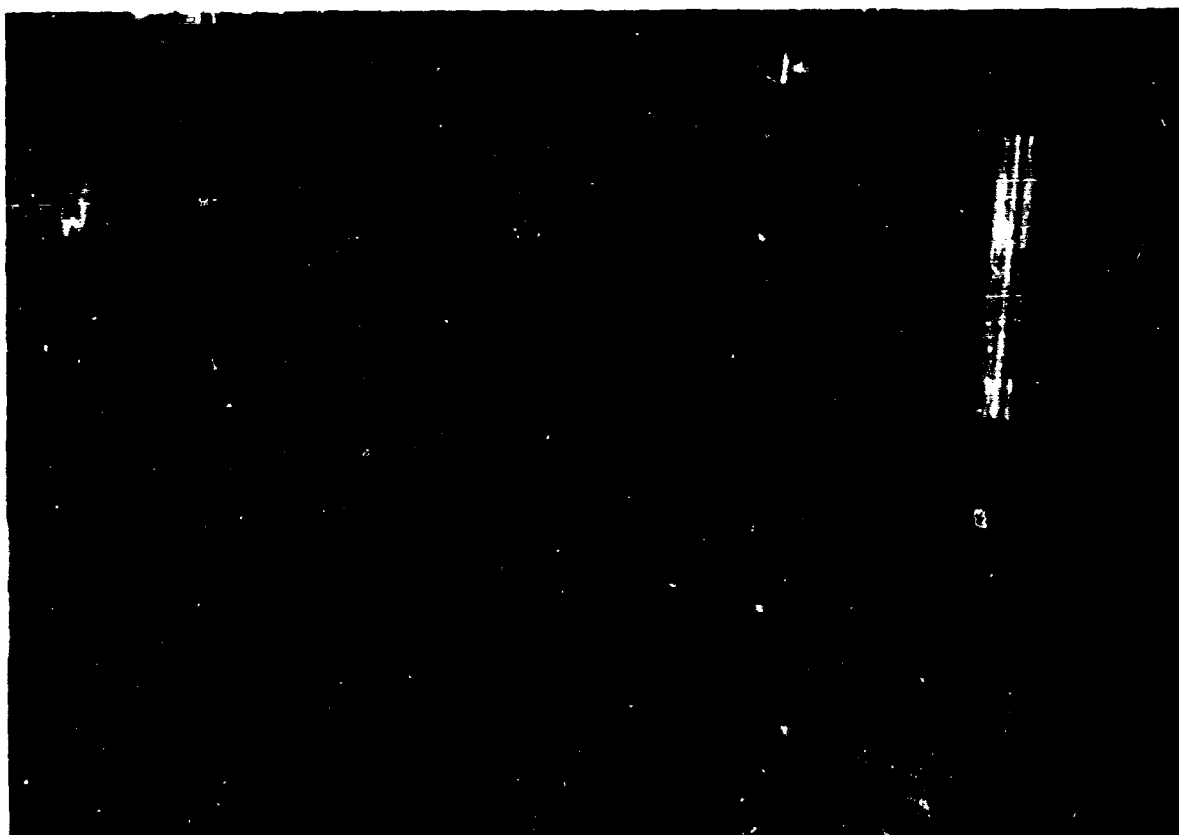


FIG 7-3. PHOTOGRAPH OF TEST SECTION OF THE MACH 2.0 FACILITY AND DRAG SENSING AND RECORDING EQUIPMENT

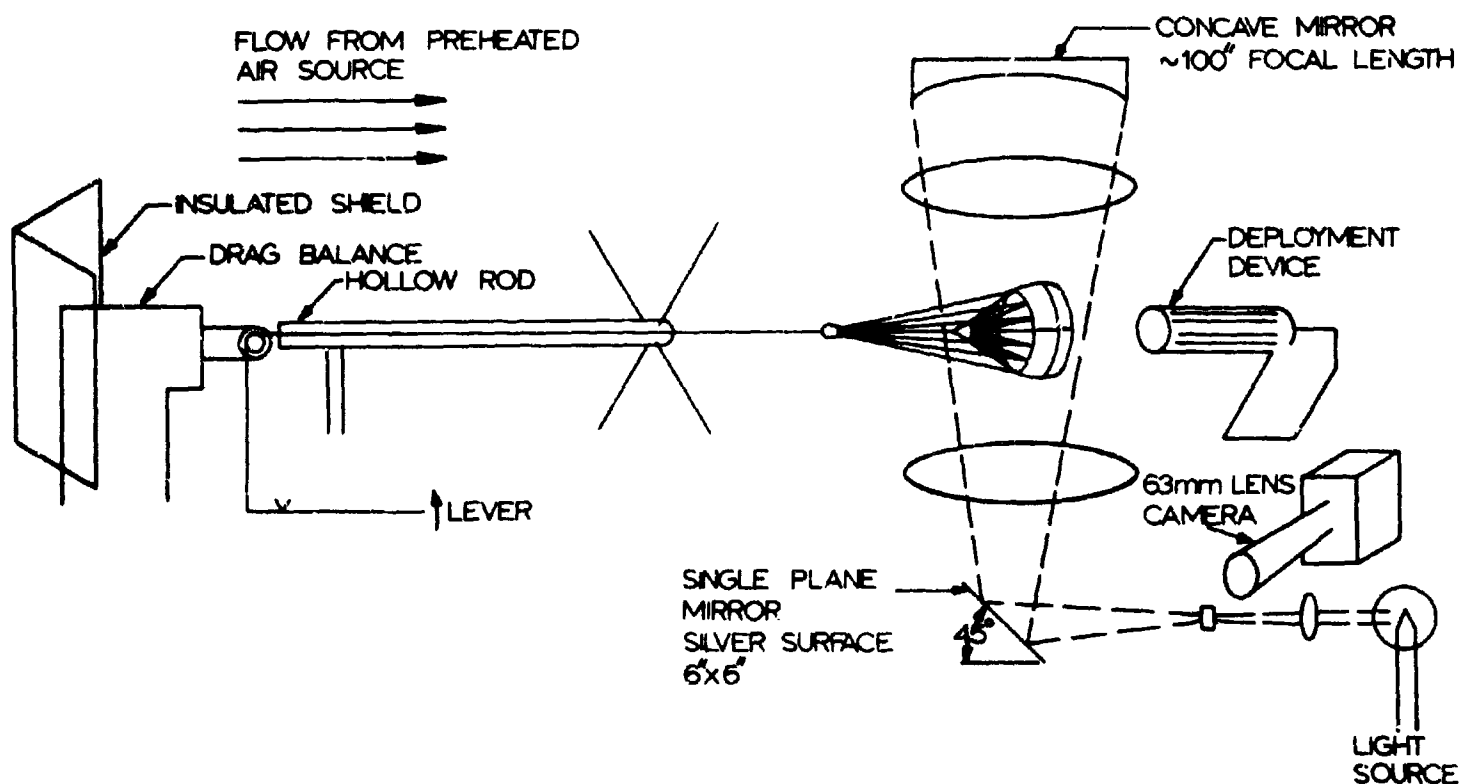


FIG 7-4. SCHEMATIC DRAWING OF FLUDYNE 23'x23' TRANSONIC TEST FACILITY

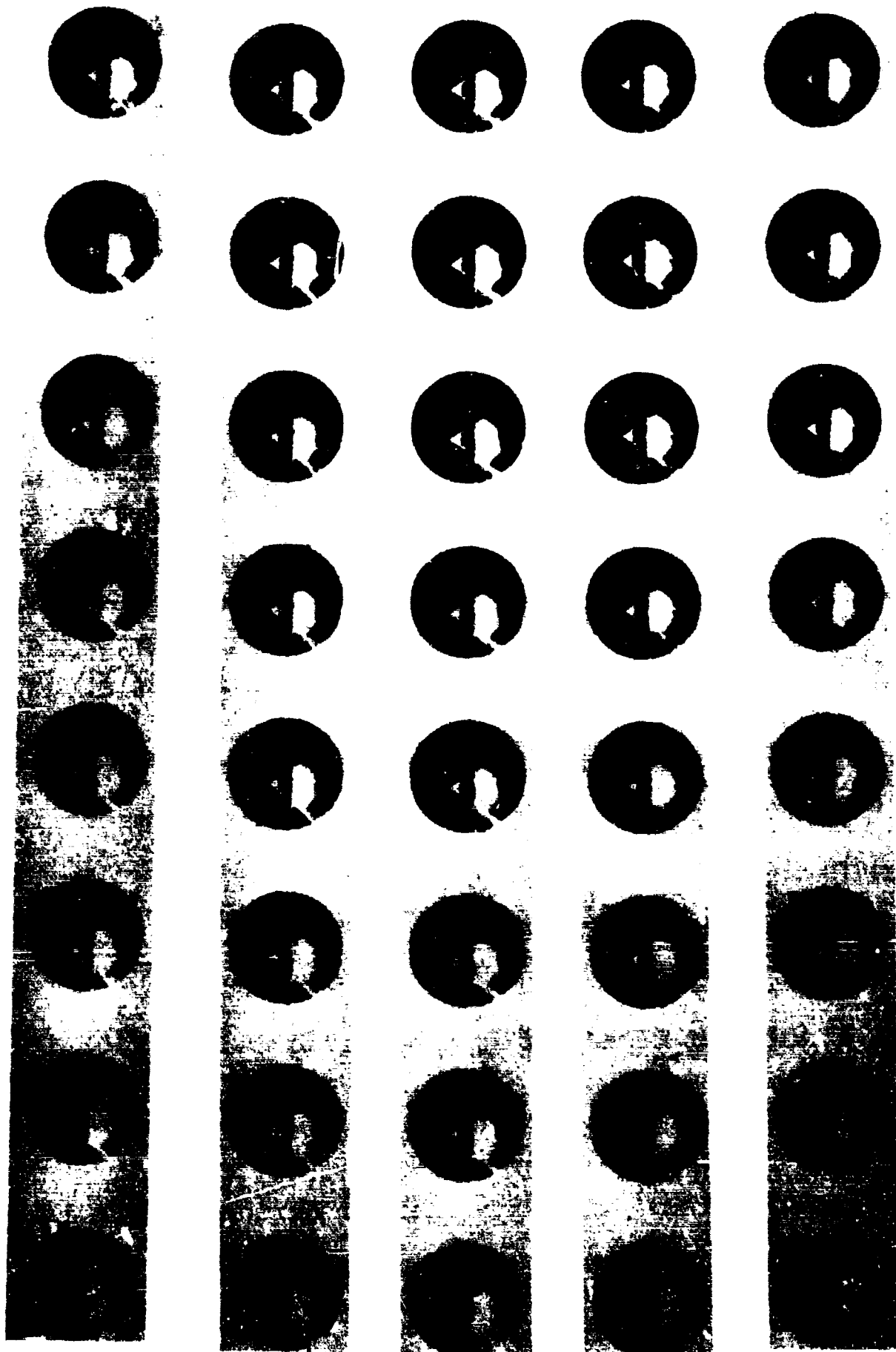


FIG 7-5. SCHLIEREN PHOTOGRAPH SEQUENCE SHOWING STABLE SUPER-SONIC PARACHUTE CONFIGURATION IN WAKE OF OGIVE FORE-BODY ($L/D = 8$) AT MACH 3.0 (2000 FRAMES PER SEC)
 $(D_1 = 3.57"$, $H/D_1 = 0.6$, $D_o/D_1 = 0.72$,
 $\Theta = 34^\circ$, $1/D_1 = 0.35)$.

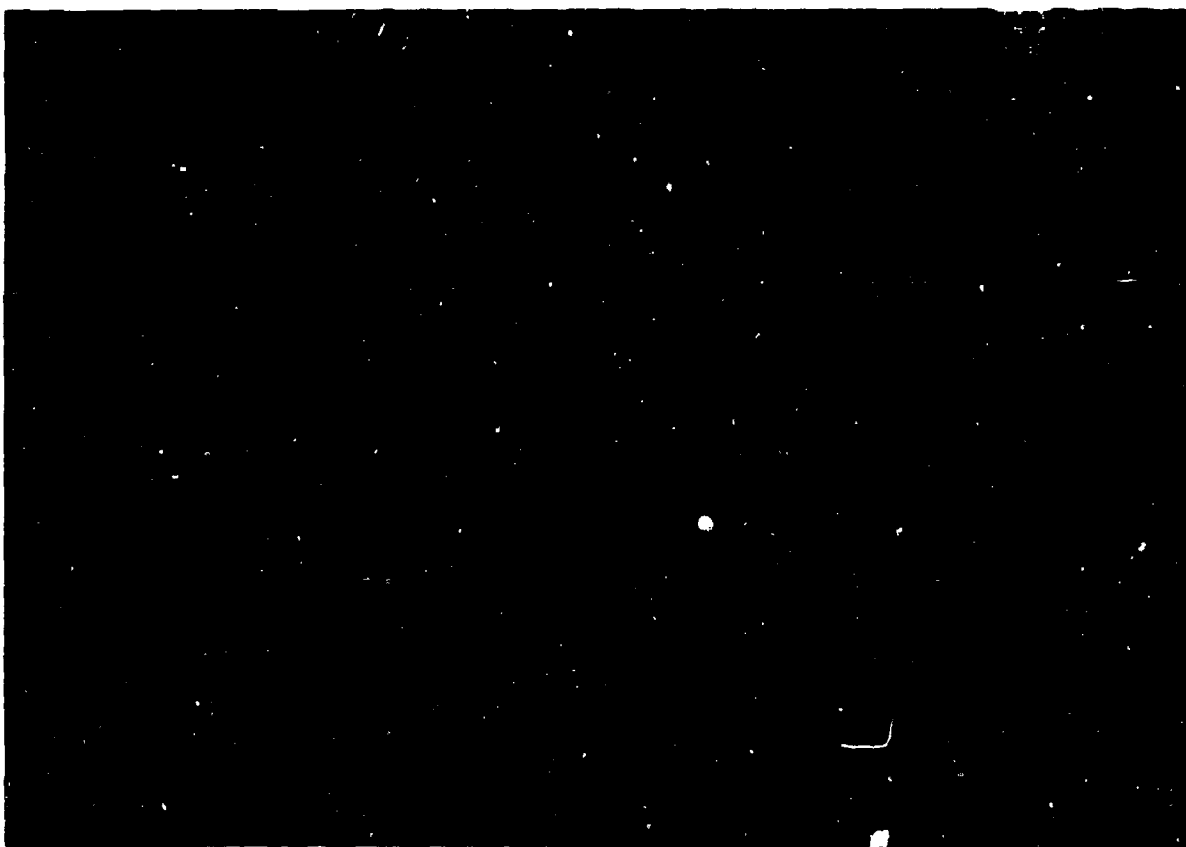


FIG 7-6. FLASH PHOTOGRAPH OF A STABLE SUPERSONIC PARACHUTE CONFIGURATION BEHIND OGIVE FOREBODY AT MACH 3.0 ($D_1 = 3.56$, $H/D_1 = 0.60$, $D_0/D_1 = 0.72$, $\theta = 34^\circ$, $1/D_1^2 = 0.35$).

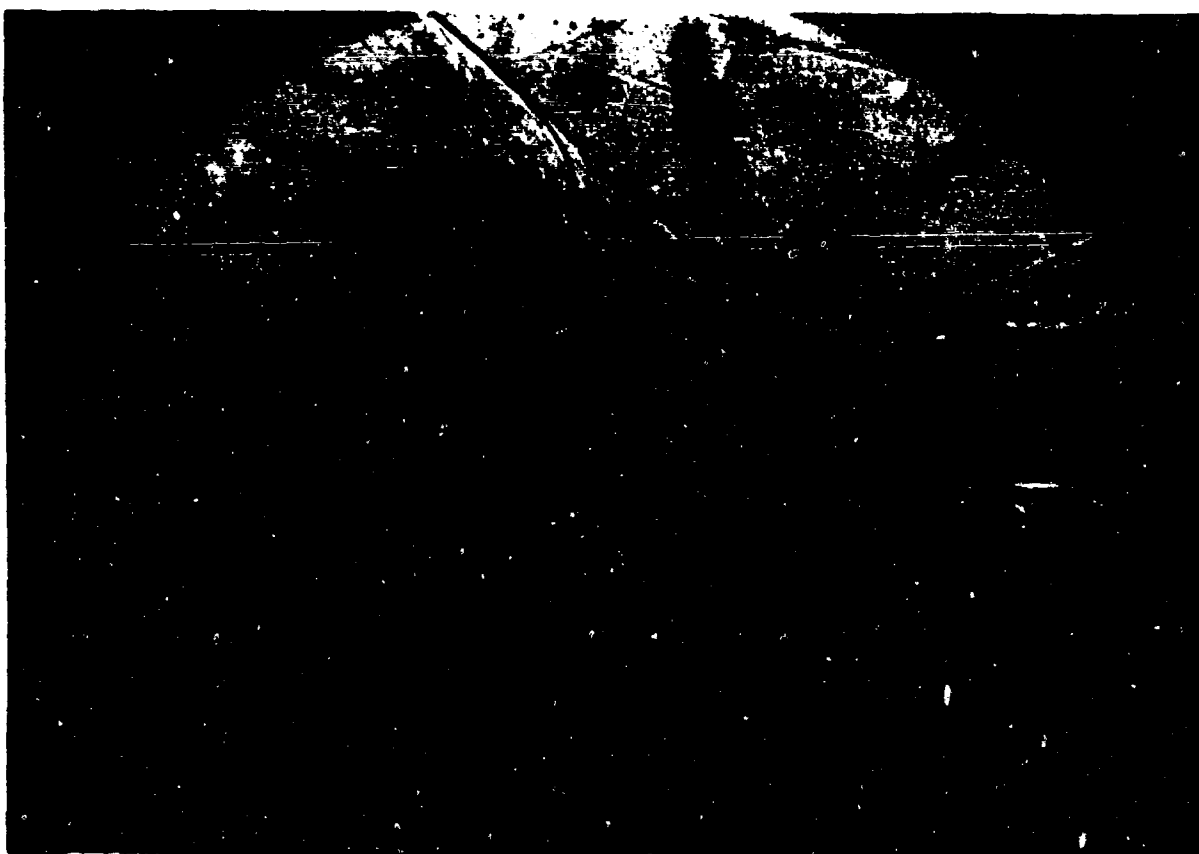


FIG 7-7. SHADOWGRAPH PHOTOGRAPH OF A STABLE SUPERSONIC PARACHUTE CONFIGURATION IN WAKE OF OGIVE FOREBODY ($L/D = 8$) AT MACH 3.0 ($D_1 = 3.56$, $H/D_1 = 0.60$, $D_0/D_1 = 0.72$, $\theta = 34^\circ$, $1/D_1^2 = 0.35$).

MACH 3.0	D_o/D_i	STABLE	SEMI-STABLE	UNSTABLE
	0.68	(1)*	(1)	
	0.71	(2)		
	0.72	(7)		
	0.73	(2)		
	0.77	(2)		
MACH 2.0	D_o/D_i	STABLE	SEMI-STABLE	UNSTABLE
	0.67		(2)	
	0.69			(1)
	0.71	(3)		
	0.72	(6)	(1)	
	0.73		(1)	
	0.74			(1)
	0.77			(1)
MACH 1.0	D_o/D_i	STABLE	SEMI-STABLE	UNSTABLE
	0.685	(2)		
	0.70	(2)		
	0.72	(1)	(1)	

*Numbers in parenthesis signify the number of tests.

FIG 7-8. DEGREE OF STABILITY OF MODELS TESTED AT VARIOUS MACH NUMBERS

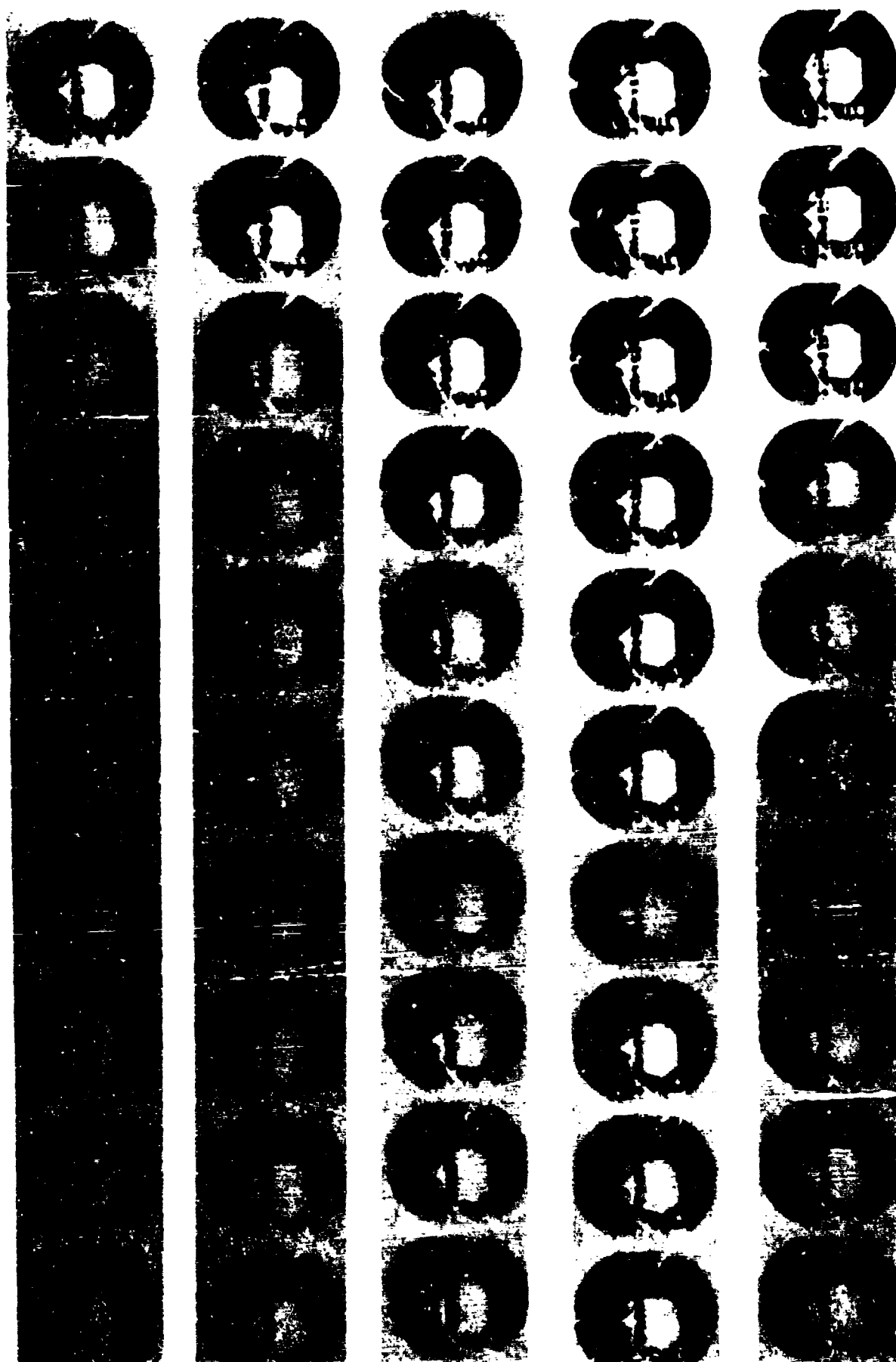


FIG 7-9. SCHLIEREN PHOTOGRAPH SEQUENCE OF STABLE SUPER-
SONIC PARACHUTE CONFIGURATION IN FREESTREAM AT
MACH 2.0. (2000 FRAMES PER SEC). ($D_1 = 3.57''$,
 $H/D_1 = 0.60$, $D_0/D_1 = 0.72$, $\theta = 34^\circ$, $1/D_1 = 0.35$).



FIG 7-10. FLASH PHOTOGRAPH OF A STABLE SUPERSONIC PARACHUTE CONFIGURATION IN FREE STREAM AT MACH 2.0
 $(D_1 = 3.57", H/D_1 = 0.60, D_o/D_1 = 0.72,$
 $\theta = 34^\circ, 1/D_1 = 0.35).$



FIG 7-11. SHADOWGRAPH PHOTOGRAPH OF STABLE SUPERSONIC PARACHUTE CONFIGURATION IN FREE STREAM AT MACH 2.0. $(D_1 = 3.57", H/D_1 = 0.60, D_o/D_1 = 0.72,$
 $\bullet = 34^\circ, 1/D_1 = 0.35).$

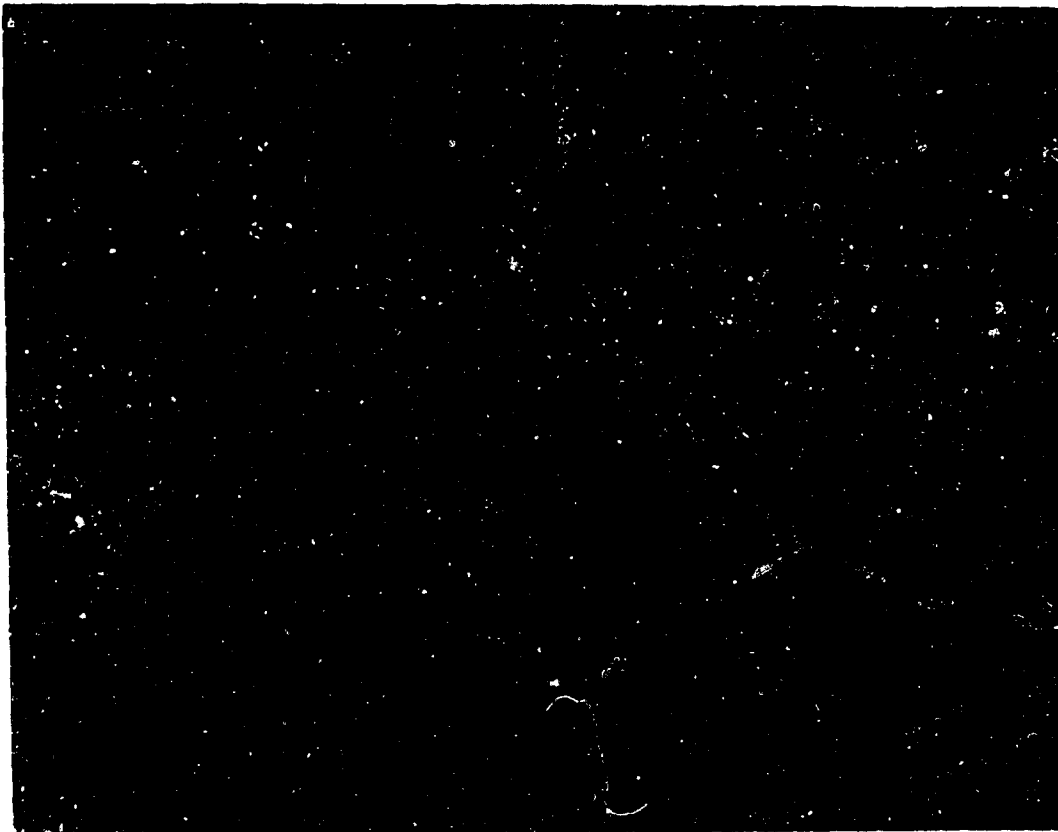


FIG 7-12. SHADOWGRAPH PHOTOGRAPH OF A STABLE SUPERSONIC PARACHUTE CONFIGURATION IN FREE STREAM AT MACH 1.10 ($D_1 = 5.73'$, $H/D_1 = 0.60$, $D_0/D_1 = 0.72$, $\theta_1 = 34^\circ$, $1/D_1 = 0.35$).

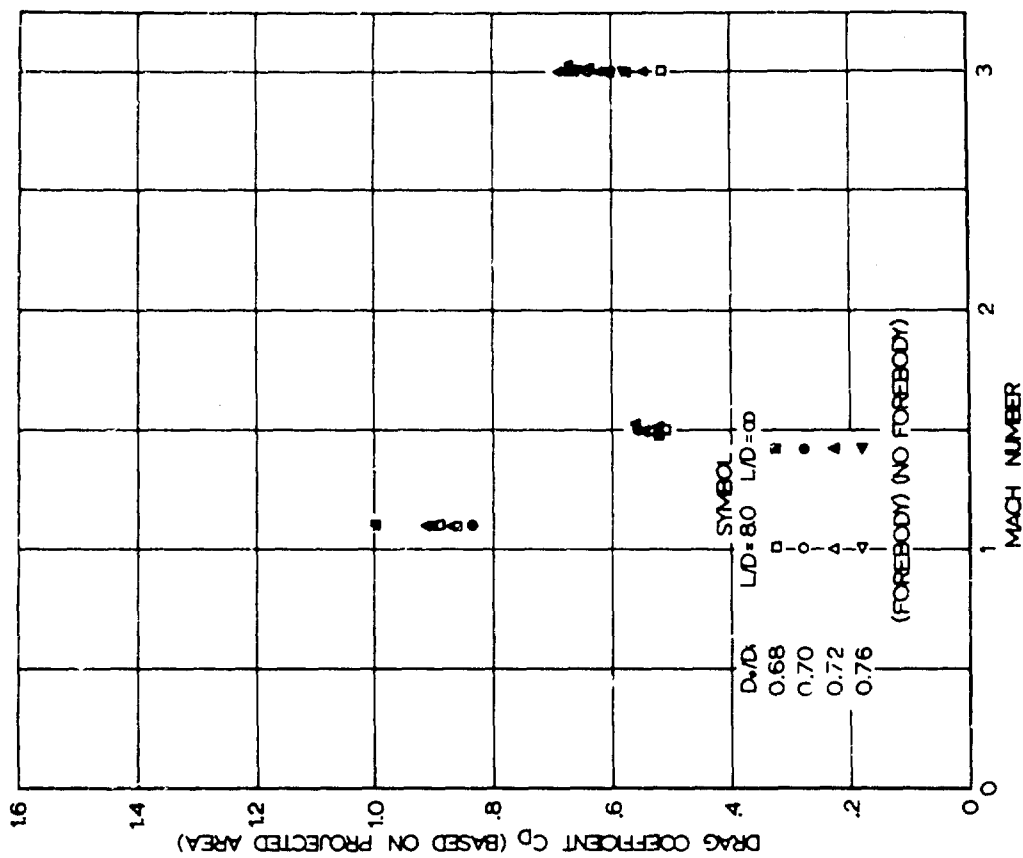


FIG 7-13. DRAG COEFFICIENT VS MACH NUMBER FOR SUPERSONIC PARACHUTE MODELS WITH VARYING D_0/D_1 RATIOS

Project No 8

5.0 Theoretical Analysis of the Dynamics of the Opening Parachute

This project will be reported as the two supporting investigations:

- a) Experimental analysis of the dynamics of the opening parachute.
- b) Mass flow study of the opening parachute.

5.1 Experimental Analysis of the Dynamics of the Opening Parachute

5.1.1 Introduction

Progress Report No 18 presented preliminary results of the parachute opening force measurements from wind tunnel tests using a three foot nominal diameter solid flat parachute. The opening force and projected area as functions of time were determined with a canopy loading, $W/C_D S_0$, of 0.323 psf and a free stream dynamic pressure of one inch of water. During the present reporting period these results were further analyzed with the results of that analysis presented in the following paragraphs.

5.1.2 Continuation

Figure 8-1 shows the force-time history for a typical experimental test. From this particular data it can be seen that the maximum force occurs at a time of $0.74 t_f$, where t_f is the filling time of the canopy. The magnitude of this force is on the order of 35 lbs. A summary of experimental results, including filling time, opening shock force, and maximum projected area appear in Table 8-1.

In addition to projected area-time and force-time histories, the distance of travel of parachute system (canopy and suspended mass) was recorded as a function of time. Using an instantaneous slope method, the absolute velocity of the system, V , with respect to the wind tunnel was determined. From this, the relative velocity V_R of the parachute system relative to the free stream velocity, V_o , was found from the relationship:

$$V_R = V_o - V \quad . \quad (8.1)$$

This relationship is shown as a function of time in Fig 8-2. From the dynamic equations of the parachute system, we know the opening shock can be found from:

$$F_{max} = -a_{max} m_s , \quad (8.2)$$

where a_{max} is the acceleration at the point of maximum force and is obtained from the slope of the velocity curve and m_s is the suspended mass.

By comparing Figs 8-1 and 8-2, we see that the maximum slope does occur at the point of opening shock; namely, $t_o/t_f = 0.74$. By using the slope at this point we find the $a_{max} = -577.2 \text{ ft/sec}^2$. Substituting this into Eqn 8.2 we obtain 30.7 lbs as an estimate of the opening shock. This result compares within 11 percent of the actual recorded value.

Figure 8-3 shows the projected area as a function of time for a typical case. The experimental curve and the parabolic assumption are graphed together for comparison. Since in reality there is an initial projected area, S_i , the equation of the parabola is given by:

$$S = \left(\frac{S_{max} - S_i}{t_f^2} \right) t^2 + S_i \quad ,$$

or

$$\frac{S}{S_o} = \left[\frac{S_{max} - S_i}{S_o} \right] \left[\frac{t}{t_f} \right]^2 + \left[\frac{S_i}{S_o} \right] \quad (8.3)$$

From this figure it is apparent that the parabola follows the experimental curve fairly close, up until the time of the opening shock, where the greatest deviation occurs. Since, physically, the slope of this curve at $t/t_f = 1$ must be zero, such a deviation is to be expected. However, as a simplification of the analytical problem, the parabolic assumption appears justified. This is in reference to Progress Report No 16, paragraph 6.2.3.3., where it was assumed that

$$S = \frac{D_o^2}{\pi} T^2, \quad (8.4)$$

where S is the projected area of the canopy during inflation, D_o is the nominal diameter of the canopy, and T is the ratio of instantaneous time to filling time.

5.1.3 Proposed Work

In the future, it is planned to repeat these test series for various values of canopy loading, $W/(C_D S_o)$, and observe the effect on opening time and opening force.

5.2 Mass Flow Study of the Opening Parachute

5.2.1 Introduction

The mass flow characteristics are very important in the derivation of a theory for predicting the filling time and opening shock of reefed parachute canopies. Therefore, tests are presently being conducted in the University of Minnesota subsonic wind tunnel on the mass flow through the canopy mouth and vent hole during various stages of inflation.

Progress Report No 22 presented in detail the experimental program being conducted. During this reporting period, it was found necessary to make certain modifications in the models and instrumentation.

5.1.2 Continuation

The solid flat parachute models representing various stages of canopy inflation have been constructed as described in Progress Report No 22. These models have been modified slightly in that the brass mounting rings in the canopy mouth and vent hole have been removed to prevent flow interference. These rings are not necessary to this study since each model is suspended in the wind tunnel by the four equally spaced wires at the canopy mouth and vent hole.

The experimental set-up is described in detail in Progress Report No 22. Some modifications in this set-up have been made. In particular, three new pressure survey rakes varying in size so as to fit the different models are now being constructed. These rakes will be used to determine the pressure distribution and corresponding velocity distribution for the canopy mouth for various stages of the inflation process. The rakes will replace the pitot static tube and traversing mechanism used previously, and which were found to be unsatisfactory for accurate measurements. With the previous arrangement, the static holes of the pitot static tube were in the plane of the canopy mouth while the total pressure opening was in front of the canopy mouth plane, thus giving non-uniform results. The new rakes have alternating static and total pressure probes so that both these pressures can be measured in the plane of the canopy mouth. The rake enters the canopy through a small opening in the canopy side and is connected to a multiple manometer for data recording.

5.2.3 Proposed Work

The construction of the three pressure survey rakes for the canopy mouth will be completed. It is anticipated that tests will then proceed on the two sets of models with the improved method of inflow velocity measurement for the canopy mouth. It is hoped that these mass flow tests will give a clear relationship between the inflow velocity through the canopy mouth and the velocity through the vent hole during the parachute opening process.

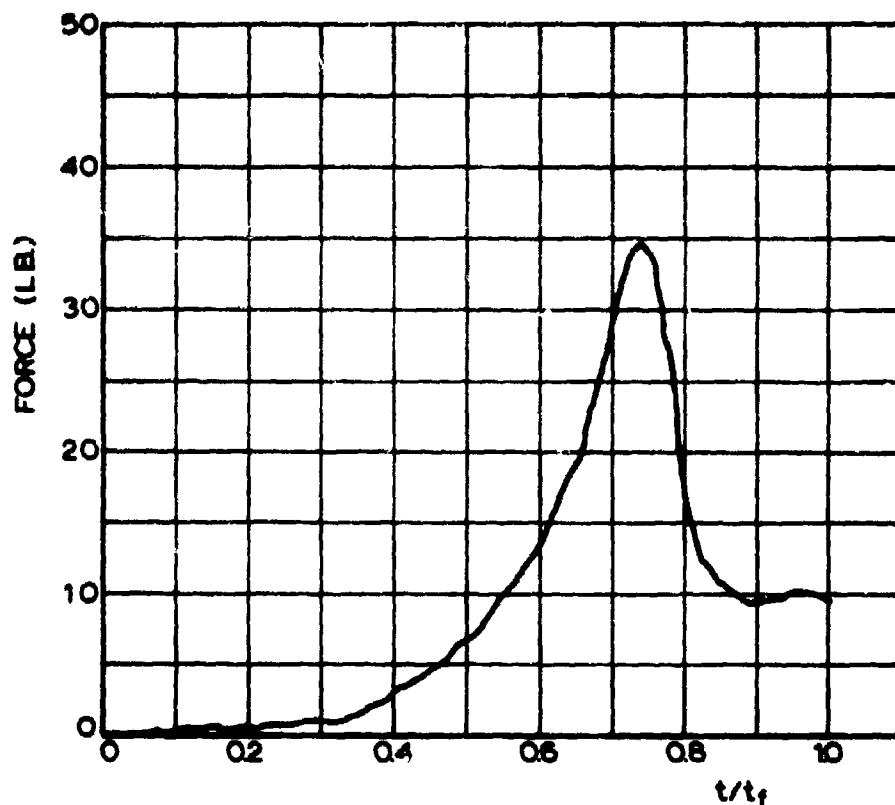


FIG 8-1. FORCE VERSUS TIME RATIO
 $W/C_D S_o = 0.323$ psf

RUN NO.	TIME OF OPENING SHOCK (t_o) (SEC)	OPENING SHOCK (F_o) (LB)	FILLING TIME (t_f) (SEC)	MAXIMUM PROJECTED AREA (IN ²)	t_o/t_f
1	0.195	37.05	0.265	3.87	0.736
2	0.203	33.79	0.267	3.78	0.760
3	0.186	34.58	0.255	3.41	0.729
4	0.201	35.07	0.276	3.68	0.728
5	0.181	34.58	0.245	3.40	0.739
6	0.160	35.41	0.231	3.45	0.693
7	0.180	35.48	0.240	3.71	0.750
8	0.160	38.73	0.225	3.43	0.711
9	0.160	38.93	0.232	3.65	0.690

TABLE 8-1. EXPERIMENTAL RESULTS FOR 3.0 FT. NOMINAL DIAMETER SOLID FLAT PARACHUTE UNDER FINITE MASS CONSIDERATIONS $W/(C_D S_o) = 0.323$ psf

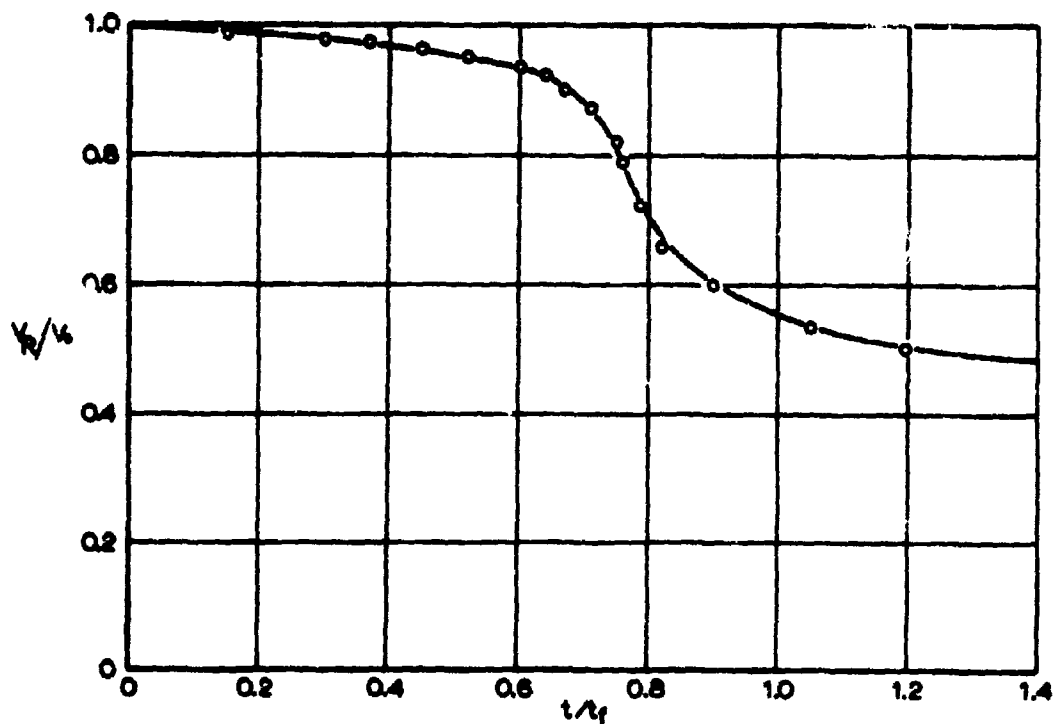


FIG 8-2. RELATIVE VELOCITY OF PARACHUTE SYSTEM VERSUS TIME RATIO $W/(C_D S_a) = 0.323 \text{ psf}$

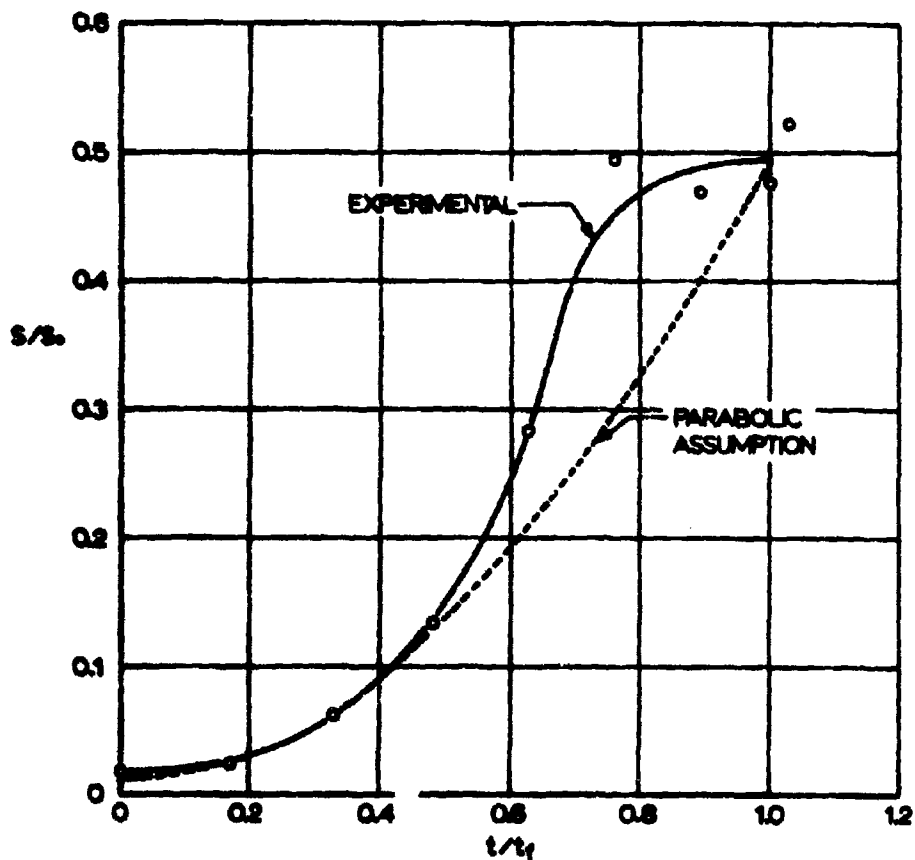


FIG 8-3. PROJECTED AREA RATIO VERSUS TIME RATIO $W/(C_D S_a) = 0.323 \text{ psf}$

Project No 9

6.0 Statistical Analysis of Extraction Time, Deployment Time, Opening Time, and Drag Coefficient for Aerial Delivery Parachutes and Systems

The final draft of the technical report for this project has been approved by the Procuring Agency and has been assigned the following technical report number and title: ASD Technical Documentary Report 62-638, "Analysis of Parachute Deployment of Heavy Cargo," by Helmut G. Heinrich, Ivan R. Russell, and Donald J. Eckstrom.

The photo-offset copy of this report has been submitted to the Procuring Agency for printing. This marks the completion of efforts on this project.

7.0 Gliding Aerodynamic Decelerator

7.1 Introduction

The objective of this study is to develop a self-inflating aerodynamic decelerator with a lift to drag ratio L/D of two. With such a lift to drag ratio, a parachute would glide at an angle of 26.5° with the horizon corresponding to an angle of attack of 63.5° . The forces and coordinates associated with a gliding parachute are shown in Fig 12-1 while the stability notation adopted is shown in Fig 12-2.

7.2 Continuation

During the present reporting period, further experiments were performed on the aerodynamic decelerator described in Progress Report No 22 and shown in Fig 12-3. This configuration displayed an angle of attack of 48° corresponding to an L/D of 1.10. Its longitudinal stability (pitch) was $\pm 5^\circ$ and its lateral stability (roll) was $\pm 10^\circ$. Several models of this design have been constructed and all exhibited similar characteristics.

To confirm wind tunnel studies of the 24" nominal diameter model, a larger model suitable for drop testing was constructed. This model was 10 feet in diameter and constructed of nylon cloth with a nominal porosity of $10 \text{ ft}^3/\text{ft}^2\text{-min}$. It is shown in Fig 12-4.

Drop tests were conducted to determine the approximate angle of attack and the stability of this larger model. The drop tests were conducted at a descent rate of approximately 10 ft/sec. The parachute assumed a very stable gliding attitude in a relatively short time and achieved a maximum stable angle of attack of approximately 50° , corresponding to an L/D of 1.19. This model was observed to be quite stable with a

longitudinal stability (pitch) of $\pm 5^\circ$ and a lateral stability (roll) of $\pm 10^\circ$.

To establish more accurately the stability of this configuration, three component (normal, tangential, and moment forces) studies were performed on a 16" diameter model in the closed test section of the University of Minnesota subsonic wind tunnel.

The model used in these tests was designed with the suspension lines extending over the canopy. This method of attaching the suspension lines distributes the stress more evenly over the canopy. Figure 12-5 shows the inflated test model. Testing of this model has been completed and the test data presently being reduced will be available in the next reporting period.

7.3 Discussion

During this reporting period efforts were directed toward obtaining further data on various models based on the conceived decelerator described in Progress Report No 22. Initial experiments with the 10 foot diameter prototype have yielded promising results. The results from these tests have confirmed the results of open test section wind tunnel experiments with the smaller models. That is, this configuration attains a stable angle of attack of approximately 50° corresponding to an L/D of 1.19.

7.4 Proposed Work

During the next reporting period data obtained from the three component measurements, the open test section wind tunnel tests, and drop tests will be thoroughly analyzed. In addition, new configurations for a gliding decelerator with a higher L/D ratio will be investigated.

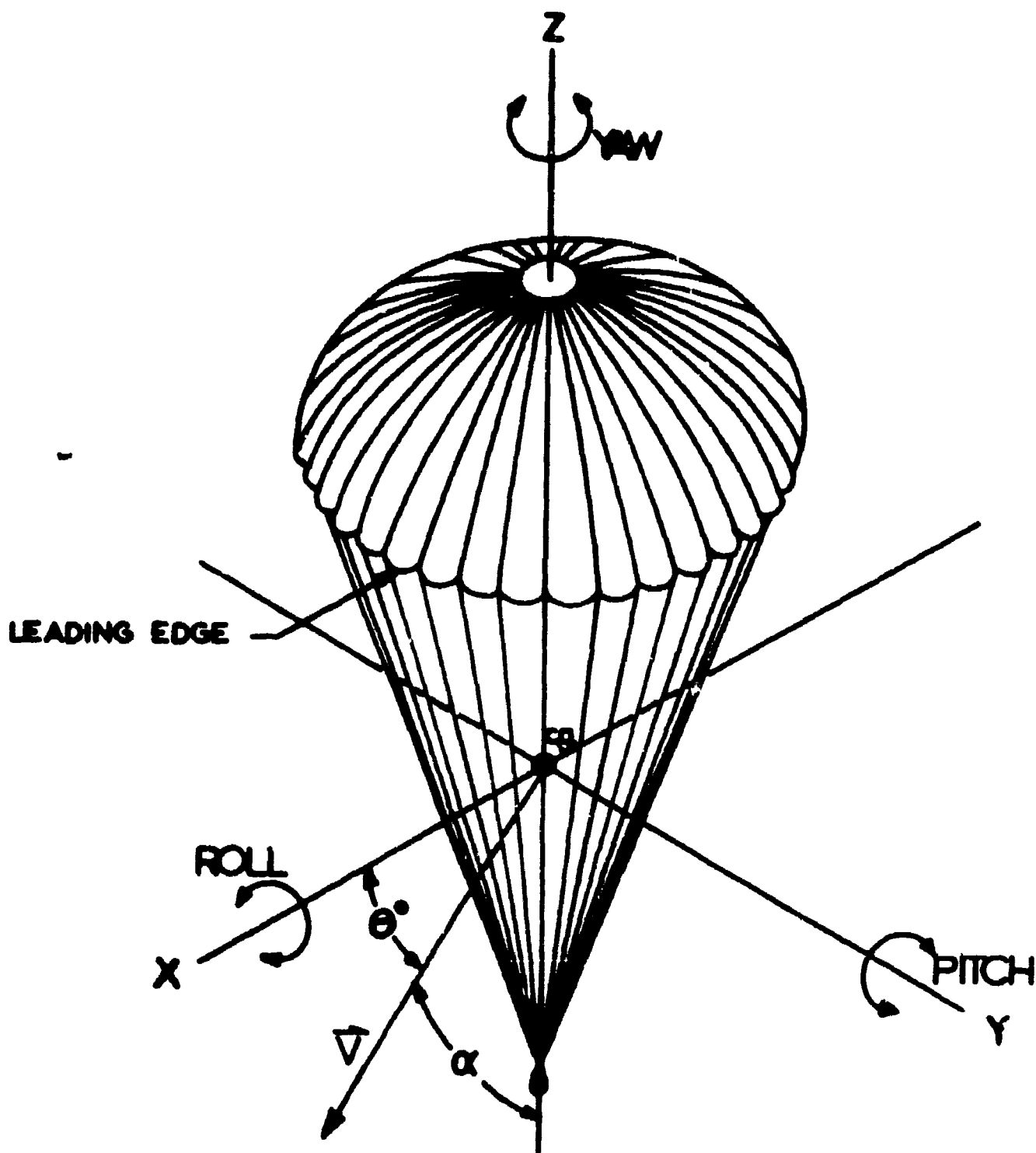


FIG 12-2. STABILITY NOTATION FOR GLIDING PARACHUTE

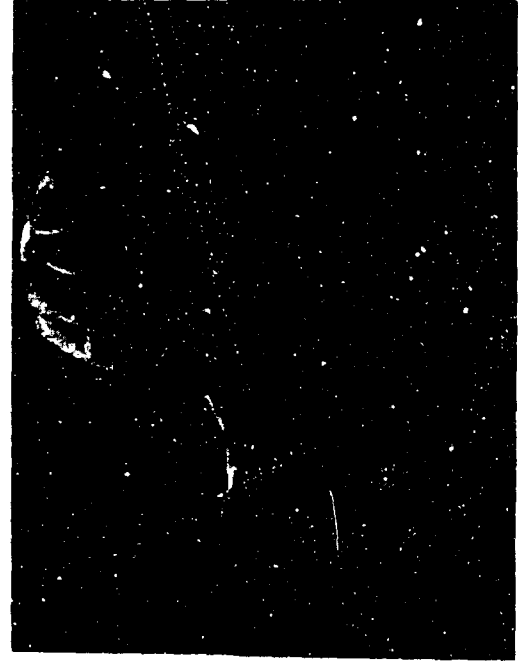


FIG 12-4. 10 FOOT DIAMETER PROTOTYPE OF THE
PROPOSED GLIDING DECELERATOR



FIG 12-3. PROPOSED GLIDING DECELERATOR
IN WIND TUNNEL

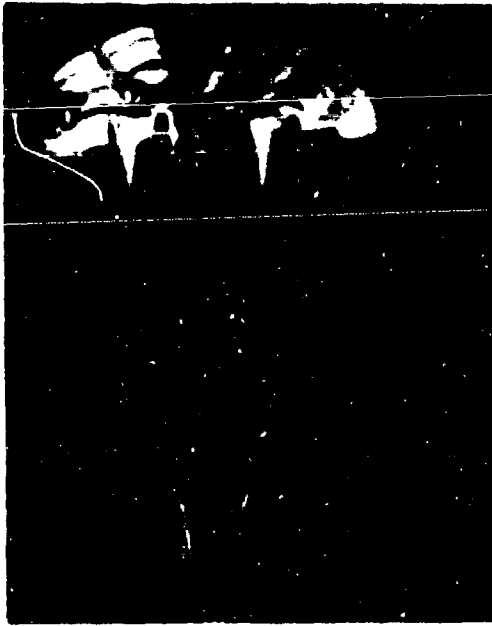


FIG 12-5. 16 INCH DIAMETER MODEL OF THE PROPOSED GLIDING DECELERATOR DURING
THREE COMPONENT STUDIES

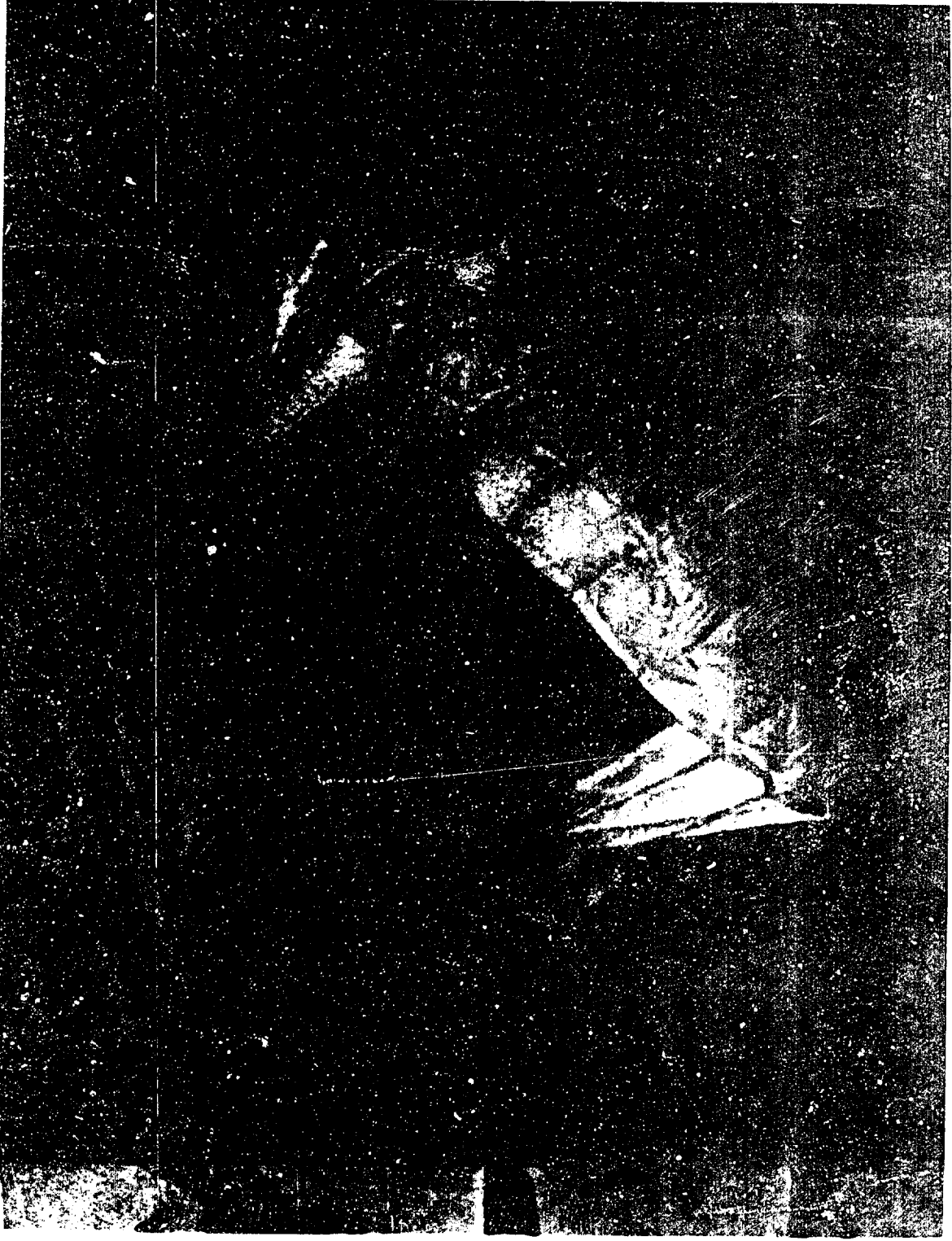


FIG 12-6. CONFIGURATION OF GLIDING DECELERATOR WITH
31 SUSPENSION LINES

Project No 13

8.0 Effective Porosity Studies

8.1 Parachute Cloths

Progress Report No 20, Section 9.1, presented test data for the effective porosity, C , of four samples of parachute cloth as a function of the pressure ratio $\Delta p / \Delta p_{cr}$ with the density ratio σ as a parameter. The pressure ratio range covered in that series of tests was $0.04 \leq \Delta p / \Delta p_{cr} \leq 1.0$ for $\sigma = 1.0$ and $0.4 \leq \Delta p / \Delta p_{cr} \leq 2.5$ for $\sigma = 0.1$.

In order that a much wider range of pressure ratios could be used, new test apparatus has been installed. The apparatus consists of three high accuracy, long scale flow meters, capable of accurately gaging flow rates as low as $0.07 \text{ ft}^3/\text{min}$. With this new equipment, it will be possible to extend our pressure ratio range to include $0.00137 \leq \Delta p / \Delta p_{cr} \leq 0.03$ for $\sigma = 1.0$ and $0.0137 \leq \Delta p / \Delta p_{cr} \leq 0.3$ for $\sigma = 0.1$. Tests are presently being conducted on the four previously tested cloth samples over the extended test range. The results of these tests will be presented during the next reporting period.

8.2 Ribbon Grid Configurations

Progress Reports Nos 20, 21, and 22 presented results from tests on various ribbon grid configurations. No new results are available for the current reporting period.

Project No 14

9.0 Study of Flow Patterns of Aerodynamic Decelerators by Means of the Surface Wave Analogy

9.1 Introduction

Progress Report No 22 noted continued refinement and development of the moving water flow channel including a modified light source for the Schlieren system, improved photographic techniques, and the construction of an observation platform.

9.2 Present Work

Theoretical considerations of the hydraulic analogy supported by water depth measurements on different scale models of a 20 degree half angle wedge indicate the desirability of using relatively larger models than those tested so far. These were limited to a characteristic dimension, such as length or diameter, of 5 to 10 inches in order that the flow image could be accommodated by the field of view of the shadowgraph and Schlieren systems described in Progress Report No 20. The size of the field of view is itself dictated by the 14 inch diameter Fresnel lenses used.

In order to enable the visualization of larger fields, tests were conducted with the shadowgraph by removing the Fresnel lens and using the carbon arc lamp as a point light source. In this way, an area 20 inches by 20 inches or larger could be visualized. Figure 14-1 is a shadowgraph of the flow field of a 20 degree half angle wedge, 10 inches long at simulated Mach 2 flow. Because of the divergent light, the intensity is not uniform as seen from the very bright area in the center of the field.

A total pressure probe to be used for measuring water flow velocities was designed and constructed. Its main

dimensions are given in Fig 14-2 and initial tests to determine the water velocity profile with depth have been conducted using a simple inclined tube manometer. The total pressure probe and sensitive inclined manometer will enable accurate velocity determination and channel calibration.

9.3 Proposed Work

A technical report on the moving water facility, its instrumentation and the techniques developed and applied to aerodynamic decelerator problems is in preparation and will be submitted for approval.

Further developments and improvements designed to extend the effectiveness and applications of this facility have been submitted in the new contract proposal.

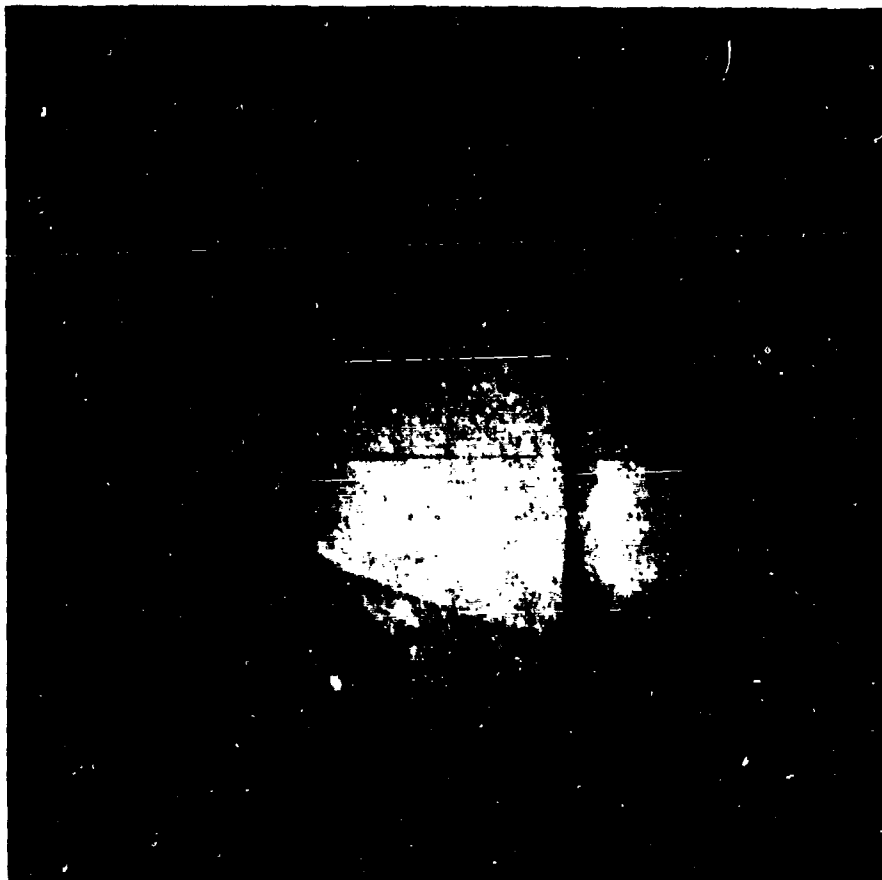


FIG 14-1. LARGE FIELD SHADOWGRAPH OF 20° HALF ANGLE WEDGE
10 INCHES LONG AT SIMULATED MACH 2

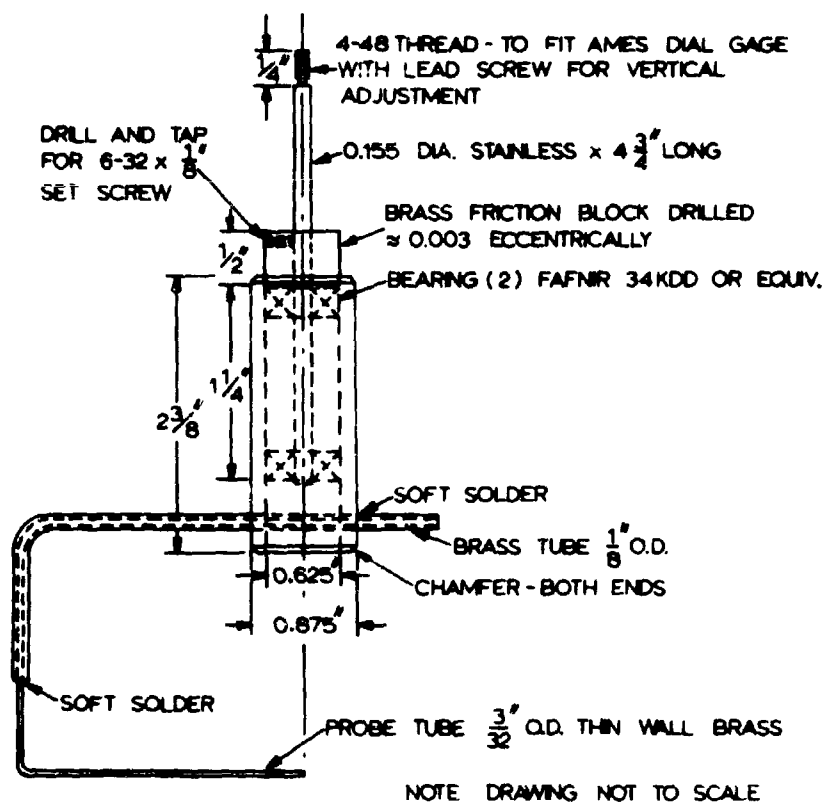


FIG 14-2. DESIGN DRAWING OF WATER FLOW
PRESSURE PROBE

Project No 16

9.6 Stress Analysis of the T-10 Troop Parachute

A preliminary technical report concerning this work has been written and will be submitted for review shortly.

Project No 17

11.0 Aerodynamic Characteristics of the Parachute Stabilized A-21 Cargo Container

11.1 Introduction

The main objective of this project is to establish the basic aerodynamic coefficients of an aerial delivery system consisting of the A-21 cargo container and the most suitable parachute configurations to stabilize it.

Whenever possible, the findings of the earlier study on the A-22 cargo container reported in ASD TR 61-326 (Ref 1) are to be applied to the present work but necessary wind tunnel testing covering two airspeed ranges and an additional investigation involving the use of larger but reefed canopies for stabilization are specified.

11.2 Previous Work

A scaled down canvas and webbing sling assembly and canvas cover representing the A-21 cargo container and a wooden box 4 inches by 8 inches by 15 inches representing a typical load were described in Progress Report No 22 and illustrated in Figure 17-1 of that report. Preliminary tests on the model container alone were conducted in the closed test section of the University of Minnesota subsonic wind tunnel using a three-component mechanical balance and mounting system illustrated in

Figure 17-2 of the last report.

The experimental results, however, showed certain inconsistencies attributed to the mechanical balance, particularly the moment measurements, and were deemed unreliable for reporting. In addition, the mounting arrangement made it impractical to cover the full range of angles of attack of 0 to ± 90 degrees. Therefore a strain gage balance for measuring the aerodynamic moments over the full angular range was designed for mounting and operation in either the closed or open test sections of the wind tunnel.

11.3 Present Work

The strain gage moment balance was made during the early part of the reporting period and was similar in design to a moment balance used for the A-22 container project. Its general arrangement and main details of mounting are illustrated in figures 7-1 and 7-2.

The lower portion of the 3/8 inch diameter rod forming the vertical pivotal shaft is hollowed out to form a torque tube with a wall thickness of 0.030 inches. Two Baldwin SR4 type strain gages, oriented along each of two orthogonal helical paths set at an angle of 45° to the shaft axis are cemented to the torque tube surface and are therefore subject to the diagonal tension and compression stresses resulting from the torque applied to the pivot shaft. The 4 gages are wired as a 4-arm bridge electrically connected to one channel of the

Century amplifying and recording system.

The balance and container mounting were designed to allow the recording of either the aerodynamic moment on the pivotal shaft or the free attitude angle of the container with respect to a fixed axis. To measure moment, the pivotal shaft is clamped at the lower end to a fitting attached to the turntable which forms the floor of the test section. The torque applied by the aerodynamic forces on the container model is sensed by the 4-arm bridge circuit. The upper end of the pivotal shaft fits into a self-aligning bearing mounted in the ceiling of the test section. The container angle of attack can be set by rotating the whole turntable.

The free attitude angle of the container is sensed by means of a high resolution, wire-wound circular potentiometer mounted inside a fitting at the base of the pivotal shaft; the wiper of this potentiometer is attached to the pivotal shaft and the shaft itself is allowed to rotate freely by releasing the clamp used for moment measurement. The potentiometer has 1020 turns over an arc of 340 degrees, i.e. it has an angular resolution of $1/3$ of 1 degree and it is connected in a two-arm bridge circuit.

Initial runs at the high speed range (about 100 ft/sec) indicated rather large deflection of the $3/8$ inch diameter rod forming the pivotal shaft and this tended to affect the moment readings. Therefore a system of guy wires and bearings was incorporated to reduce shaft deflections due to lift and drag

forces on the container and this eliminated this potential source of error. There is, however, some difficulty in obtaining perfect alignment between the clamp, the two guy wire bearings, and the ceiling bearing. Great care is exercised to effect the best possible alignment over the full angular range and in addition, a plot of initial deflection versus angle α is made and a correction applied to the data for each angle.

Calibration of the moment gage was made by fixing a moment arm to the container model and applying static moments using known weights attached to the moment arm and recording the corresponding galvanometer deflections for a specified gain setting of the amplifier. Figure 7-3 gives the calibration curve obtained with a gain setting of 1 (maximum) and used for the tests reported for $q = \frac{1}{2}$ inch of water. It shows satisfactory linearity and sensitivity.

It is convenient to specify a system of three orthogonal axes with the origin at the center of gravity position of the container. The first axis, the longitudinal axis, may be defined as the axis through the center of gravity perpendicular to the base of the container, i.e. in the height direction. The other two axes through the center of gravity, the lateral axes, are orthogonal to the longitudinal axis. One may consider an infinite number of such orthogonal lateral axes but, on the basis of the container geometry and method of attachment of the

risers and parachute, it is natural to consider a system of two lateral axes that are perpendicular to the side faces of the container. Figure 7-4 illustrates the reference system used and the sign convention for the angle of attack and moment coefficient. Two different orientations of the container model denoted by orientations A and B were tested to determine the more critical one from the stabilization viewpoint.

Wind tunnel tests were first carried out at an airspeed of 47.7 ft/sec with the pivotal axis perpendicular to the 4 inch by 15 inch face of the model container (orientation A). Moment recordings were taken in the angular range 0° to 20° at 2° intervals and 20° to 90° with 5° intervals and were repeated for the negative angular range 0° to -90° with the same intervals. The experimental data was consistent and repeatable. The corresponding values in the positive and negative angular ranges were averaged, corrected for slight unsymmetry of the flow and plotted as C_m versus α . The moment coefficient is based on the area of the base of the container, A, the length of the diagonal of that base, d, and the dynamic pressure of the flow, $q = \frac{1}{2} \rho v^2$, and is determined by

$$C_m = \frac{M}{q S d} \quad (1)$$

Figure 7-5 presents the average moment coefficient versus angle of attack for the A-21 container model in

orientation A at an airspeed of 47.7 ft/sec, or a Reynolds No of 0.445×10^6 . It shows a positive moment coefficient over the full angular range and a large stable derivative $\left(\frac{\partial C_M}{\partial \alpha}\right)$ at the neutral point of stability ($\alpha = 0$). Since the moment curve C_m versus α is expected to be substantially similar for the same configuration at high speeds, the same model was next tested in the other orientation, B. Figure 7-6 presents the average moment coefficient curve for this configuration at air speeds of 47.7 ft/sec and 116.8 ft/sec with corresponding Reynolds Numbers of 0.445×10^6 and 1.089×10^6 . There are some slight differences at the two airspeeds but the general characteristics of the moment curves are similar. They show relatively smaller but stable derivatives at 0° and $\pm 90^\circ$. There is also an unstable derivative at $\pm 65^\circ$.

The A-21 container is designed to accomodate a wide range of shapes and sizes varying in length from 30 to 60 inches, in width from 20 to 40 inches, and in height from 10 to 30 inches. From the stabilization standpoint, the determination of the most critical configuration involves considerations of shape, orientation, and size.

For a given container, the moment coefficient will depend on the shape, orientation, and angle of attack. As in the earlier study (Ref 1), the moment coefficients are referred to the container base area and a characteristic length equal to

the diagonal of the rectangular base. Thus, the size of the container is an important factor and it is necessary to determine the critical combination of shape, orientation, and size requiring the largest stabilizing effect from the parachute. Experimentally, this entails testing a large number of configurations and a practical compromise has to be chosen. For this purpose, the container load has been redesigned to provide means for varying the load shape, size, and orientation of its pivotal axis.

Preliminary tests with free pivotal axis and models of the ribless guide surface and ribbon parachute models with risers representing 10 and 20 feet full scale suggest that the two point suspension arrangement may not be very efficient for the A-21 container and other suspension arrangements may prove more desirable.

11.4 Proposed Work

Using the redesigned model, tests will be conducted to determine the critical combination of shape, orientation, and size of load-container combination without stabilization.

Tests will then be conducted on this critical configuration using model parachutes of the ribbon and ribless guide surface with risers representing full lengths of 10 and 20 feet and the moment coefficients over the full angular range 0° to $\pm 90^\circ$ will be calculated.

The free attitude angles and overall characteristics

of the system of container, risers and parachute will then be determined.

The tests indicated above will be conducted at the two specified airspeed ranges of 20-40 ft/sec and 100-200 ft/sec in the closed test section and at the lower speed range in the open test section. The latter tests will indicate the effects of the tunnel wall constraint and enable testing with the longer risers.

After completion of the above tests, an investigation of large reefed canopies having the same drag area (when reefed) as the values obtained from the previous tests will be carried out.

REFERENCES

1. Heinrich, Helmut G. and Ibrahim, Shukry K.:
Determination of the Minimum Sized Parachute
Required for Stabilization of the A-22 Cargo
Container, ASD TR 61-326, November 1961.

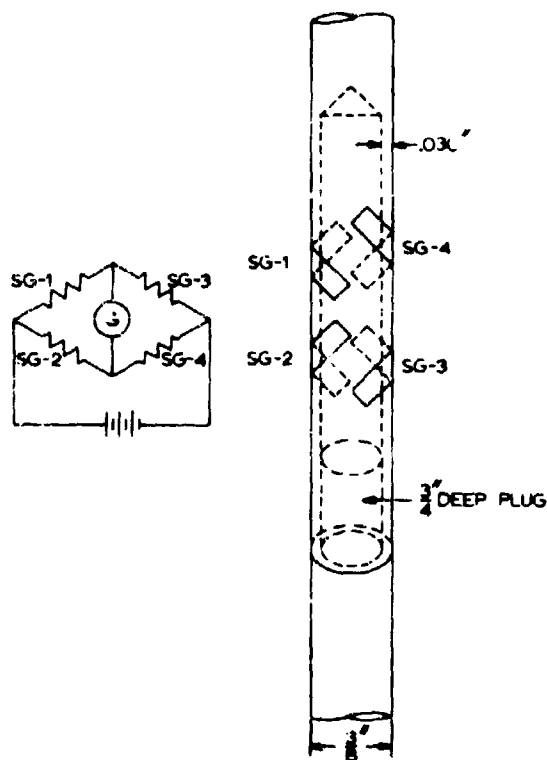


FIG 17-1. DETAIL OF STRAIN GAGE MOMENT BALANCE

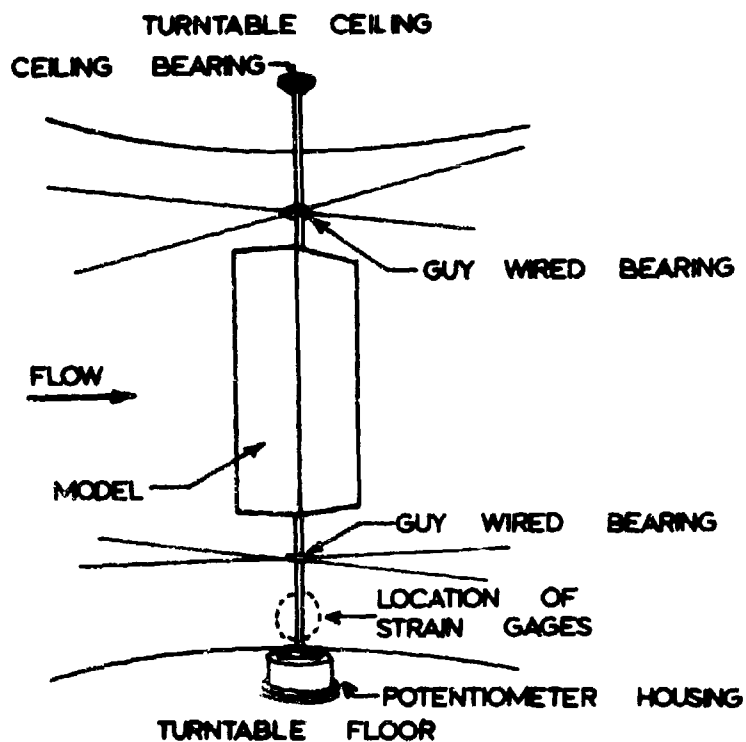


FIG 17-2. DIAGRAMMATIC VIEW AND PHOTOGRAPH OF A-21 MODEL MOUNTING IN CLOSED TEST SECTION- ORIENTATION B

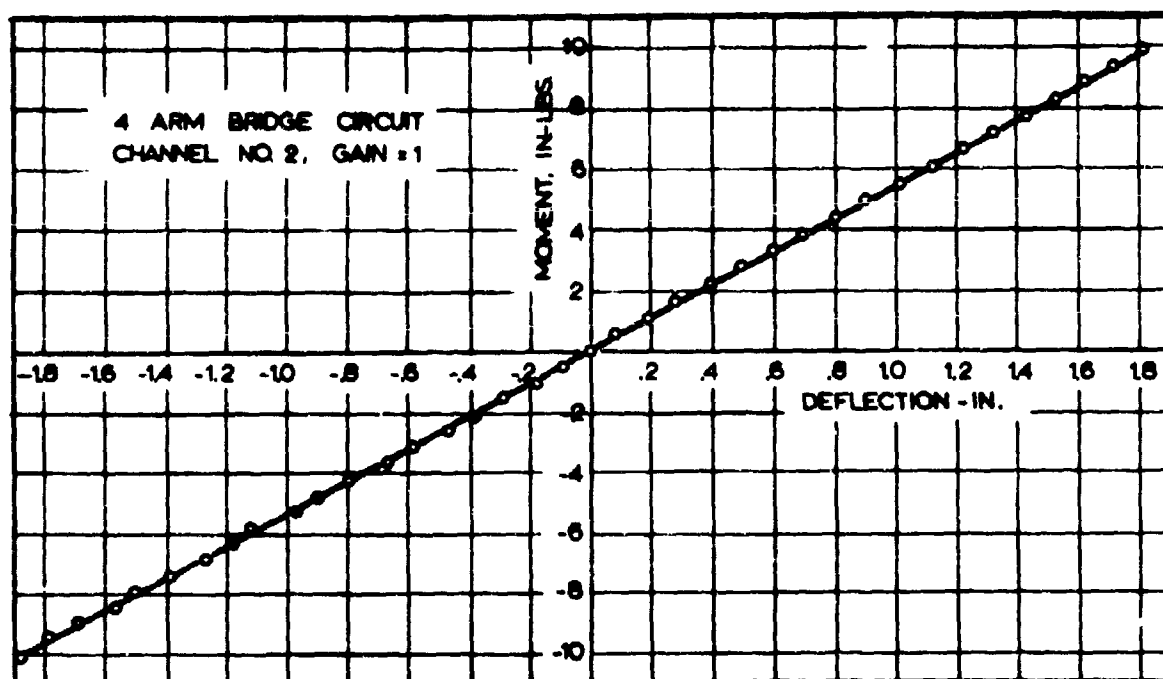


FIG 17-3. MOMENT BALANCE CALIBRATION

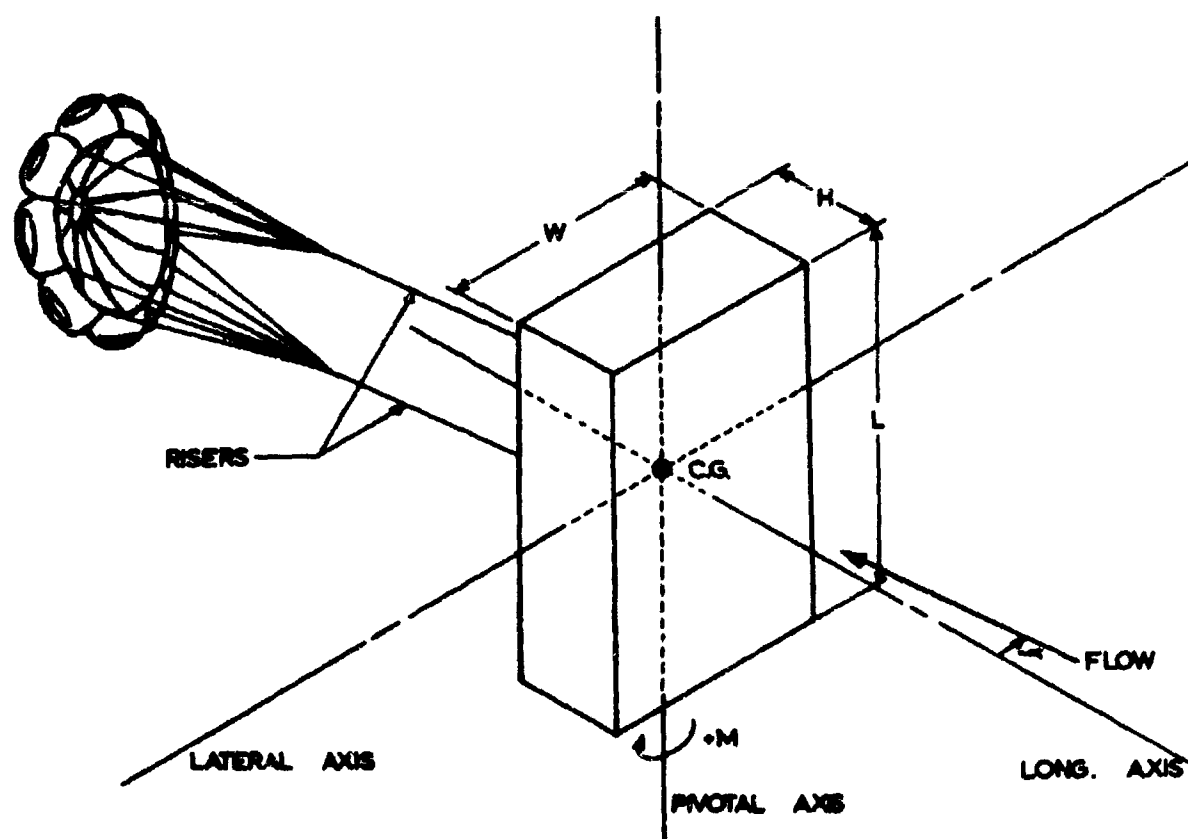


FIG 17-4. SYSTEM OF REFERENCE FOR ORIENTATION B

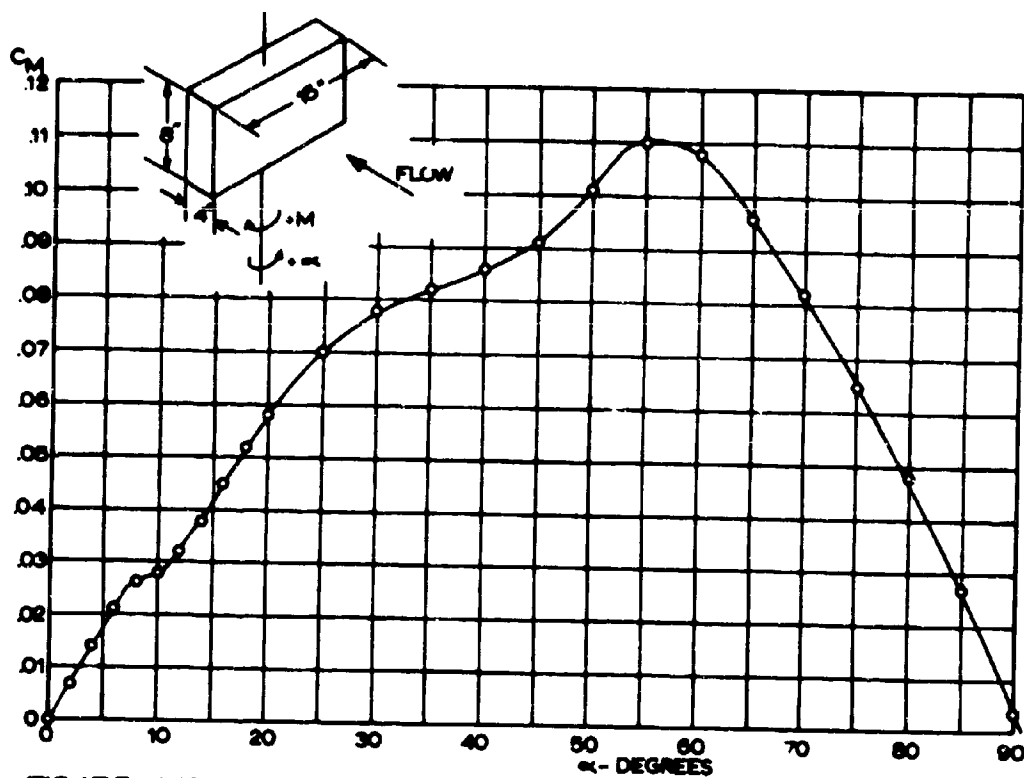


FIG 17-5. MOMENT COEFFICIENT OF A-21 CONTAINER MODEL IN ORIENTATION A
TEST REYNOLDS NO. = 445×10^6

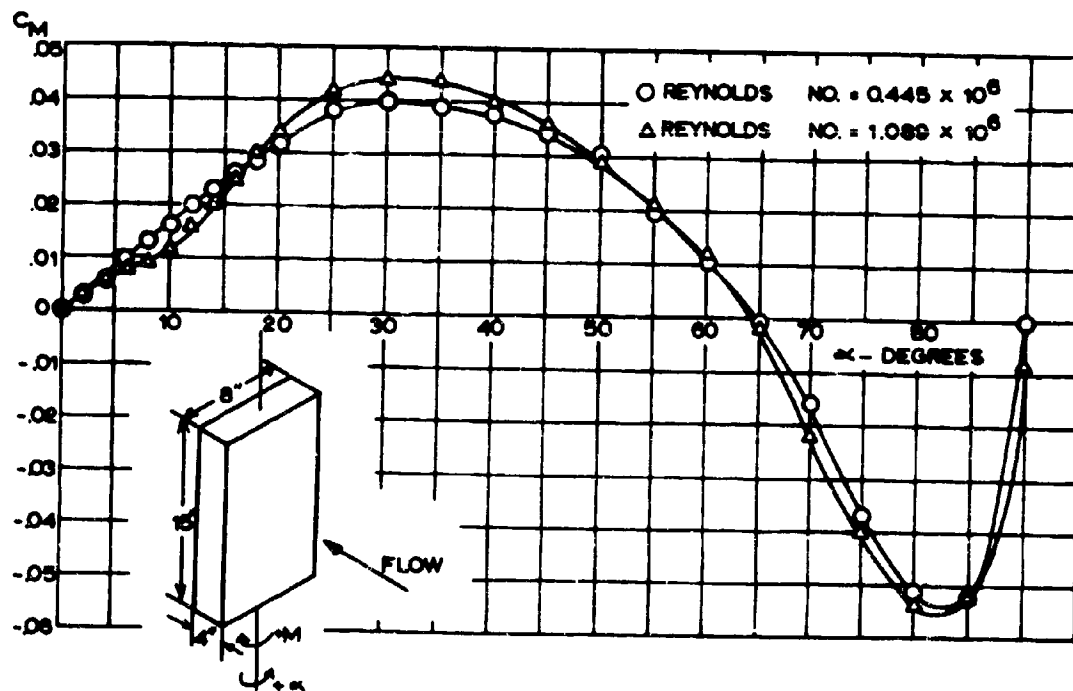


FIG 17-6. MOMENT COEFFICIENT OF A-21 CONTAINER MODEL IN ORIENTATION B

Project No 18

12.0 Aerodynamic Characteristics of the 'Cross' and
Wagon Wheel' Type Parachutes.

12.1 Evaluation of 'Cross' and 'Wagon Wheel' Type
Parachute Configurations in Free Stream

12.1.1 Introduction

The purpose of this investigation is to establish the aerodynamic and opening characteristics of the cross type and wagon wheel parachutes. Tests to determine such characteristics will be conducted in the wake of a primary body configuration, as well as in free stream with no forebody. The overall investigation involves three principal phases. The first of these, initiated in the previous reporting period, has been carried into the present reporting period and is designated, "Evaluation of 'Cross' and 'Wagon Wheel' Type Parachute Configurations in Free Stream."

12.1.2 Previous Work

Work prior to the present reporting period, as presented in Progress Report No 22, consisted of determining the aerodynamic characteristics in free stream of one model (textile) of the wagon wheel parachute configuration, and two models of the cross parachute configuration, one of these being fabricated from a non-porous material. The aerodynamic

characteristics investigated were: the normal force coefficient, C_N ; the tangent force coefficient, C_T ; and the aerodynamic moment coefficient, C_M . The results of these investigations were presented in Progress Report No 22, Figs 18-10 through 18-17. The normal, tangent, and moment coefficients are based on total cloth area and a moment arm equal to the suspension line length.

Since the last reporting period, it has been decided that to facilitate comparison of like canopies, (such as the wagon wheel and ribbon parachutes), a standard must be established for determining area and moment arm length.

A description of the reasoning employed in arriving at this standard together with revised test results will be presented in the next progress report.

12.1.3 Continuation

Drawings of three new configurations for the Wagon Wheel type parachute, and three new configurations for the Cross type parachute have been provided by the Procuring Agency. For the Wagon Wheel parachute configurations, the number of spokes is varied, while for the Cross parachute, the ratio between the widths and lengths of the arms, W/L , is varied. Three models, each of a different cloth type (varying nominal porosity) are being constructed for each of the three new Wagon Wheel configurations, making a total of nine Wagon Wheel models. In addition, three models, each of a different cloth

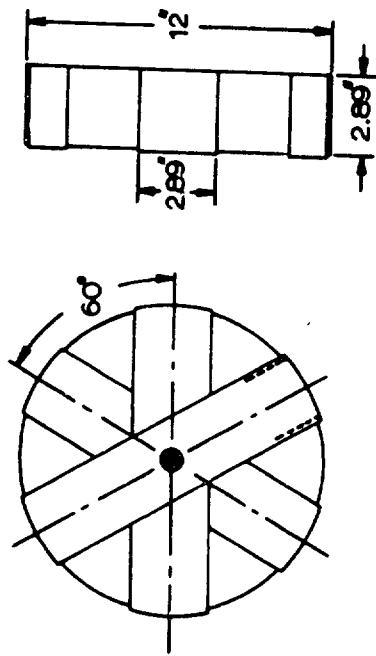
type, are being constructed for two of the new Cross parachute configurations, and two models, each of a different cloth type, will be constructed for the third Cross configuration, making a total of eight Cross parachute models being constructed. Figures 18-1 and 18-2 show sketches of each of the new parachute configurations. It may be noted that in the new Wagon Wheel Configurations, the gores linking the outer ends of the spokes of the first Wagon Wheel model have been replaced by a single band of cloth encompassing the spokes of the parachute. Also, the new configurations of the Wagon Wheel models will not have a hemi-spherical shape as the first model, but instead, will retain a more flat inflated shape.

12.4 Proposed Work

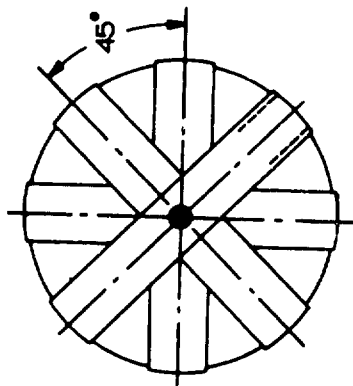
The aerodynamic characteristics of the models constructed from the new design configurations will be investigated in free stream, and when the most favorable configuration of each parachute has been determined, these configurations will be combined with an A-21 or A-22 Container and further investigation will be carried out to establish the aerodynamic characteristics of the parachute in the wake of the container forebody. Having completed these studies, an investigation will be carried out to determine the inflation characteristics of the most promising parachute configurations in free flight as well as in the wake of a cargo container in

the infinite mass case. These investigations will be conducted employing high speed films to measure opening time, and a strain gage bridge and electronic recording device to measure opening force.

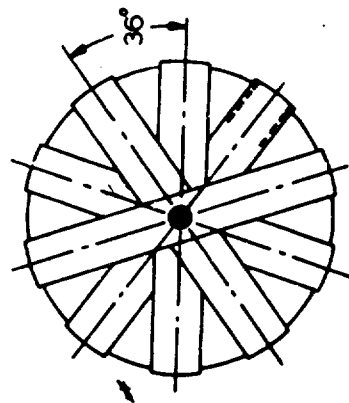
This work, however, may have to be postponed in view of the necessity to write technical reports about other aspects of the entire research effort.



3 SPOKES 12.0' x 2.89'
1 BAND 37.70' x 2.89'
12 SUSPENSION LINES
SCALE $\frac{3''}{16} = 1'$

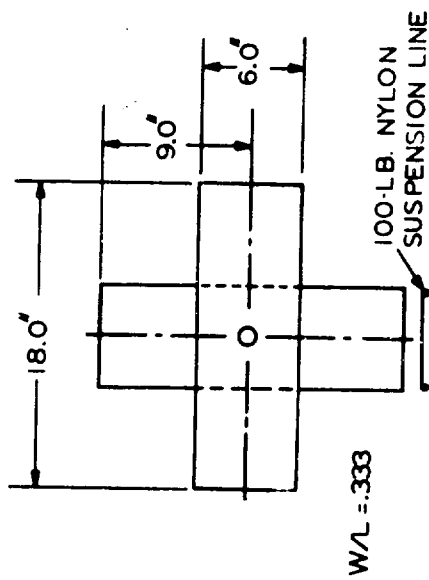


4 SPOKES 12.0' x 2.22'
1 BAND 37.70' x 2.22'
16 SUSPENSION LINES
SCALE $\frac{3''}{16} = 1'$



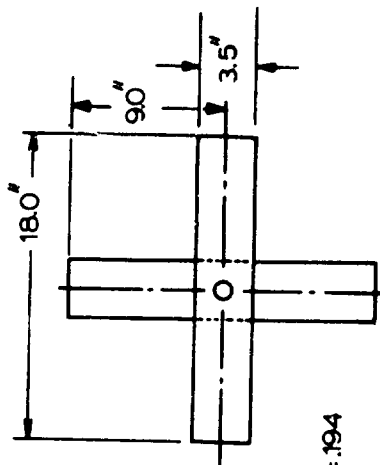
5 SPOKES 12.0' x 1.89'
1 BAND 37.70' x 1.89'
20 SUSPENSION LINES
SCALE $\frac{3''}{16} = 1'$

FIG 1B-1. "WAGONWHEEL" PARACHUTE MODEL CONFIGURATIONS

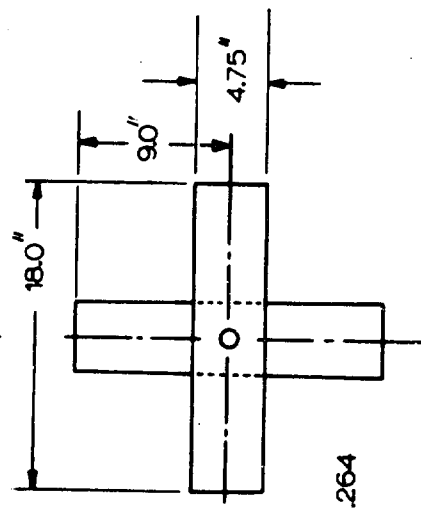


W/L = .333

100-LB. NYLON
SUSPENSION LINE



W/L = .194



W/L = .264

FIG 1B-2. "CROSS" TYPE PARACHUTE MODEL CONFIGURATIONS

Project No 19

13.0 Determination of Mass Flow Through Parachutes With Inherent Geometric Porosity

13.1 Introduction

The present reporting period marks the initiation of the test program of Project Number 19, "Determination of Mass Flow Through Parachutes With Inherent Geometric Porosity." As noted in detail in Aeronautical Systems Division Contract No. AF 33(616)-8310, Project 19, the purpose of this investigation is, in part, to determine experimentally the mass flow ratios through the canopies of fully inflated ribbon parachute models at subsonic, transonic, and supersonic speeds. While the total effort calls for use of models both with and without forebodies, the present test program calls for free stream tests on models having geometric porosities of 15 to 30 percent.

Since the mass flow of air through the canopy is solely a function of the pressures to which the parachute is subjected and the geometric porosity and shape of the openings in the chute, it appears, as noted in the contract, that the initial step is to determine the pressure distributions on the canopies by means of internal and external pressure taps. Then

rigid ribbon model would be fitted with a rear hollow support sting and the skirt of the canopy covered with a solid plate and the model mounted in the wind tunnel.

After the flow is established around the configuration, an airflow is introduced through the support sting and adjusted to a pressure equal to the internal pressure previously measured under the same free stream condition. The mass flow through this system is then measured. When steady-state conditions are reached, the in-flowing air mass must be approximately the same as the flow through the porous canopy under normal conditions.

12.2 Subsonic Model Tests

Rigid models of the circular flat ribbon parachute with geometric porosities of 15, 20, 25, and 30 per cent are currently being tested at subsonic Mach numbers in the variable density wind tunnel at the University of Minnesota. (Fig 19-1 shows a typical model configuration). There are two models for each porosity value; one with pressure taps on the internal surface and one with pressure taps on the outer surface (see Fig 19-1). A typical model mounted in the wind tunnel test section is shown in Fig 19-2.

The subsonic pressure distributions obtained from these tests will be used to obtain mass flow measurements by the means originally proposed in the contract and as noted above. These mass flow measurements for subsonic Mach numbers

will also be conducted in the subsonic variable density wind tunnel at the University of Minnesota.

13.3 Supersonic Model Tests

With the Supersonic test program, it has been necessary to alter the mass flow determination methods from the method originally outlined in the contract. Preliminary calculation of the mass flow through a hollow sting showed that unreasonably large pressures and sting sizes would be necessary to accommodate the necessary mass flow. Therefore while the procedure for obtaining pressure distributions on the surface of the model will be the same, it will be necessary to change the method for determining the mass flow. It has thus been proposed, that the canopy models be mounted in the flow measuring facility originally used to measure the effective porosity of ribbon grids.

The supersonic Mach number effects will be simulated by producing the same pressure distribution and pressure ratio across the model as was present in the pressure distribution studies in the supersonic wind tunnel. In this manner all mass crossing the boundary of the enclosed model must pass through the model itself and the mass flow can thus be measured.

13.4 Proposed Work

It is anticipated that tests on the four models of the circular flat ribbon parachutes with geometric porosities of

15, 20, 25, and 30 per cent at one subsonic and one supersonic Mach number will be finished and all data reduction completed shortly. A subsequent technical report will be written concerning this phase of the program by the end of this contract period.

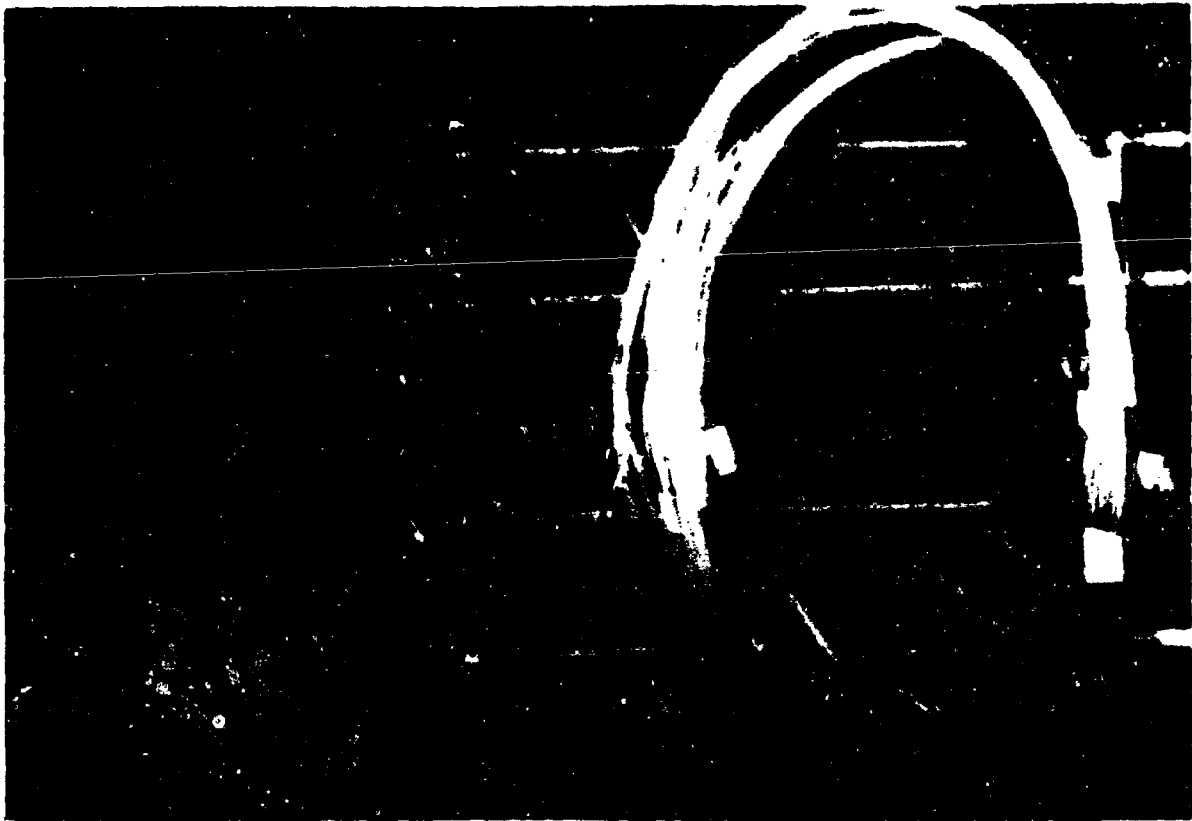


FIG 19-1. RIGID PRESSURE TAP MODELS USED IN MASS FLOW STUDIES OF CIRCULAR FLAT RIBBON PARACHUTES.



FIG 19-2. RIGID PARACHUTE MODEL MOUNTED IN SUBSONIC VARIABLE DENSITY WIND TUNNEL.

APPENDIX

The authors of this report who are listed on the front page wish to acknowledge the accomplishments and assistance of the following personnel:

Clerical Staff:

E. Zembergs, Sr. Engineering Assistant
Beverly M. Broers, Secretary

Graduate Students:

R. O. Bailey, Research Assistant
S. R. Hess, Research Assistant
L. R. Jamison, Research Assistant
W. K. Lockman, Research Assistant
D. J. Monson, Research Assistant
J. J. Paulsen, Research Assistant
R. E. Schaller, Research Assistant
R. E. Rose, Research Fellow
L. W. Rust, Research Fellow

Undergraduate Students:

J. M. Carlson, Engineering Assistant
D. F. Coleman, Engineering Assistant
N. A. Dodge, Engineering Assistant
D. D. Evenson, Engineering Assistant
D. K. Florman, Engineering Assistant
R. W. Friestad, Engineering Assistant
K. J. Goar, Engineering Assistant
R. W. Gutenkauf, Engineering Assistant
R. J. Hubert, Engineering Assistant
J. M. Johnson, Engineering Assistant
H. M. Lipka, Engineering Assistant
M. J. Martin, Engineering Assistant
W. A. McArthur, Engineering Assistant
T. C. Nietz, Engineering Assistant
R. A. Noreen, Engineering Assistant
D. L. Pekarek, Engineering Assistant
R. O. Strom, Engineering Assistant
L. M. Timmons, Engineering Assistant

Machine Shop Personnel:

J. Taube, Laboratory Machinist
P. A. Huehnert, Wind Tunnel Mechanic